



저작자표시-비영리-변경금지 2.0 대한민국

이용자는 아래의 조건을 따르는 경우에 한하여 자유롭게

- 이 저작물을 복제, 배포, 전송, 전시, 공연 및 방송할 수 있습니다.

다음과 같은 조건을 따라야 합니다:



저작자표시. 귀하는 원저작자를 표시하여야 합니다.



비영리. 귀하는 이 저작물을 영리 목적으로 이용할 수 없습니다.



변경금지. 귀하는 이 저작물을 개작, 변형 또는 가공할 수 없습니다.

- 귀하는, 이 저작물의 재이용이나 배포의 경우, 이 저작물에 적용된 이용허락조건을 명확하게 나타내어야 합니다.
- 저작권자로부터 별도의 허가를 받으면 이러한 조건들은 적용되지 않습니다.

저작권법에 따른 이용자의 권리는 위의 내용에 의하여 영향을 받지 않습니다.

이것은 [이용허락규약\(Legal Code\)](#)을 이해하기 쉽게 요약한 것입니다.

[Disclaimer](#)

이학박사 학위논문

**Dynamics of the opposing Hadley cell-
jet change in the Southern
Hemisphere
in the Last Glacial Maximum**

마지막최대빙하기에서 남반구 해들리순환-제트의
반대 방향 이동의 역학

2023 년 2 월

서울대학교 대학원
지구환경과학부
김서연

Dynamics of the opposing Hadley cell- jet change in the Southern Hemisphere in the Last Glacial Maximum

마지막최대빙하기에서 남반구 해들리순환-제트의
반대 방향 이동의 역학

지도교수 손 석 우

이 논문을 이학박사 학위논문으로 제출함

2022 년 10 월

서울대학교 대학원
지구환경과학부
김서연

김서연의 이학박사 학위논문을 인준함

2023 년 1 월

위 원 장 허 창 회 (인)

부위원장 손 석 우 (인)

위 원 유 창 현 (인)

위 원 김 성 중 (인)

위 원 김 주 완 (인)

Abstract

A poleward displacement of the Hadley cell (HC) edge and the eddy-driven jet latitude has been observed in the Southern Hemisphere (SH) during the last few decades. This change is further projected to continue in the future, indicating coherent tropical and extratropical zonal-mean circulation changes from the present climate to a warm climate. Here we show that such a systematic change in the zonal-mean circulation change does not hold in a cold climate. By examining the Last Glacial Maximum (LGM), preindustrial (PI), and extended concentration pathway 4.5 (ECP4.5) scenarios archived for phase 3 of the Paleoclimate Modeling Intercomparison Project (PMIP3) and phase 5 of the Coupled Model Intercomparison Project (CMIP5), it is shown that while the annual-mean SH HC edge systematically shifts poleward from the LGM scenario to the PI scenario and then to the ECP4.5 scenario the annual-mean SH eddy-driven jet latitude does not. All models show a poleward jet shift from the PI scenario to the ECP4.5 scenario, but over one-half of the models exhibit no trend or even an equatorward jet shift from the LGM scenario to the PI scenario. This opposing HC and jet change is most pronounced in SH winter when the Antarctic surface cooling in the LGM scenario is comparable to or larger than the tropical upper-tropospheric cooling. This result indicates that polar amplification could play a crucial

role in driving the decoupling of the tropical and midlatitude zonal-mean circulation in the SH in a cold climate.

The opposing HC–jet change, an equatorward shift of the HC edge but a poleward shift of the jet latitude, is well reproduced in a dynamical core general circulation model (GCM) experiment in which the LGM-like thermal perturbations are imposed. By systematically varying the amplitude of tropical upper-tropospheric and polar surface cooling, an opposing shift of circulation is found when polar cooling is much stronger than tropical cooling. This is due to the higher sensitivity of the jet-latitude change in response to polar cooling than its HC counterpart. The HC-edge change is largely attributed to the activity of slow waves and the axisymmetric circulation change. They lead to the HC edge being weakly influenced by extratropical baroclinicity, resulting in an equatorward shift of the HC edge. Instead, the jet latitude is much influenced by the enhancement of lower-level baroclinicity on its poleward flank due to polar cooling. This makes long waves become more unstable and an increase in anticyclonic wave-breaking events, which give rise to a poleward shift of the jet.

The above dynamical interpretation is revisited by using the atmosphere-coupled global climate models (AGCM) with varying sea ice concentrations (SIC). It turned out that the LGM winter condition with

high SIC experiment well reproduces the opposing change of the HC and jet, highlighting the pivotal role of SIC in shifting the jet in the SH. Furthermore, an increase in the lower-level baroclinicity in the high latitudes and the related importance of long waves are well found in high SIC experiments. This demonstrates that the dynamical mechanisms proposed above work well in the more complex coupled climate models.

We also found such circulation changes but with an opposite sign in global warming-like dynamical-core experiments, suggesting a potential opposing HC–jet shifts in the future.

Keyword : Hadley cell, eddy–driven jet, Last Glacial Maximum, Rossby dynamics, idealized model study

Student Number : 2017–37910

Table of Contents

<i>Abstract.....</i>	<i>iii</i>
<i>List of tables.....</i>	<i>ix</i>
<i>List of Figures</i>	<i>x</i>
<i>Chapter 1. Introduction</i>	<i>1</i>
1.1 Dynamics of Large-scale Circulation.....	1
1.2 Relationship between the HC edge and jet latitude	4
1.3 Circulation changes from paleo to warm climates	7
1.3.1 Recent circulation changes.....	8
1.3.2. Circulation changes in the paleoclimate.....	13
1.4 Aims of the Thesis and Outline	15
<i>Chapter 2. Data and Methods.....</i>	<i>18</i>
2.1 Coupled models: CMIP5, PMIP3, PMIP4	18
2.2 Configuration for simplified dry dynamic core	20
2.2.1 Model description.....	20
2.2.2 Cooling experimental setup: Equilibrium simulation	22
2.2.3. Cooling experimental setup: Transient simulation.....	24
2.2.4. Axisymmetric (2D) experiment.....	26
2.3 AGCM description and experimental design	26
2.3.1 Model description.....	26
2.3.2 Experimental design	28
2.4 Analysis methods.....	29
2.4.1 Eddy spectra analysis	29
2.4.2 Refractive index and reflective level	30
<i>Chapter 3. Opposing HC–jet change in the Last Glacial Maximum</i>	<i>32</i>

3.1. Zonal-mean responses.....	33
3.2 HC–jet Relationship from cold to warm climates	39
3.2.1 Long-term change <i>versus</i> interannual variability	39
3.2.2 Model-mean bias in LGM.....	43
3.2.3. Update to state-of-the-art models.....	47
3.3 Role of tropical and polar temperature in the opposing HC–jet change.....	48
3.4 Global cooling-like experiments: dynamic-core GCM.....	52
3.4.1 Motivation	52
3.4.2 Control experiment.....	54
3.4.3 Reference Cooling experiment.....	55
3.4.4 Parameter sweep study.....	62
<i>Chapter 4. Dynamical mechanisms for opposing HC –jet change</i>	<i>67</i>
4.1 Plausible mechanism(s).....	67
4.2 Eddy activities in the global cooling experiments.....	70
4.3 Axisymmetric circulation response to thermal forcing.....	83
4.4 Transient response of circulation	90
4.4.1 Motivation	90
4.4.2 Time evolution of circulation change.....	92
4.4.3 Changes in mean meridional circulation (MMC)	99
4.4.4 Change in zonal winds.....	101
4.4.5 Mechanisms of the tropospheric jet shift	106
<i>Chapter 5. The opposing HC–jet change in the LGM scenario: using a full GCM</i>	<i>111</i>
5.1 Motivation.....	111
5. 2 Zonal-mean atmospheric change.....	113
5.3 The eddy activity change	119

<i>Chapter 6. Conclusions</i>	<i>124</i>
<i>Chapter 7. Further work: global warming-like simulations.....</i>	<i>133</i>
<i>References</i>	<i>143</i>
국문 초록	152

List of tables

Table 2.1. CMIP5 and PMIP3 models used in this study. The six models, which provide all three experiments, are indicated by asterisks. The analyzed simulation is denoted with “O”.

Table 2.3. PMIP4 models used in this study.

Table 2.4. Summary of model experiments.

Table 2.5. CESM model description used in Chapter 5.

Table 3.1. The shifting rates of the HC edge and jet latitudes to tropical/polar thermal forcings and the HC edge-to-jet latitude shifting ratio (“HC-jet ratio”) for each forcing. The plus sign indicates a poleward shift.

List of Figures

Figure 2.1. The equilibrium temperature profile (black contours) and the additional tropical, q_{trop} , and polar thermal forcings, q_{pole} , for cooling experiments. The additional forcings are introduced to mimic LGM-like climate states, respectively. The contour intervals are 20 K, and shading intervals are 0.2 K day^{-1} .

Figure 3.1. Multi-model-averaged annual-mean zonal-mean temperature (left), mass stream function (middle), and zonal wind (right) in PI simulation (contours), ECP4.5-PI (top) and LGM-PI (bottom) differences are shaded. Units are K for temperature, $10^{10} \text{ kg s}^{-1}$ for mass stream function, and m s^{-1} for zonal wind. The dotted region indicates that more than 80% of the models show the same sign. Note that the latitudinal range of (b, e) is different from the others.

Figure 3.2. The annual-mean HC edge and jet latitude changes in (a) ECP4.5 and (b) LGM simulations compared to PI simulation. The statistically significant difference at the 95% confidence level is indicated with a filled bar. Note that a positive value represents a poleward HC shift or a poleward jet shift in the SH.

Figure 3.3. Relationship between the HC edge and jet latitude changes in the LGM-PI (blue) and ECP4.5-PI (red) differences for (a) the annual mean, (b) austral winter, and (c) austral summer. The models that show statistically significant jet latitude changes are denoted with filled circles, while those with an insignificant change are denoted with an open circle. (d) Correlation coefficients between the HC edge and jet latitude changes in the LGM-PI (blue) and the ECP4.5-PI (red) differences for all seasons with significant correlation coefficients denoted with asterisks. (e) Interannual correlation between the HC edge and jet latitude in the PI simulations. The correlation coefficient derived from each model is simply averaged. The asterisk indicates that more than 80% of the models have a statistically significant correlation at the 95% confidence level.

Figure 3.4. Comparison between the interannual ratio and long-term ratio of HC edge to jet latitude in LGM (blue) and ECP4.5 (red) simulations for (a) the annual mean, (b) austral winter, and (c) austral summer. The long-term ratio is considered as the difference of the LGM (blue) or ECP4.5 (red) simulation from the PI simulation. The interannual ratio with a statistically significant correlation coefficient at

the 95% confidence level between the HC edge and the jet latitude is denoted with filled circles.

Figure 3.5. The austral winter (JJA) zonal-mean zonal wind at 300 hPa (solid lines) and 850 hPa (dashed lines) in the LGM (blue) and PI (black) simulations. The reference wind profile from JRA-55 is also shown in gray with one standard deviation on the interannual timescale. The position of the eddy-driven jet and its one standard deviation are indicated in the top-left corner of each panel.

Figure 3.6. Same as Figure 3.5 but for the ECP4.5 (red) and PI (black) simulations.

Figure 3.7. The relationship of jet latitude change to (a) $\Delta T_{\text{trop},250}$ and (b) $\Delta T_{\text{pole},925}$ in the LGM-PI (blue) and ECP4.5-PI (red) differences in austral winter (JJA). The stars denote the models with a flatten eddy-driven jet in the LGM simulations. The filled circles indicate the models which have statistically significant jet latitude changes as in Fig. 3.3.

Figure 3.8. Same as Fig. 3.3 (a-c) but for PMIP4 models.

Figure 3.9. Polar temperature changes at 925 hPa ($\Delta T_{\text{pole},925}$) and tropical temperature changes at 250 hPa ($\Delta T_{\text{trop},250}$) in austral winter (left) and summer (right) for the ECP4.5-PI differences (top) and the LGM-PI differences (bottom). The model that shows a statistically significant jet latitude change is denoted with a filled circle, while that with an insignificant change is denoted with an open circle as in Fig. 3.3 and Fig. 3.7. The asterisk indicates the model showing a poleward jet shift.

Figure 3.10. (top) Climatological zonal-mean temperature (unit: K), (middle) mass stream function (unit: $10^{10} \text{ kg s}^{-1}$), and (bottom) zonal wind (unit: m s^{-1}) in CTRL (contours) and their responses to the thermal forcings (shading) when $(q_{\text{trop}}, q_{\text{pole}}) = (-0.3, 0.0)$, $(0.0, -1.2)$, and $(-0.3, -1.2) \text{ K day}^{-1}$ from left to right columns. The contours in (a-c) are from 200 K to 310 K with an interval of 10 K in (a-c), from $-20 \times 10^{10} \text{ kg s}^{-1}$ to $20 \times 10^{10} \text{ kg s}^{-1}$ with an interval of $2 \times 10^{10} \text{ kg s}^{-1}$ in (d-f), and from 0 to 40 m s^{-1} with an interval of 5 m s^{-1} in (g-i). In the bottom row, zero lines of shading are indicated in thick gray lines. The experiment denoted with TROP-C is further examined in Chapter 4.

Figure 3.11. Same as Fig. 3.10 but for experiments with $(q_{\text{trop}}, q_{\text{pole}}) =$ (left) $(0.0, -2.8)$ and (right) $(-0.3, -2.8) \text{ K day}^{-1}$. The experiments denoted with POLE-C and COMB-C are further examined in Chapter 4. Figure formats are identical to those in Fig. 3. 10.

Figure 3.12. (left) Temperature, mean meridional circulation, zonal wind in the linear summation of experiments with $(q_{\text{trop}}, q_{\text{pole}}) = (-0.3, 0.0)$ K day⁻¹ and $(q_{\text{trop}}, q_{\text{pole}}) = (0.0, -1.2)$ K day⁻¹, which are represented in the left two columns of Fig. 3.10. (right column) Same as (a, c, e) but for the linear summation of experiments with $(q_{\text{trop}}, q_{\text{pole}}) = (-0.3, 0.0)$ K day⁻¹ and $(q_{\text{trop}}, q_{\text{pole}}) = (0.0, -2.8)$ K day⁻¹ with the former same as the left column of Fig. 3.10 and the latter shown in the right column of Fig. 3.11. Figure formats are identical to those in Fig. 3. 10.

Figure 3.13. (a) The HC-edge and jet-latitude changes with respect to CTRL as a function of tropical forcing (q_{trop} in x-axis) and polar forcing (q_{pole} in the y-axis) in all cooling experiments. The upper and lower numbers in each box indicate the HC-edge and jet-latitude shifts from CTRL. The experiments with opposing circulation changes, i.e., an equatorward HC-edge shift but a poleward jet-latitude shift, are denoted in dark blue. The experiments, which are examined in detail in Chapter 4, are denoted with TROP-C, POLE-C, and COMB-C. (b) The relationship between the HC-edge and jet-latitude changes in experiments shown in (a). The experiment showing a significant jet-latitude shift at the 99% confidence level is denoted with a black edge, while the one with an insignificant shift is denoted with no edge.

Figure 4.1. (a) The 850-hPa zonal wind (U850), (b) 250-hPa eddy momentum flux (EMF250) divergence, (c) 500-hPa mass stream function (Ψ 500), and (d) 850-hPa eddy heat flux (EHF850) in CTRL (gray), TROP-C (orange), POLE-C (green), and COMB-C (blue). The maximum latitudes of U850, EMF250 convergence, and EHF850 are denoted with “X” in (a), (b), and (d), respectively. The zero-crossing latitudes for EMF250 divergence and Ψ 500 are denoted with “O” in (b) and (c), respectively.

Figure 4. 2. Eddy heat flux at 850 hPa along with the zonal wavenumber (x-axis) in CTRL (black), TROP-C (orange dotted), POLE-C (green dashed), COMB-C (blue solid) (unit: m s⁻¹ K).

Figure 4.3. EMF250 divergence cospectra (10^{-8} m s⁻², contours) as a function of angular phase speed and latitude in (a) CTRL, (b) TROP-C, (c) POLE-C, and (d) COMB-C. (b–d) The differences in EMF divergence in each experiment from CTRL (e.g., TROP-C *minus* CTRL) are shaded, with anomalous divergence in blue and convergence in red. Contours are depicted from -6×10^{-8} m s⁻¹ day⁻¹ to 6×10^{-8} m s⁻¹ day⁻¹ with intervals of 1×10^{-8} m s⁻¹ day⁻¹, and the shading range is from -5×10^{-8} m s⁻¹ day⁻¹ to 5×10^{-8} m s⁻¹ day⁻¹ with intervals of 0.4×10^{-8} m s⁻¹ day⁻¹. Thick and

thin curves indicate the critical latitude and the reflective latitude for zonal wavenumber 6, respectively, for CTRL (gray) and cooling experiments (colored). Gray shaded phase speed range of -5 to 5 m s^{-1} denotes a *slow* phase speed range.

Figure 4.4. Eddy Momentum flux at 250 hPa (EMF250) divergence cospectra (10^{-8} m s^{-2} , contours) as a function of angular phase speed and latitude in the linear summation of TROP-C and POLE-C in Figs. 4.2b and c, respectively. The differences in EMF divergence in the summation from CTRL are shaded, with anomalous divergence in blue and convergence in red. Contours are depicted from $-6 \times 10^{-8} \text{ m s}^{-1} \text{ day}^{-1}$ to $6 \times 10^{-8} \text{ m s}^{-1} \text{ day}^{-1}$ with intervals of $1 \times 10^{-8} \text{ m s}^{-1} \text{ day}^{-1}$, and the shading range is from $-5 \times 10^{-8} \text{ m s}^{-1} \text{ day}^{-1}$ to $5 \times 10^{-8} \text{ m s}^{-1} \text{ day}^{-1}$ with intervals of $0.4 \times 10^{-8} \text{ m s}^{-1} \text{ day}^{-1}$. Thick and thin curves indicate the critical latitude and the reflective latitude for zonal wavenumber 6, respectively, for CTRL (gray) and cooling experiments (colored). Gray shaded phase speed range of -5 to 5 m s^{-1} denotes a slow phase speed range described in the text.

Figure 4.5. Zonal wavenumber-angular phase speed cospectra for the eddy momentum flux convergence at 250 hPa (a, b, c) at the tropics ($18-28^\circ$) and (d, e, f) at the midlatitudes ($40-45^\circ$) for (shading) CTRL (Unit: $10^7 \text{ m s}^{-1} \text{ day}^{-1}$). The changes of the EMF divergence for (a, d) TROP-C, (b, e) POLE-C, and (c, f) COMB-C compared to CTRL are in contours. The contour and shading intervals are $0.5 \times 10^7 \text{ m s}^{-1} \text{ day}^{-1}$.

Figure 4.6. (top) Temperature (unit: K), (middle) mass streamfunction (unit: $10^{10} \text{ kg s}^{-1}$), and (bottom) zonal wind (unit: m s^{-1}) in 2D-CTRL (contours) and their responses to the thermal forcings (shading; $2\text{D-EXP} \text{ minus } 2\text{D-CTRL}$) in axisymmetric simulations with $(q_{\text{trop}}, q_{\text{pole}}) = (-0.3, 0.0)$, $(0.0, -2.8)$, and $(-0.3, -2.8) \text{ K day}^{-1}$ from left to right columns. See section 2.2.4 for the details of the model experiments. Contours for top, middle, and bottom panels are from 210 to 350 K, -1.2×10^{11} to $1.2 \times 10^{11} \text{ kg s}^{-1}$, and 5 to 60 m s^{-1} with their intervals 10 K, $10^{10} \text{ kg s}^{-1}$, and 5 m s^{-1} , respectively, excluding zero lines.

Figure 4.7. (a) Temperature (unit: K), (b) mass streamfunction (unit: $10^{10} \text{ kg s}^{-1}$), and (c) zonal wind (unit: m s^{-1}) in 2D-CTRL (contours) and their responses in the linear summation of 2D_TROP-C and 2D_POLE-C (shading; linear summation *minus* 2D-CTRL) in axisymmetric simulations. Contours for top, middle, and bottom panels are from 210 to 350 K, -1.2×10^{11} to $1.2 \times 10^{11} \text{ kg s}^{-1}$, and 5 to 60 m s^{-1} with their intervals 10 K, $10^{10} \text{ kg s}^{-1}$, and 5 m s^{-1} , respectively, excluding zero lines.

Figure 4.8. (contours) The mass streamfunction (upper) and the zonal wind (lower) for (a, d) TROP-C, (b, e) POLE-C, and (c, f) COMB-C. The results are from the three-dimensional (3D) equilibrium experiments shown in Figs. 3.10 and 3.11. The gray shading denotes the area where the local Rossby number is greater than 0.5. Contours are from -20 to $20 \times 10^{10} \text{ kg s}^{-1}$ with intervals of $2 \times 10^{10} \text{ kg s}^{-1}$ for mass stream function, and 0 to 40 m s^{-1} with the interval of 5 m s^{-1} for zonal wind.

Figure 4.9. The HC edges in response to tropical cooling (q_{trop}) in the axisymmetric cooling simulations. Color on markers denotes the amplitude of polar cooling (q_{pole}) from 0 to -3.2 K day^{-1} . The linear regression line is denoted in black line.

Figure 4.10. Evolution of zonal-mean temperature (unit: K), zonal wind (unit: m s^{-1}), mean meridional circulation (MMC; unit: $10^{10} \text{ kg s}^{-1}$), and eddy momentum flux (EMF; unit: $\text{m}^2 \text{ s}^{-2}$) fields for the coherent case. (top) Control run values; (middle) difference between 10-day averages of the transient and the control run for days 5 to 15, for days 25 to 35, and (bottom) difference between the last 100-day average quasi-equilibrium states and the control run. (bottom) The control run in the top row is presented again in gray lines for the comparison.

Figure 4.11. Evolution of zonal-mean temperature (unit: K), zonal wind (unit: m s^{-1}), mean meridional circulation (MMC; unit: $10^{10} \text{ kg s}^{-1}$), and eddy momentum flux (EMF; unit: $\text{m}^2 \text{ s}^{-2}$) fields for the EXP-O. The overall format of the figure is identical to the Fig. 4.10.

Figure 4.12. Time evolutions of (left) ensemble-mean HC edge and (right) jet latitude changes in EXP-C (green) and in EXP-O (blue) from CTRL. Their one-standard deviation range across ensembles are denoted by shading. A negative value denotes a poleward shift (southward shift).

Figure 4.13. Zonal and ensemble-mean transient responses of 500-hPa meridional streamfunction ($10^{10} \text{ kg s}^{-1}$) as a function of latitude and time: (a, b): simulated and (c, d) diagnosed from the momentum budget [Eq. (4.2)].

Figure 4.14. Ten-day running means of the change in each of the terms in Eq. (5.3) along with their sum (red solid) and the zonal wind anomalies (black solid) from the control run (top) in EXP-C (bottom) in EXP-O [uvc = 2nd term of Eq. (5.3)] averaged from the top of the model to 700 hPa.

Figure 4.15. Zonal and ensemble-mean transient responses of 850-hPa zonal wind (unit: m s^{-1}) and vertically integrated eddy momentum flux

convergence (EMFC; unit: m s^{-2}) as a function of latitude and time in (left) EXP-C and (right) EXP-O experiments.

Figure 4.16. Anticyclonic wave breaking (AWB)-Cyclonic wave breaking (CWB) densities in time in EXP-C (green) and EXP-O (blue), respectively. All data displayed are the 11-days running mean of all 100 ensembles in each day. AWB and CWB events are computed following Strong and Magnusdottir (2008). See text for more details.

Figure 4.17. Zonal and ensemble-mean transient responses of Eady growth rate ($\sigma = 0.31g/(aN\theta_0)(\partial\bar{\theta}/\partial\phi)$, unit: 10^7 s^{-1}) as a function of latitude and time in (left) EXP-C and (right) EXP-O.

Figure 4.18. Schematic diagram for the possible dynamical mechanisms of the opposing HC-jet shifts under the global cooling condition. See Chapter 5 for the details.

Figure 5.1. The zonal-mean temperature (unit: K), zonal wind (unit: m s^{-1}), and mean meridional circulation (MMC; unit: $10^{10} \text{ kg s}^{-1}$) responses (top) in the LowSIC and (bottom) in the HighSIC. Note that the latitudinal range in (c, f) is different from others.

Figure 5.2. (a) The polar and tropical temperature changes in High-SIC (blue circle) and Low-SIC (skyblue triangle). (b) The HC edge shifts vs. jet latitude shifts High-SIC (blue circle) and Low-SIC (skyblue triangle).

Figure 5.3. Eddy momentum flux divergence differences (shading, unit: 10^{-5} m s^{-2}) in (a) LowSIC and (b) in HighSIC. The contours eddy momentum flux divergence in the LGM scenario.

Figure 5.4. Eddy heat flux differences (unit: K m s^{-1}) in (a) LowSIC and (b) in HighSIC (shading). The contours are eddy heat fluxes in LGM scenario. The negative eddy heat flux indicates the poleward (southward) eddy heat flux.

Figure 5.5. (a) Eddy heat fluxes at 850 hPa for all waves in LGM (solid blue), PI (solid black), LowSIC (dotted), and HighSIC (dashed) experiments (unit: $\text{m s}^{-1} \text{ K}$).

Figure 5.6. (a) Eddy heat fluxes at 850 hPa for all waves in LGM (solid blue), PI (solid black), LowSIC (dotted), and HighSIC (dashed) experiments (unit: $\text{m s}^{-1} \text{ K}$). (b, c) Same as (a) but (b) for long waves with a range of zonal wavenumber k from 1 to 5, and (c) for short waves with a range of zonal wavenumber from 6 and larger, respectively. Note that

the positive sign of the y axis indicates the poleward shift of the EHF in the SH.

Figure 7.1. The equilibrium temperature profile (black contours) and the additional tropical, q_{trop} , and polar thermal forcings, q_{pole} , for heating experiments. The additional forcings are introduced to mimic global-warming-like climate states, respectively. The contour intervals are 20 K, and shading intervals are 0.2 K day⁻¹.

Figure 7.2. Same as Fig. 3.10 but from heating experiments (q_{trop} , q_{pole}) = (0.3, 0.0), (0.0, 1.2), and (0.3, 1.2) K day⁻¹. The left column is identical to the one in Fig. 2 and is shown here for comparison purpose.

Figure 7.3. Same as Fig. 7.2 but with a stronger polar warming of (q_{trop} , q_{pole}) = (-0.3, 0.0), (0.0, 2.8), and (0.3, 2.8) K day⁻¹. The left column is identical to the one in Fig. 7.2 and is shown here for comparison purpose.

Figure 7.4. Same as Fig. 3.13 but for warming experiments. The experiments with opposing shifts of circulations, i.e., a poleward HC-edge shift and an equatorward jet-latitude shift, are denoted in dark red in (a). The three experiments, i.e., TROP-H, POLE-H, and COMB-H, are denoted with a black border. (b) The relationship between the HC-edge and jet-latitude changes in all experiments. The HC-jet change ratio to $q_{\text{trop}}=-0.3$ K day⁻¹ (orange) and $q_{\text{pole}}=-2.8$ K day⁻¹ (green) are denoted with colored lines. The one-to-one line is denoted with a dotted line in (b).

Figure 7.5. Same as Fig. 4.1 but for TROP-H (orange), POLE-H (green), and COMB-H (red). The maximum latitudes of U850, EMF250 convergence, and EHF850 are denoted with “X” in (a), (b), and (d), respectively. The zero-crossing latitudes for EMF250 divergence and Ψ 500 are denoted with “O” in (b) and (c), respectively.

Figure 7.6. EMF250 divergence cospectra (10^{-8} m s⁻², contours) as a function of angular phase speed and latitude in (a) CTRL, (b) TROP-H, (c) POLE-H, and (d) COMB-H. (b–d) The differences in EMF divergence in each experiment from CTRL (e.g., TROP-H *minus* CTRL) are shaded, with anomalous divergence in blue and convergence in red. Contours are depicted from -6×10^{-8} m s⁻¹ day⁻¹ to 6×10^{-8} m s⁻¹ day⁻¹ with intervals of 1×10^{-8} m s⁻¹ day⁻¹, and the shading range is from -5×10^{-8} m s⁻¹ day⁻¹ to 5×10^{-8} m s⁻¹ day⁻¹ with intervals of 0.4×10^{-8} m s⁻¹ day⁻¹. Thick and thin curves indicate the critical latitude and the reflective latitude for zonal wavenumber 6, respectively, for CTRL (gray) and cooling experiments (colored). Gray shaded phase speed range of -5 to 5 m s⁻¹ denotes a slow phase speed range.

Chapter 1. Introduction

1.1 Dynamics of Large-scale Circulation

The atmospheric general circulation is characterized by the Hadley cell (HC) in the tropics, and two jet streams: the subtropical jet and the eddy-driven jet (sometimes referred to as the subtropical jet or midlatitude jet). The Hadley cell, a thermally driven cell in the Earth, is strongly associated with the subtropical jet through strong vertical wind shear and strong temperature gradients. The eddy-driven jet, driven by the midlatitude eddies (e.g., extratropical cyclones) as the name indicates, exhibits a quasi-barotropic vertical structure. The circulations, such as the Hadley cell and the eddy-driven jet, are prominent features of extratropical dynamics. In particular, the midlatitude jet is often referred to as the southern annular mode, which has been widely documented (Thompson and Wallace 2000), with the associated Antarctic circumpolar current. In this thesis, the HC and the eddy-driven jet are focused on, and the eddy-driven jet will henceforth be referred to as the jet.

The formation of the HC is largely explained by the mass conservation by looking at the barotropic dynamics. The HC dynamics can be largely explained by starting from the primitive equation of zonal-mean zonal momentum can be written as below:

$$\frac{\partial \bar{u}}{\partial t} = -\frac{1}{a \cos^2 \varphi} \frac{\partial \overline{u'v'} \cos^2 \varphi}{\partial \varphi} + f \bar{v} - \bar{v} \frac{1}{a \cos \varphi} \frac{\partial \bar{u} \cos \varphi}{\partial \varphi} - \bar{\omega} \frac{\partial \bar{u}}{\partial p} - \frac{\partial (\bar{\omega}' \bar{u}')}{\partial p} + \frac{\bar{u}_{sfc}}{\tau} + R. \quad (1.1)$$

Here, overbars and primes denote the zonal mean and the deviation from the zonal mean. u and v are zonal wind and meridional wind, respectively. Other symbols are the standard Coriolis parameter (f), the radius of the Earth (a), and the damping coefficient of boundary layer friction (τ). φ is latitude, t is time, p is pressure, and the subscript sfc indicates the surface property. The first and second terms in the right-hand side of Eq. (1.1) indicate the convergence of meridional eddy momentum flux and the Coriolis force. The third, fourth, and fifth terms are meridional and vertical advection of zonal-mean zonal wind, and the convergence of vertical momentum fluxes, respectively. The last two terms represent the surface damping term and the residual term.

In the extratropics, the momentum budget is examined with quasi-geostrophic (QG) approximation. We neglect the terms related to the ageostrophic advection terms as well as the vertical eddy momentum flux term. After QG assumption, Eq. (1.1) can be re-written as the quasi-geostrophic zonal momentum equation (e.g., Lorenz and Hartmann 2001):

$$\frac{\partial \bar{u}}{\partial t} = -\frac{1}{a \cos^2 \varphi} \frac{\partial [\bar{u} \bar{v}'] \cos^2 \varphi}{\partial \varphi} + f[\bar{v}] - \frac{[\bar{u}_{sfc}]}{\tau} \quad (1.2)$$

In the steady state ($\frac{\partial \bar{u}}{\partial t} = 0$), Eq. (1.2) shows that the three terms on the right-hand-side (i.e., associated with the eddy momentum flux convergence, the Coriolis force, and the surface friction) can be balanced to each other. In particular, the first two terms are the major two terms that dominate the zonal momentum balance. Eq. (1.2) is also interpolated into the Rossby wave concept. In the midlatitudes where the stirring by Earth's rotation is strongest, the Rossby waves are generated via the Coriolis parameter and absolute vorticity gradient. Waves propagate away from the stirring region, generating the momentum fluxes ($[\bar{u} \bar{v}']$) in the opposite sense to wave propagation (Hoskins 1985). This leads to convergent momentum fluxes and accelerates the zonal mean flow by Eq. (1.2).

$$0 = -\frac{1}{a \cos^2 \varphi} \frac{\partial [\bar{u} \bar{v}'] \cos^2 \varphi}{\partial \varphi} + f[\bar{v}] - \frac{[\bar{u}_{sfc}]}{\tau} \quad (1.3)$$

In the upper branch of the Hadley circulation where the stream function is horizontal, the mean zonal momentum balance in a statistically steady state is approximately

$$(f + \bar{\zeta})\bar{v} = f(1 - R_o)v \approx S \quad (1.4),$$

with the relative vorticity in zonal mean $\bar{\zeta} = \frac{1}{a \cos \varphi} \frac{\partial \bar{u} \cos \varphi}{\partial \varphi}$, local Rossby number $R_o = -\bar{\zeta}/f$, and eddy momentum flux divergence S . This

typically holds in the upper branch near the center of the Hadley cell. If $R_o \rightarrow 0$, the mean meridional circulation ($f\bar{v}$) is tied to the eddy momentum flux divergence (S). On the other hand, if $R_o \rightarrow 1$, the eddy momentum flux approaches zero, and the mean meridional circulations are not well associated with the eddy momentum flux divergence. The local Rossby number is typically smaller in the summer hemisphere ($Ro \lesssim 0.2$) than in the winter hemisphere ($Ro \gtrsim 0.5$) (e.g., Schneider and Bordoni 2008), indicating that the summer hemisphere is under the zonal-mean dominant regime while the winter hemisphere is in the eddy-dominant regime.

1.2 Relationship between the HC edge and jet latitude

The HC edge is quantified as a zero-crossing latitude of the 500-hPa mass stream function. The 500-hPa mass stream function, Ψ_{500} , is defined by vertically integrating the zonal-mean meridional wind $[\bar{v}]$ from the top of the atmosphere to the 500-hPa pressure level as follows:

$$\Psi_{500} \equiv \frac{2\pi a \cos \varphi}{g} \int_{500 \text{ hPa}}^{500 \text{ hPa}} [\bar{v}] dp \quad (1.5)$$

where a , φ , and g represent the radius of the Earth, the latitude, and the gravitational acceleration, respectively. The bracket and overbar denote the zonal-mean and the time-mean, respectively.

The eddy-driven jet is defined as the zonal wind maximum in the lower troposphere. Unlike the subtropical jet, the eddy-driven jet has a quasi-barotropic structure in the vertical. In the SH, its latitudinal position is often defined from the zonal-mean zonal wind profile at 850 hPa. Following Adam et al. (2018), a trapezoidal interpolation method is applied to detect the latitudinal position of the maximum zonal wind from 35°S to 75°S. The cubic-spline method is also tested to investigate the method sensitivity. It turns out that the jet latitude derived from the trapezoidal integration is slightly different from that estimated from the cubic-spline method. However, their differences are minor, not changing the overall conclusions.

The HC edge and the eddy-driven jet are known to be related to each other, especially in the zonal-mean perspective (Son et al. 2009; Kang and Polvani 2011). The HC is a thermally direct circulation that is driven by radiative heating in the deep tropics. The driving mechanism of the HC can be understood in the context of an eddy-free, axis-symmetric flow (Held and Hou 1980). However, the HC edge, which is located in the subtropics, is primarily determined by the latitude where baroclinic instability becomes significantly strong (Held 2001). On the other hand, the eddy-driven jet, or the polar-front jet, is driven by baroclinic eddies in the midlatitudes. This is seen in the eddy-free state

of numerical models, which is also jet-free (Held and Hou 1980; Kim and Lee 2001).

By vertically integrating into the free atmosphere (1.2), the surface friction term can be neglected. By multiplying a few constants, (1.2) can be denoted as follow:

$$0 = -\frac{2\pi}{gf\cos\phi} \int_{0hPa}^{500hPa} \frac{\partial \overline{u'v'} \cos^2\phi}{\partial \phi} dp + \frac{2\pi a \cos\phi}{g} \int_{0hPa}^{500hPa} \overline{[v]} dp \quad (1.6)$$

The latitude where the vertically integrated meridional wind, the right term on the right-hand side, is zero is determined as the edge of the HC. Therefore, this equation indicates that the HC edge is associated with the upper-tropospheric eddy momentum flux convergence.

By repeating the vertical integration of Eq. (1.2) to the surface, one can also obtain the following relationship:

$$\overline{[u]} \approx -\frac{\tau}{a \cos^2\phi} \int_{top}^{sfc} \frac{\partial \overline{u'v'} \cos^2\phi}{\partial \phi} dp. \quad (1.7)$$

This equation indicates that the jet location, which is determined by a maximum zonal wind at the surface, is quantitatively established by column-integrated EMF convergence.

Equations (1.6) and (1.7) reveal that both the HC edge and jet latitude are primarily determined by EMFs. The HC edge, that is, the zero-crossing latitude of Ψ_{500} , is then located at the zero-crossing latitude of

the EMF convergence maximum. The jet latitude, defined by the latitude of zonal wind maximum, is primarily associated with the latitude of the column-integrated EMF convergence. Since the eddy momentum flux is strongest in the upper troposphere, it is apparent that the HC edge and jet latitude would be remarkably controlled by the latitudinal distribution of the EMF ($\overline{u'v'}$) in the upper troposphere (Walker and Schneider 2006; Lu et al. 2008). As shown in the previous section, the dynamical relationship is strongly held in the winter when the mean meridional circulation is linked to the eddy momentum flux convergence (Kang and Polvani 2011).

1.3 Circulation changes from paleo to warm climates

The atmospheric general circulation is often characterized by the HC in the tropics and the eddy-driven jet (hereafter simply “jet”) in the midlatitudes. These are two key factors that affect global hydroclimate, ocean currents, and air-sea interactions. For instance, the poleward edge of the HC and its variability modulate precipitation and the water cycle in the subtropics. The jet is closely related to storm track activities, controlling midlatitude precipitation. In the Southern Hemisphere (SH), the jet also plays a crucial role in determining the Antarctic circumpolar

currents and the global overturning circulation in the oceans, affecting the global carbon cycle (e.g., Marshall and Speer 2012).

1.3.1 Recent circulation changes

The HC and the westerly jet, two prominent features of Earth's atmospheric general circulation, play a key role in redistributing the Earth's energy (e.g., Lau and Kim 2015) and affecting the surface weather and further global climate change (e.g., Marshall and Speer 2012). The circulation changes in the recent few decades have received much attention with the associated increased anthropogenic forcings: tropical expansion and a poleward shift of the jet in the midlatitudes (Davis and Rosenlof 2012; Choi et al. 2014; Lucas et al 2014, Waugh et al 2018). Recently, it is observed that the anthropogenic-forced response of the HC edge has emerged over the natural variability, especially in the Southern Hemisphere (SH) (e.g., Grise et al 2019, Grise and Davis 2020). Such robust tropical expansion in the SH is known to be predominantly derived by greenhouse gases (GHGs) and stratospheric ozone (e.g., Son et al. 2010). Recently, anthropogenic aerosols (AER), which are the only driver of the opposite response of circulation, have received much attention (Rotstayn et al 2013, Choi et al. 2019).

In recent years, evidence has accumulated that both the poleward edge of the HC and the eddy-driven jet latitude have shifted poleward in the recent few decades. They have shifted poleward during the last few decades in both hemispheres (Hu and Fu 2007; Seidel et al. 2008; Ceppi et al. 2013; Lucas et al. 2014; Lee et al. 2019). This is especially true in the SH (e.g., Lucas et al. 2014). Such circulation changes are projected to continue in future climate as global warming is enhanced (e.g., Lu et al. 2008; Barnes and Polvani 2013; Son et al. 2018a; Grise et al. 2019), affecting the global water budget, midlatitude weather, and ocean circulation, among many others (e.g., Russell et al. 2006; Lau and Kim 2015). Although these changes are often statistically insignificant due to rather short observational records and uncertainties in the reanalysis products (Lucas et al. 2014; Mantsis et al. 2017), they are evident in climate model simulations (Gerber and Son 2014; Grise et al. 2019), particularly in the SH where the long-term trend of circulation is greater than the natural variability (Staten et al. 2018; Grise et al. 2019). In particular, the HC expansion is found in most coupled model simulations. The datasets archived for the Coupled Model Intercomparison Project phase 5 (CMIP5, Taylor et al. 2012) show a systematic poleward shift in the HC edge under various warming scenarios such as the Representative Concentration Pathway (RCP) (Lu

et al. 2008; Hu et al. 2013; Choi et al. 2019) and Extended Concentration Pathway (ECP) scenarios (Chavailaz et al. 2013; Son et al. 2018a). Likewise, a poleward shift in the jet latitude is found in the CMIP5 future scenario runs (Barnes and Polvani 2013; Vallis et al. 2015). Although these changes are found in both hemispheres, they are expected to be larger in the SH than in the Northern Hemisphere (Hu et al. 2013; Barnes and Polvani 2013).

The model simulations further show that the long-term trends of the HC edge and jet latitude are linearly correlated with each other, especially in the SH (Son et al. 2018a; Waugh et al. 2018). Multi-model analyses revealed that their trends in austral summer have a 1:2 ratio, indicating that a poleward shift of the SH-summer jet latitude of 2° is roughly associated with a poleward shift in the SH-summer HC edge of 1° (Gerber and Son 2014). Such a linear relationship, which is not evident in the Northern hemisphere, is also found in the CMIP5 and chemistry-climate model simulations (Son et al. 2018a).

With increasing evidence of a recent poleward shift of the HC edge, particularly in the SH (e.g., Hu and Fu 2007; Seidel et al. 2008; Lucas et al. 2014), a great deal of research has focused on how the circulation will respond to external forcing associated with climate change (e.g., Butler et al. 2010; Gerber and Son 2014; Screen et al. 2018; Son et al.

2018a). Global warming projections show a prominent temperature increase both in the upper tropics and at the polar surface, which effectively reduces the meridional temperature gradient in the lower level and increases the upper-level temperature gradient. Although general circulation changes are influenced by multiple factors, the most pronounced changes are often explained by the opposing effects of polar surface warming versus tropical upper-tropospheric warming in response to increased greenhouse gases (e.g., Butler et al. 2010; Yuval and Kaspi 2016). The former leads to a reduced meridional temperature gradient in the lower troposphere, while the latter results in an increased temperature gradient in the upper level. The poleward shift of the HC edge, or the HC expansion, is mainly caused by the upper-level increased temperature gradient and subtropical static stability mostly due to the enhanced tropical upper-tropospheric warming than the low-level warming (e.g., Lu et al. 2008; Grise and Polvani 2016; Son et al. 2018b). Unlike the HC, the jet is influenced by both the upper- and lower-level temperature gradient changes (e.g., Butler et al. 2010; Barnes and Screen 2015). The jet shifts poleward in response to polar amplification and shifts equatorward in response to tropical warming (e.g., Butler et al. 2010; Barnes and Screen 2015; Screen et al. 2018). This is particularly true in the Northern Hemisphere. Since the polar amplification is not

evident over the Antarctic, the poleward shift of the jet has been mainly attributed to the subtropical upper-tropospheric warming in the SH.

The jet shift to climate change is understood by the counterbalancing influences of tropics and polar surface temperature changes under global warming (e.g., Barnes and Screen 2015; Grise and Polvani 2016). However, their detailed mechanisms remain obscure. Numerous studies elaborate on the poleward shift of the jet under global warming conditions (Chen et al. 2007; 2008; 2013; Kidston 2010; 2011; Kidston and Vallis 2012; Lorenz 2014; Lu et al. 2008; Riviere 2011). Chen et al. (2007;2008) pointed out the wave absorption change at the upper level. Kidston et al. (2010;2011) suggested that an increase in the zonal wavenumber of waves under global warming plays a pronounced role in shifting the jet poleward. A bunch of studies has focused on the changes in the dissipation of wave activity on the poleward flank of the jet. Chen et al. (2013); Lu et al. (2008) stressed the increased vertical propagation of waves from the lower level. On the other hand, Kidston and Vallis (2012) and Lorenz (2014) argued that wave reflection changes are further important. Riviere (2011) provides that the enhancement of lower-level baroclinicity change would contribute to the increase in anticyclonic wave-breaking events, further pushing the jet poleward.

1.3.2. Circulation changes in the paleoclimate

In the LGM conditions, the concentration of CO₂ decreases by up to 90 parts per million due to oceanic storage of the excess carbon (Sigman et al. 2010). The latitudinal shifts in the SH westerlies are invoked as a possible cause of enhanced ocean storage mechanisms. An equatorward shifted westerly jet could suppress deep water ventilation, leading to carbon becoming trapped in cold dense waters (Toggweiler et al. 2006; Denton et al. 2010). Kim et al. (2003) presented an important role of the dynamic response of the ocean associated with the surface wind change in the LGM climate in the coupled model.

Despite such importance of understanding the LGM circulations, previous studies are mostly focused on the present and future climate. However, recent studies have shown that the HC edge and jet latitude do not necessarily move in the same direction even in the SH in the cold climate (Chavaillaz et al. 2013; Kim and Son 2020, hereafter KS20). KS20 showed that the SH HC edge and jet latitude shift to the opposite direction in the Last Glacial Maximum (LGM, 21,000 years ago) winter in the general circulation models (GCMs) archived for the Paleoclimate Modeling Intercomparison Project phase 3 (PMIP3; Braconnot et al. 2012). While the SH HC edge in the LGM climate is robustly located on the equatorward side of the one in the pre-industrial (PI) climate

(D'Agostino et al. 2018; Son et al. 2018b; Wang et al. 2018), the jet latitude appears on the poleward side of its counterpart in the PI condition in a few LGM simulations (e.g., Chavaillaz et al. 2013).

Based upon the above findings, it is evident that the coherent HC-jet change in the present and future climates does not hold in the paleoclimate. Toggwiler and Russell (2008) first proposed an equatorward jet shift in the SH in the LGM, arguing that an equatorward-shifted jet might lead to a weaker CO₂ uptake in the Southern Ocean in the paleoclimate. However, the PMIP3 models showed that the jet in the LGM does not always shift equatorward compared to the PI scenario (Chavaillaz et al. 2013; Rojas 2013; Harrison et al. 2015). Since the HC edge systematically shifts poleward from the LGM to the future scenarios (see also Son et al. 2018b), this gives a hint of a possible opposing change in HC edge and jet latitude from the PI to LGM scenarios. Their relationship, however, has not been quantitatively examined.

Previous studies suggested this opposing change in a cold climate is likely due to polar cooling amplification over Antarctica. Unlike global warming simulation, LGM simulation shows a pronounced Antarctic cooling due to thickened land ice. This acts to increase the meridional temperature gradient in the lower troposphere (Sime et al. 2016; Kim et al. 2017), strengthening the jet poleward compared to the

PI condition (Chavaille 2013; KS20). This is exactly opposed to the projected Arctic amplification in a future climate. In contrast, reduced static stability in the subtropics due to an enhanced cooling in the upper level than in the lower level maintains the HC edge on the equatorward side of the one in the PI condition.

1.4 Aims of the Thesis and Outline

Although previous studies help us to understand the eddy influence on the HC edge and jet latitude, some questions related to the HC-jet relationship in the LGM conditions remain to be explored. The HC-jet relationship in global cooling conditions, however, has not been quantitatively explored. It is particularly unclear whether the linear HC-jet relationship in a recent climate hold in the paleoclimate, and if not, what makes the difference, or a possible cause of the relationship change, and finally how the eddies act in the HC-jet in a cold climate.

The main purpose of this study is to improve our dynamical understanding of the HC-jet relationship in detail. Therefore, we attempted to answer these questions as follows:

- 1) Is the linear HC-jet relationship in global warming conditions held in global cooling conditions? (Chapter 3)

2) If not, what makes the difference in the HC–jet relationship?

(Chapter 3)

3) What are the dynamical mechanisms for the HC–jet relationship in cold climates? (Chapter 4)

4) Is the dynamic processes held in the comprehensive models?

(Chapter 5)

5) Can the opposing HC–jet change occur in the future? (Chapter 7)

To do so, we first identify the long-term HC–jet relationship in the SH in the global climate models from cold to warm climates (Chapter 3). We expect the HC and jet to move in an opposite direction to each other, which is called “*opposing* HC–jet change.” Secondly, we examine the relationship between the HC edge and jet latitude in an equilibrium simulation using an idealized dry dynamic model (Chapters 3 and 4). Two thermal forcing parameters, which are determined based on the comprehensive model results, are varied in a wide range to fully investigate the favorable condition for the opposing HC–jet change. A subset of simulations in Chapter 3 is further analyzed in detail in terms of Rossby wave dynamics to find out a possible mechanism for the opposing HC–jet change (Chapter 4). The transient experiments are also performed using the same idealized model to further investigate the evolution of the circulation changes in the global cooling-like simulations

(section 4.7). In Chapter 5, the above findings are briefly repeated for the LGM simulations in a comprehensive model with varying sea ice concentrations.

The rest of this paper is organized as follows. Chapter 2 provides the model descriptions and methods. In Chapter 3, the zonal-mean responses of the HC edge and eddy-driven jet latitudes from paleo to future climates is investigated by using the atmospheric-oceanic coupled climate models in Chapter 3. Such an HC–jet relationship is reproduced by using a simplified GCM, particularly for the global cooling condition. The role of eddies in the opposing HC–jet change is discussed in Chapter 4 by examining the equilibrium and transient simulations. The role of sea ice in the coupled climate model is explored in Chapter 5. Chapter 6 provides conclusions and the extension of the idealized model study but for global warming-like experiments. A number of contents in Chapter 3 are from Kim and Son (2020), and the contents in Chapter 4 are from Kim and Son (2023).

Chapter 2. Data and Methods

2.1 Coupled models: CMIP5, PMIP3, PMIP4

The present chapter analyzes the three sets of climate model simulations as in Son et al. (2018a). They are the LGM, PI, and ECP4.5 simulations (Table 2.1). Note that, unlike previous studies that have mainly analyzed the RCP scenarios, this study examines the ECP4.5 scenario, targeting an equilibrium state in the 23rd century. Expanding upon Son et al. (2018a), who analyzed only six models that provide all three sets of simulations (denoted with an asterisk in Table 1), all available models are used to better quantify the circulation differences between the LGM and PI scenarios and those between the ECP4.5 and PI scenarios.

All analyses are performed with the last 100 years of each simulation. The two exceptions are the ECP4.5 simulations of FGOALS-g2 (2201-2275) and CCSM4 (2201-2299), whose data records are slightly shorter than 100 years. Although several models provide multiple ensemble members, only the first ensemble members (r1i1p1) are used by assuming that 100-year-long data effectively reduce the uncertainty in zonal-mean circulation change. An exception is GISS-E2-R in which r1i1p150 run for the LGM scenario and r1i1p151 run for the PI scenario

are used because r1i1p1 run is not available. Each model has a different horizontal resolution ranging from $0.9^{\circ}\times 1.25^{\circ}$ to $2.8^{\circ}\times 3.0^{\circ}$ (Table 1). The varying resolutions are interpolated to a common resolution of $2.5^{\circ}\times 2.5^{\circ}$ and at 17 pressure levels to reduce the resolution influence in determining the HC edge and jet latitude.

A multi-model mean (MMM) is calculated by averaging all 9, 14, and 11 models of the LGM, PI, and ECP4.5 simulations, respectively. The MMM difference is computed by averaging the LGM-PI differences of 9 models and the ECP4.5-PI differences of 11 models.

In all analyses, the HC edge and jet latitude are computed with annual or seasonal mean data and averaged over the analysis period (100 years in most cases). The statistical significance of the LGM-PI differences and the ECP4.5-PI differences is evaluated at the 95% confidence level by using the two-tailed Student's t-test, with a null hypothesis of equal averages in the two independent samples.

Table 2.1. CMIP5 and PMIP3 models used in this study. The six models, which provide all three experiments, are indicated by asterisks. The analyzed simulation is denoted with “O”.

ID number	Model	Horizontal resolution	LGM	PI	ECP4.5
1	CCSM4*	$0.9^{\circ}\times 1.25^{\circ}$	O	O	O
2	CESM1-CAM5	$0.9^{\circ}\times 2.5^{\circ}$	-	O	O
3	CNRM-CM5*	$1.4^{\circ}\times 1.4^{\circ}$ (T127)	O	O	O

4	COSMOS-ASO	T31 (3.75°x3.75°)	0	0	-
5	CSIRO-Mk3-6-0	1.9°x1.9°	-	0	0
6	FGOALS-g2*	2.8°x3°	0	0	0
7	GISS-E2-R*	2°x2.5°	0	0	0
8	IPSL-CM5A-LR*	1.875°x3.75°	0	0	0
9	IPSL-CM5A-MR	1.9°x2.5°	-	0	0
10	MIROC-ESM*	2.8°x2.8° (T42)	0	0	0
11	MPI-ESM-LR	1.9°x1.9° (T63)	-	0	0
12	MPI-ESM-P	1.9°x1.9° (T63)	0	0	-
13	MRI-CGCM3	1.1°x1.1°	0	0	-
14	NorESM1-M	1.9°x2.5°	-	0	0

The three PMIP phase 4 (Kageyama et al. 2018) models which have both LGM and PI scenarios, i.e., AWI-ESM-1-1-LR, MIROC-ES2L, and MPI-ESM1-2-LR, are investigated (Table 3).

Table 2.3. PMIP4 models used in this study.

ID number	Model	Horizontal resolution	Vertical resolution
1	AWI-ESM-1-1-LR	T63 (~1.8°x1.8°)	L47
2	MIROC-ES2L	T42 (~2.8°x2.8°)	L40
3	MPI-ESM1.2-LR	T63 (~1.8°x1.8°)	L47

2.2 Configuration for simplified dry dynamic core

2.2.1 Model description

All experiments are performed using a dynamic-core GCM developed by the Geophysical Fluid Dynamics Laboratory (GFDL), which was used in KS20. This model is set to have a spectral resolution of a

triangular truncation at wavenumber 85 and is vertically divided into 40 sigma levels. Each experiment is integrated for 5,500 days, and the last 5,000 days are analyzed by discarding the first 500 days as an initial spin-up.

This model is forced by relaxing temperature to a radiative equilibrium temperature profile (T_{eq}). In this study, the T_{eq} of Held and Suarez (1994) is used with a minor modification to mimic austral winter conditions (contours in Fig. 2.1):

$$T_{eq}(\phi, p) = \max \left\{ 200 \text{ K}, [T_0 - \Delta_h(\sin^2\phi - 2\sin\phi_0\sin\phi) - \Delta_v \log\left(\frac{p}{p_0}\right) \cos^2(\phi)] \left(\frac{p}{p_0}\right)^{Rc_p^{-1}} \right\}, \quad (3.1)$$

where ϕ is latitude, ϕ_0 is the thermal equator ($= 6^\circ\text{N}$), p is pressure, p_0 is the reference surface pressure ($= 1000 \text{ hPa}$), T_0 is the surface temperature at the equator ($= 315 \text{ K}$), Δ_h is the equator-to-pole temperature difference ($= 60 \text{ K}$), Δ_v is the static stability parameter ($= 10 \text{ K}$), R is the gas constant of the air, and c_p is the specific heat capacity at constant pressure ($Rc_p^{-1} = 2/7$). Topography is not included as this study aims to understand the SH circulation changes.

2.2.2 Cooling experimental setup: Equilibrium simulation

The dynamical-core GCM has been widely used to examine the atmospheric circulation response to global warming-like thermal forcings (e.g., Butler et al. 2010; Sun et al. 2013; Barnes and Screen 2015). Following Butler et al. (2010), the zonally-symmetric thermal forcings are imposed in the tropical upper troposphere and in the polar lower troposphere:

$$Q_{\text{trop}}(\phi, p) = q_{\text{trop}} \exp \left\{ - \left[\frac{(\phi - \phi_{\text{trop}})^2}{2\sigma_\phi^2} + \frac{(p - p_{\text{trop}})^2}{2\sigma_p^2} \right] \right\}, \quad (2)$$

$$Q_{\text{pole}}(\phi, p) = q_{\text{pole}} \cos \left[(\phi - \phi_{\text{pole}})^{15} \right] \exp \{ 4(p - p_{\text{pole}}) \} \quad (3).$$

In Eq. (2), the tropical forcing, Q_{trop} , is controlled by its latitudinal and vertical locations with a meridional width of σ_ϕ and vertical width of σ_p . It is placed over the thermal equator (i.e., $\phi_{\text{trop}} = \phi_0 = 6^\circ\text{N}$) at 300 hPa ($p_{\text{trop}} = 300$ hPa) with $\sigma_\phi = 20^\circ$ and $\sigma_p = 125$ hPa. The polar forcing, Q_{pole} , is confined near the surface with $\phi_{\text{pole}} = 90^\circ\text{S}$ and $p_{\text{pole}} = 1000$ hPa. These parameters are set to mimic LGM-like and global warming-like temperature changes (Fig. 3.1; see also Son et al. 2018b; KS20). The LGM and future temperature changes are pronounced by global cooling and warming, respectively, particularly enhanced in the tropics in the upper troposphere and the near-surface polar region (see

Fig. 3.1). Note that the width of Q_{trop} is considered relatively broad to produce the global warming or cooling-like climate change, which is different from a narrow El-Niño-like forcing (e.g., Lu et al. 2008; Sun et al. 2013).

The forcing amplitudes, q_{trop} and q_{pole} , are varied independently to explore a wide range of climate states and competing individual influences on HC edges and jet latitudes. Both negative values (LGM-like states) and positive values (global-warming-like states) are considered. By varying q_{trop} and/or q_{pole} , a parameter sweep experiment is performed. In this study, q_{trop} is varied from -0.3 to -0.7 K day⁻¹ in 0.2 K day⁻¹ increments for cooling experiments. A stronger polar forcing is imposed by varying q_{pole} from -0.8 to -3.2 in 0.4 K day⁻¹ increments for cooling experiments. The multiple forcing experiments are also performed by setting non-zero q_{trop} and q_{pole} . All experiments conducted in this study are summarized in Table 2.4. They are compared with the control run with no thermal forcing, hereafter referred to as CTRL.

Table 2.4. Summary of model experiments.

		Tropical forcing experiments	Polar forcing experiments	Multiple forcing experiments
Heating experiment	q_{trop} (K day ⁻¹)	0.3, 0.5, 0.7	0	0.3, 0.5, 0.7
	q_{pole} (K day ⁻¹)	0	0.8, 1.2, 1.6, 2.0, 2.4, 2.8, 3.2	0.8, 1.2, 1.6, 2.0, 2.4, 2.8, 3.2
Cooling experiment	q_{trop} (K day ⁻¹)	-0.3, -0.5, - 0.7	0	-0.3, -0.5, -0.7
	q_{pole} (K day ⁻¹)	0	-0.8, -1.2, -1.6, -2.0, -2.4, -2.8, -3.2	-0.8, -1.2, -1.6, -2.0, -2.4, -2.8, -3.2

2.2.3. Cooling experimental setup: Transient simulation

To identify the role of polar cooling in shifting the poleward shift of the jet, we focus on the two transient experiments: one with tropical cooling (q_{trop}) of -0.3 K day⁻¹ (referred to as EXP-C) and polar cooling (q_{pole}) of -1.2 K day⁻¹ and the other with tropical cooling of -0.3 K day⁻¹

and polar cooling of -3.2 K day^{-1} (referred to as EXP-0). The former corresponds to the coherent, and the latter is expected to the opposing HC-jet change in the equilibrium simulations (See Fig. 3.13a).

The 100-member ensembles of transient experiments are run wherein the forcing is abruptly turned on. The purpose of these transient experiments is to dissect the processes of the evolution from the initial control state to the new forced equilibrium. Each ensemble of transient simulations branches out from every 50th day of the last 2000 days of the control simulation. For each of ensemble, the same thermal forcings are switched on at the first day and the model integrates for 200 days.

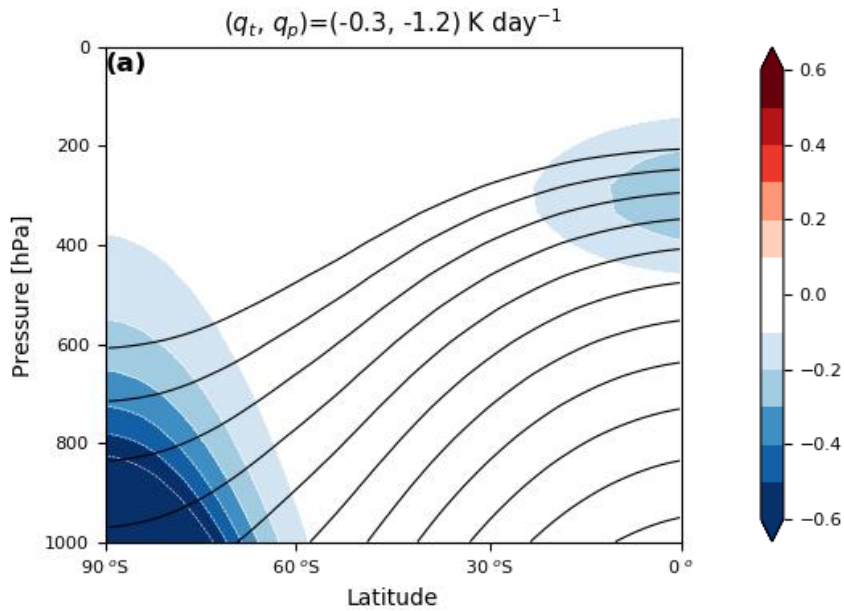


Figure 2.1. The equilibrium temperature profile (black contours) and the additional tropical, q_{trop} , and polar thermal forcings, q_{pole} , for cooling experiments. The additional forcings are introduced to mimic LGM-like

climate states, respectively. The contour intervals are 20 K, and shading intervals are 0.2 K day^{-1} .

2.2.4. Axisymmetric (2D) experiment

To separate the eddy responses from the mean quantities, the axisymmetric model is performed. All other settings are identical to the model described in section 3.2.1, except for a few modifications for the zonally-symmetric circulation. Following Kim and Lee (2001), the value of vertical diffusion coefficient k_v is chosen as $-2.0 \text{ m}^2 \text{ s}^{-1}$ and the diffusion $-20 \text{ m}^2 \text{ s}^{-1}$ of k_f to remove small-scale perturbation. The control run in the axisymmetric model is called 2D_CTRL. The three sets of cooling perturbations $(q_{\text{trop}}, q_{\text{pole}}) = (-0.3, 0.0)$, $(0, -2.8)$, and $(-0.3, -2.8) \text{ K day}^{-1}$, are applied, referred to as 2D_TROP-C, 2D_POLE-C, and 2D_COMB-C, respectively. All experiments are analyzed for 500 days after discarding 1000-days of data as a spin up. The 2D experiments are elaborated on in section 4.3.

2.3 AGCM description and experimental design

2.3.1 Model description

We examine the output from the Community Earth System Model version 1 (CESM1; Hurrell et al. 2013). CESM1 consists of interactive atmosphere, ocean, land, and sea ice component models. The

atmospheric model component is Community Atmosphere Model version 5.3 (CAM5.3; Neale et al. 2012). The Community Land Model version (CLM4.5; Oleson et al. 2013) is used as the land model component here. The spatial resolutions of the atmosphere and land model components are the same as 1.9° by 2.5° . Sea ice and land ice model components in this model are Community Ice Code version 4 (CICE4) and Glimmer-Community Ice Sheet Model version 1.9 (Glimmer-CISM1.9), respectively. The land ice model components include the ice on the Antarctic and Greenland so that the sea-ice feedback can be rapidly applied via the land ice model component. For the ocean model component, Parallel Ocean Program version 2 (POP2) is utilized with the same spatial resolution to the land-sea model component of 1° by 1° . The model description is briefly summarized in Table 2.5. To examine the eddy activities, daily mean data are analyzed.

Table 2.5. CESM model description used in Chapter 5.

Model		Resolution
Atmosphere	NCAR Community Atmosphere Model (CAM) 5.3	$1.9^\circ \times 2.5^\circ$
Land	Community Land Model (CLM) 4.5	

Ocean	Parallel Ocean Program (POP) 2	$1.0^{\circ} \times 1.0^{\circ}$
Sea ice	Community Ice Code (CICE) 4	
Land Ice	Glimmer-CISM 1.9	-

2.3.2 Experimental design

To identify the responses of the circulations in the LGM and PI conditions in this model, we performed three experiments referred to as LGM, PI, and PI_LGMSIC. Among them, two experiments have the same boundary conditions to PMIP3 protocols for the LGM and PI conditions. This PI-LGMSIC experiment is designed based on the equilibrium results from the two experiments. To examine the role of sea ice on the SH circulations in LGM conditions, we designed an experiment where the sea ice concentration is only preserved at the LGM condition. In other words, the SIC is held at the LGM scenario's level but other atmospheric boundary conditions in this PI-LGMSIC experiments are identical to the PI simulations.

To compare the sea-ice impact, two experiments are newly determined as follows:

- 1) LowSIC: LGM *minus* PI_LGMSIC experiments
- 2) HighSIC: LGM *minus* PI experiments

In the first set, we compared the LGM experiment with fixed SIC at the LGM level (LowSIC). Secondly, the HighSIC experiment presents the comparison of the LGM experiment to the PI experiment. By looking at the HighSIC, we can quantify the impacts of full LGM conditions, such as the sea-ice concentration, the increased ice sheet, their interactions to the atmosphere, and so on. By comparing LGM-SIC and LGM-XSIC experiments, we could verify the role of SIC.

To investigate the equilibrium response, the last 50 years-long data from each of the experiments are analyzed after discarding the first 200 years. All results which are further shown in sections 3.1 to 3.3 are analyzed based on the austral winter (June-July-August; JJA).

2.4 Analysis methods

2.4.1 Eddy spectra analysis

We first examine decomposing the EMF convergence into discrete phase speeds (c), eddies' phase speeds are examined in the opposing HC-jet cases. The spectra are primarily confined between two critical latitudes (where $\bar{u}/\cos\phi=c_A$) defined by the time-mean flow at this upper-tropospheric level. Faster waves' propagation is restricted into the regions near the jet core, and somewhat equatorward of the jet

maximum, whereas slower waves, which are so-called low-frequency eddies, propagate into the deep tropics.

Based on the linear theory, Rossby waves' propagation, reflection, and breaking are dependent on the wavelength as well as the phase speed. It is also known that the long and short waves act differently on the jet change: long waves are responsible for the broadening of the jet while short waves contribute to the shift of the jet (e.g., Lorenz and Hartmann 2001; Son and Lee 2005; O'Rourke and Vallis 2016).

2.4.2 Refractive index and reflective level

Following Harnik and Lindzen (2001), we use the critical and reflective profiles to analyze changes in wave propagation and the locations of wave breaking. The critical and reflective profiles are quantified through a refractive index, which is one of the measures of wave propagation and reflection. The specific latitude and level of each layer are dependent on the wavenumber and phase speed. Starting from the quasi-geostrophic potential vorticity (PV) conservation equation, the zonal-mean refractive index squared is given by

$$n_{ref}^2 = N^2 \left[\frac{a\bar{q}_\phi}{\bar{u}-c} - \frac{k^2}{\cos^2\phi} - a^2 f^2 F(N^2) \right], \quad (4.1)$$

where c is the zonal phase speed, N is the buoyancy frequency, Ω is the planetary rotation rate, a is the radius of the earth, p is pressure, N^2

is the buoyancy frequency, k is the zonal wavenumber, and h is the density scale height ($\rho = \rho_0 e^{-z/h}$) as equation (C2) in Harnik and Lindzen (2001). Here the definitions of F and meridional PV gradient are the same as in Harnik and Lindzen (2001).

Waves preferentially propagate toward regions where the refractive index is high, such as those within a jet core (Vallis 2006). They are reflected where the refractive index approaches zero and break where the refractive index approaches infinity. The reflective latitude is defined as the latitude where the refractive index is equal to zero at the 250-hPa level. Likewise, the critical latitude is the latitude where the refractive index becomes infinite or zonal-mean zonal wind is equal to the phase speed of the wave.

Chapter 3. Opposing HC–jet change in the Last Glacial Maximum

In this chapter, we explore the overall relationship between the HC edge and jet latitude changes in a wide range of climates covering the LGM, PI, and ECP4.5 states. Motivated by Toggwiler and Russell (2008), only the SH circulation is considered as any circulation change in the SH can be quantified in the zonal-mean context. Unlike previous studies, all available models archived for the PMIP3 and CMIP5 are utilized.

It is confirmed that the HC edge and jet latitude do not necessarily change in the same direction from the PI to LGM scenarios. This is in stark contrast to a coherent poleward shift of both the HC and jet from the PI to ECP4.5 scenarios. The opposing HC edge and jet latitude changes in the LGM are briefly discussed in terms of the interannual co-variability, the model mean biases, and the relative importance of tropical versus polar temperature changes. The possible impacts of external thermal forcings on the HC and jet changes are further explored by conducting idealized model experiments.

3.1. Zonal-mean responses

Figure 3.1 illustrates the responses of zonally-averaged temperature, mass stream function, and zonal wind to the LGM and ECP4.5 forcings. The temperature response to increasing greenhouse gas concentrations, which is quantified by the MMM ECP4.5-PI difference, shows a well-known pattern of strong tropical upper-tropospheric warming and polar lower-tropospheric warming (Fig. 3.1a). A similar temperature response is also found in the MMM LGM-PI difference with a comparable amplitude but in an opposite sign (Fig. 3.1d), indicating a strong cooling in the tropical upper troposphere and polar lower troposphere (see also Chavaillaz et al. 2013; Son et al. 2018b). Note that the Antarctic cooling in the LGM scenario is much stronger than the Antarctic warming in the ECP4.5 scenario. This is partly due to the thickened ice sheet and enhanced polar amplification around the Antarctic ocean in the LGM scenario.

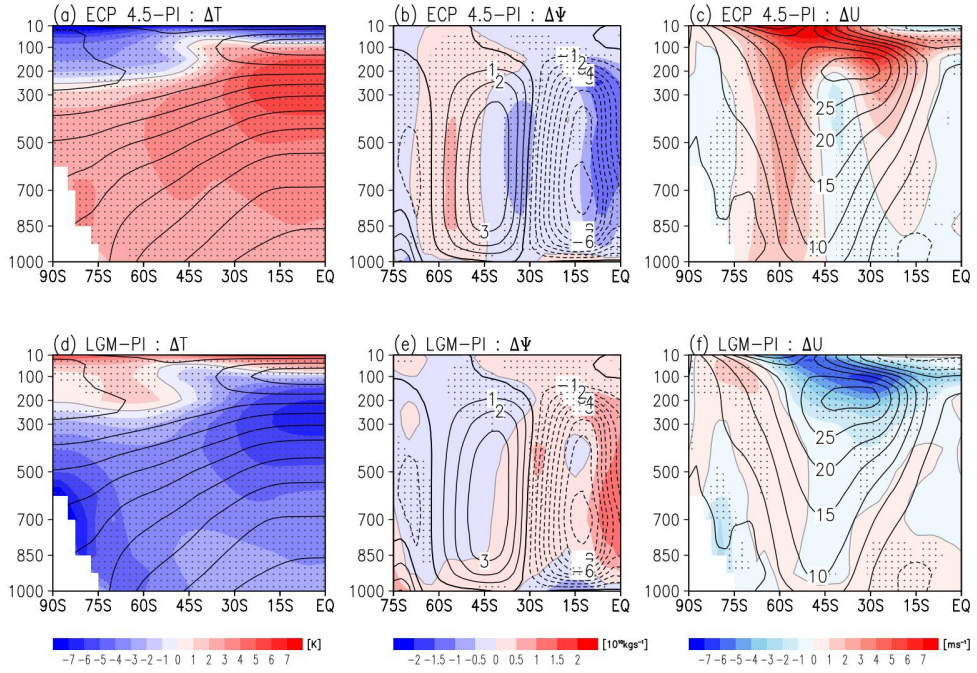


Figure 3.1. Multi-model-averaged annual-mean zonal-mean temperature (left), mass stream function (middle), and zonal wind (right) in PI simulation (contours), ECP4.5-PI (top) and LGM-PI (bottom) differences are shaded. Units are K for temperature, $10^{10} kg s^{-1}$ for mass stream function, and $m s^{-1}$ for zonal wind. The dotted region indicates that more than 80% of the models show the same sign. Note that the latitudinal range of (b, e) is different from the others.

The mass stream function under the PI scenario and its change in response to global warming or cooling are illustrated in Figs. 3.1b and 3.1e. The HC is characterized by a negative mass stream function in the tropics, indicating a counterclockwise circulation (dashed contours in Figs. 3.1b and 3.1e). Its outer edge is located near $30^{\circ}S$. The MMM ECP4.5-PI difference shows a negative value (blue shading) at the HC edge. This indicates a poleward shift of the HC edge in the future climate

(Fig. 3.1b). The opposite is also true in the MMM LGM-PI difference, indicating a relatively narrow HC in the LGM compared to the PI scenarios (Fig. 3.1e). Figure 3.2 further shows that the HC edge shifts poleward from the PI to ECP4.5 scenarios (Fig. 3.2a) but equatorward from the PI to LGM scenarios (Fig. 3.2b). This result, revealing a poleward shift of the SH HC edge from the LGM to PI and then to ECP4.5 scenarios, confirms the key finding of Son et al. (2018b).

The zonal wind shows a more complicated response to the LGM and ECP4.5 forcings (Figs. 3.1c and 3.1f) than the mass stream function. The MMM ECP4.5-PI wind difference (Fig. 3.1c) is generally positive on the poleward flank of the PI jet ($\sim 45^\circ\text{S}$). This indicates a poleward shifted and intensified SH jet in a warm climate (Fyfe and Saenko 2006; Wilcox et al. 2012; Barnes and Polvani 2013). More importantly, most models show the same signed ECP4.5-PI wind difference near the PI jet (see the dotted region in Fig. 3.1c). The MMM LGM-PI zonal wind difference, however, exhibits only small values around the PI jet. On average, it is less than 1 m s^{-1} and this change is not systematic across the models. As hinted from the non-dotted region in Fig. 3.1f, each model shows a different wind change around the PI jet.

A systematic poleward jet shift from the PI to ECP4.5 scenarios but a non-robust jet change from the PI to LGM scenarios is further

confirmed by examining each model's annual-mean circulation changes (Fig. 3.2). All 11 models show a poleward jet shift from the PI to ECP4.5 scenarios (Fig. 3.2a). All models show statistically significant changes. The resulting jet shift is on average approximately 1.5° latitude with two models (i.e., IPSL-CM5A-LR and IPSL-CM5A-MR) showing $3\text{--}4^\circ$ latitude shift. Such changes do not appear in the LGM-PI differences (Fig. 3.2b). While three models (i.e., CNRM-CM5, GISS-E2-R, and IPSL-CM5A-LR) show a significant equatorward jet shift, four models (i.e., FGOALS-g2, MIROC-ESM, MPI-ESM-P, and MRI-CGCM3) show a significant poleward jet shift as in the ECP4.5-PI differences. As a result, the MMM LGM-PI difference shows a weak poleward jet shift.

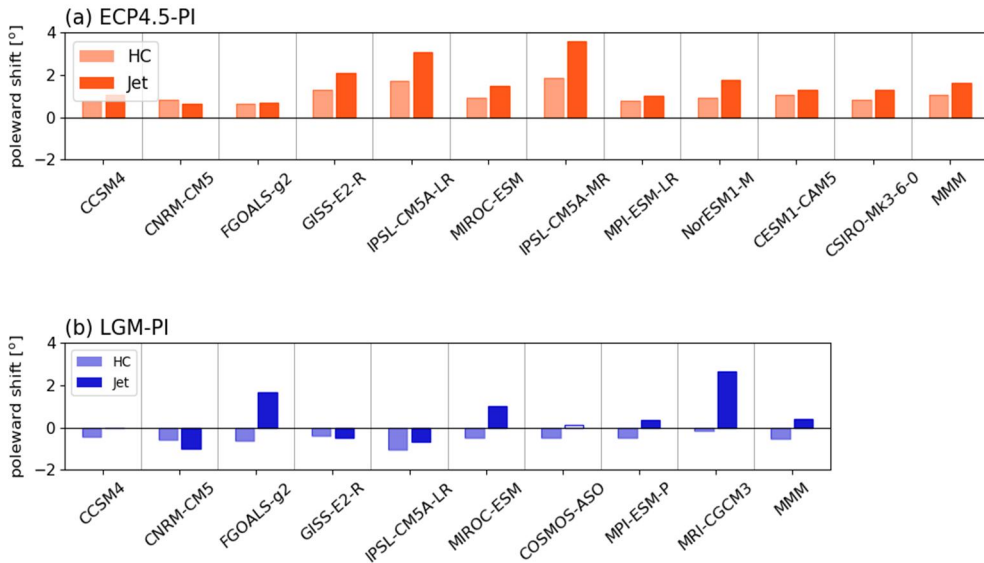


Figure 3.2. The annual-mean HC edge and jet latitude changes in (a) ECP4.5 and (b) LGM simulations compared to PI simulation. The statistically significant difference at the 95% confidence level is indicated

with a filled bar. Note that a positive value represents a poleward HC shift or a poleward jet shift in the SH.

The above result suggests a different HC-jet change in the ECP4.5 scenario and in the LGM scenario. All models show a poleward shift of both the HC edge and jet latitude in the ECP4.5 scenario, confirming a coherent poleward shift of the SH zonal-mean circulation in a warm climate. No such relationship, however, is observed in a colder climate. In fact, six out of the nine models (i.e., the CCSM4, FGOALS-g2, MIROC-ESM, COSMOS-ASO, MPI-ESM-P, and MRI-CGCM3) show that the HC edge and jet latitude changes from the PI to LGM scenarios in the opposite direction (Fig. 3.2b).

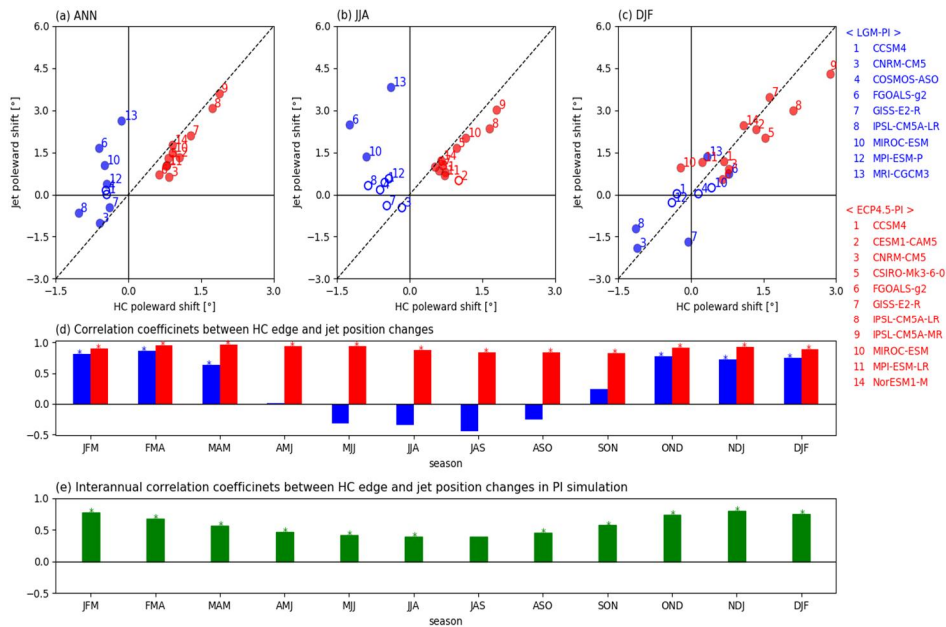


Figure 3.3. Relationship between the HC edge and jet latitude changes in the LGM-PI (blue) and ECP4.5-PI (red) differences for (a) the annual mean, (b) austral winter, and (c) austral summer. The models that show statistically significant jet latitude changes are denoted with filled circles, while those with an insignificant change are denoted with an open circle. (d) Correlation coefficients between the HC edge and jet latitude changes in the LGM-PI (blue) and the ECP4.5-PI (red) differences for all seasons with significant correlation coefficients denoted with asterisks. (e) Interannual correlation between the HC edge and jet latitude in the PI simulations. The correlation coefficient derived from each model is simply averaged. The asterisk indicates that more than 80% of the models have a statistically significant correlation at the 95% confidence level.

The opposing HC-jet change from the LGM to PI scenarios (Fig. 3.2b) is further illustrated in Fig. 3.3a. The HC-jet relationship is quasi-linear from the PI to ECP4.5 scenarios (red), with a regression close to a 1:2 ratio as in the literature (e.g., Gerber and Son 2014). Such a relationship, however, does not appear in transitioning to a cold climate (blue). Unlike the ECP4.5-PI differences, which are all located in the top-right corner of the figure, the LGM-PI differences are spread from the top-left to bottom-left corners of the figure.

A breakdown in the HC-jet relationship in the LGM scenario is mainly observed in austral winter (June-July-August; JJA) (Fig. 3.3b). In austral summer (December-January-February; DJF), the HC-jet relationship is quasi-linear (Fig. 3.3c) regardless of a warm or cold climate. While the HC edge and jet latitude changes are linearly related

in most seasons under the ECP4.5 condition (red bars in Fig. 3.3d), their relationship switches the sign from a positive to a negative value in austral winter with a maximum negative correlation in July-August-September. This result clearly indicates that the non-systematic changes in the HC edge and jet latitude from the LGM to PI scenarios are seasonally dependent, occurring only in austral winter.

3.2 HC-jet Relationship from cold to warm climates

3.2.1 Long-term change *versus* interannual variability

One could relate a non-systematic long-term change, shown in Figs. 3.3a, b, with an interannual co-variability of the HC edge and jet latitude. It is well documented that the SH HC edge and jet latitude co-vary on the interannual timescale, and their correlation is stronger and more statistically significant in DJF than in JJA (Kang and Polvani, 2011; Waugh et al. 2018).

This is also true in all simulations analyzed in this study. The interannual HC-jet co-variability is generally weak in JJA (Fig. 3.3e) as the annual-mean circulation change is mainly explained by JJA change (Figs. 3.3a-c). Most models indeed show the HC-jet interannual correlation coefficients greater than 0.6 in DJF and rather small correlation coefficients of 0.4 in JJA in the PI scenario (Fig. 3.3e). A strong positive

interannual correlation in DJF is consistent with a coherent HC edge and jet latitude changes from the LGM to PI, then to ECP4.5 scenarios in DJF (Fig. 3.3d). However, the interannual co-variability in JJA, which is weak but still positive, does not match the long-term HC-jet changes shown in Fig. 3.3d.

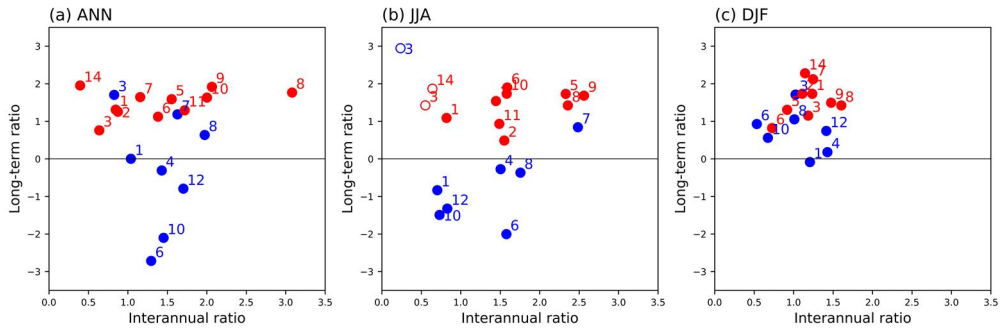


Figure 3.4. Comparison between the interannual ratio and long-term ratio of HC edge to jet latitude in LGM (blue) and ECP4.5 (red) simulations for (a) the annual mean, (b) austral winter, and (c) austral summer. The long-term ratio is considered as the difference of the LGM (blue) or ECP4.5 (red) simulation from the PI simulation. The interannual ratio with a statistically significant correlation coefficient at the 95% confidence level between the HC edge and the jet latitude is denoted with filled circles.

The possible relationship between the interannual co-variability and long-term change of the HC edge and jet latitude is quantified by evaluating the interannual co-variability ratio and long-term change ratio in Fig. 3.4. Here the interannual ratio is defined by the linear regression coefficient of the jet latitude to the HC edge across all years in the LGM or ECP4.5 simulation. The long-term ratio is defined by the jet

latitude change divided by the HC edge change from the PI to LGM scenarios or from the PI to ECP4.5 scenarios. This is essentially the slope of each dot from the zero in Figs. 3.3a-c. If the long-term ratio is greater than one, the jet latitude change is larger than the HC edge change. If negative, the long-term change of the jet latitude is opposite in sign to that of the HC edge (e.g., several blue dots below zero line in Figs. 3.4a and b). Since this ratio cannot be defined well when the HC edge change is close to zero or the shift of jet latitude is much greater than the HC edge change, those models are excluded (e.g., MRI-CGCM3 in LGM, GISS-E2-R in LGM DJF, and MIROC-ESM and MPI-ESM-LR in ECP4.5 DJF).

Figure 3.4b shows that the interannual ratios in LGM substantially vary from 0.2 to 2.5. This result, which indicates that the HC-jet co-variability is not robust in austral winter, is partly caused by the fact that the thermally-driven HC becomes stronger and is only weakly influenced by midlatitude eddies in this season (e.g., Bordoni and Schneider 2010). However, all simulations still show positive interannual ratios in the LGM scenario. This differs from the long-term ratios that are even negative in some LGM models (blue dots in Fig. 3.4b). This result clearly suggests that the long-term trend and interannual variability are not necessarily controlled by the same dynamic processes.

The HC edge and jet latitude co-vary remarkably well in DJF (Fig. 3.4c). The interannual ratio is on average 1.1 for the LGM, 1.3 for the PI, and 1.2 for the ECP4.5 scenarios, indicating that the jet latitude change is slightly larger than the HC edge change. This value is similar to the one in the reanalysis (about 1.1). The interannual ratios, which widely spread from near 0.5 to 1.5, are partly related to the long-term ratios. This is especially true in the ECP4.5 scenario. The interannual ratios in the ECP4.5 scenario are related to the long-term ratios in the ECP4.5-PI differences (red dots in Fig. 3.4c). This may imply that both long-term change and interannual co-variability are mediated by the same dynamical process. Such a linear relationship, however, does not appear in the LGM-PI differences (blue dots in Fig. 3.4c). This result again suggests that the long-term circulation changes cannot be simply explained by internal dynamics (e.g., Li et al. 2015).

3.2.2 Model-mean bias in LGM

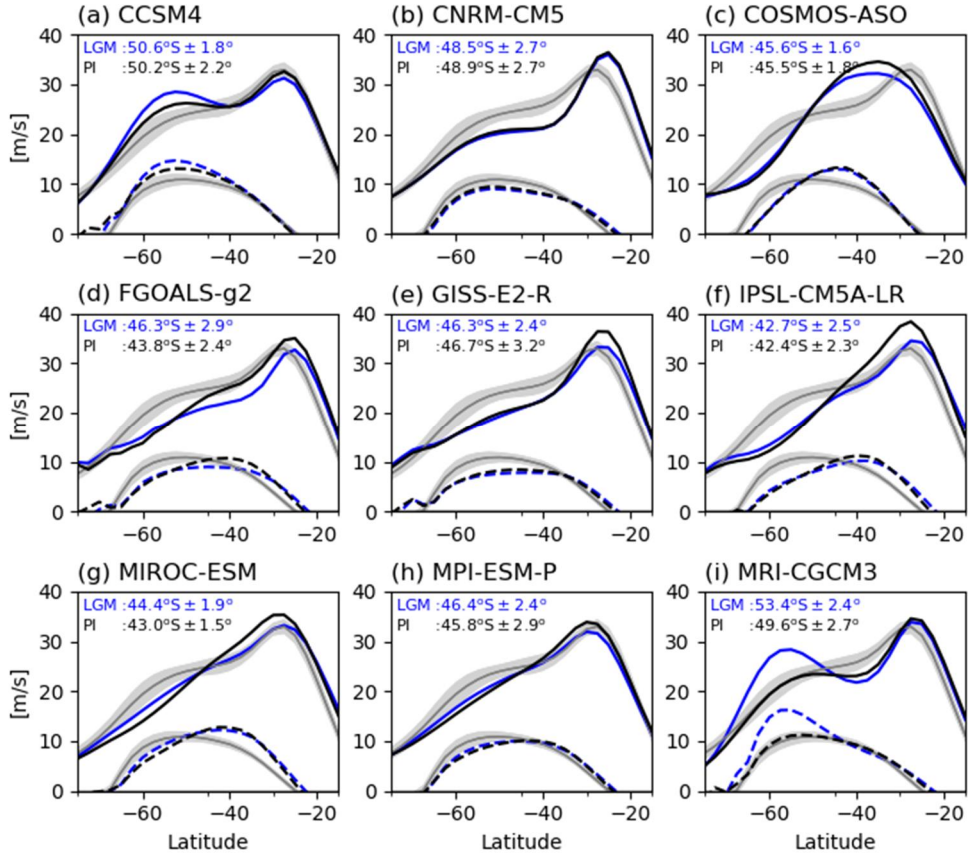


Figure 3.5. The austral winter (JJA) zonal-mean zonal wind at 300 hPa (solid lines) and 850 hPa (dashed lines) in the LGM (blue) and PI (black) simulations. The reference wind profile from JRA-55 is also shown in gray with one standard deviation on the interannual timescale. The position of the eddy-driven jet and its one standard deviation are indicated in the top-left corner of each panel.

The opposing HC-jet change in the LGM-PI difference may be associated with model mean biases and/or thermal forcings which are

different from the ECP4.5-PI difference. Since the incoherence is found only in JJA, all analyses below are focused on JJA circulation changes.

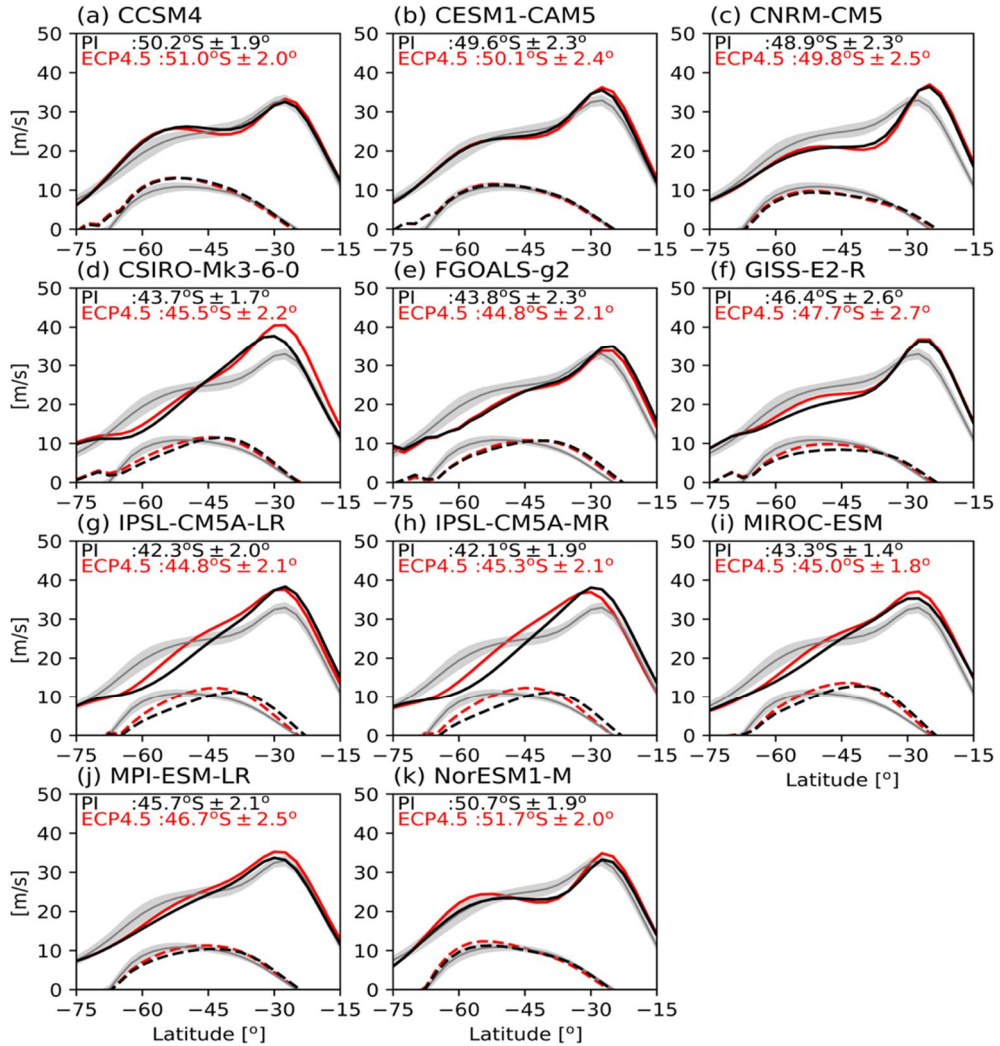


Figure 3.6. Same as Figure 3.5 but for the ECP4.5 (red) and PI (black) simulations.

The jet response to external forcing is influenced by the background flow. For instance, Son and Lee (2005) showed that a poleward jet shift in response to the polar cooling becomes stronger

when tropical driving is relatively weak. This could result in the eddy-driven jet becoming separated from the subtropical jet. Such jet separation is observed in the MRI-CGCM3 LGM simulation (Fig. 3.5i). The eddy-driven jet (maximum wind at 850 hPa) is separated from the subtropical jet (maximum wind at 300 hPa). This jet structure change may partly explain a significant poleward jet shift from the PI to LGM scenarios in this model (Figs. 3.3b and 3.5i).

A significant poleward jet shift from the PI to LGM scenarios in FGOALS-g2 could also be caused by the latitudinal jet structure. As shown in Fig. 3.5d, this model shows an almost flat zonal wind profile at 850 hPa in the LGM condition. A similar flattening is also observed in GISS-E2-R. Such flattening of the midlatitude jet, which is not observed in the ECP4.5 scenario (see Fig. 3.6), could lead to a large jet latitude change with a slight wind change.

It should be stated that the majority of models fail to reproduce the climatological jet latitude in the observations. In JJA, the jet in the Japanese 55-year reanalysis (JRA-55, Kobayashi et al. 2015) is located at 49°S. Among the nine models examined in Fig. 3.5, only three models, CCSM4, CNRM-CM5, and MRI-CGCM3, reproduce such a high-latitude jet under the PI condition (compare the black and gray lines in Fig. 3.5). All other models show the jet biased to lower latitudes. Three models (i.e.,

FGOALS-G2, IPSL-CM5A-LR, and MIROC-ESM) display the jet at even 42°S or 43°S in PI condition, about 7° equatorward from the jet in the modern reanalysis data. This bias could affect the jet latitude response to the Antarctic cooling in the LGM condition. Previous studies have indicated that the models with a lower-latitude jet tend to have a larger jet latitude response to climate change in austral winter (Simpson and Polvani 2016). This may suggest that a significant poleward shift in the austral winter jet in FGOALS-g2 (Fig. 3.5d) and MIROC-ESM (Fig. 3.5g) is partly due to the model mean bias. However, it is found that the jet latitude change is not directly correlated with the climatological jet position in each model (Fig. 3.7).

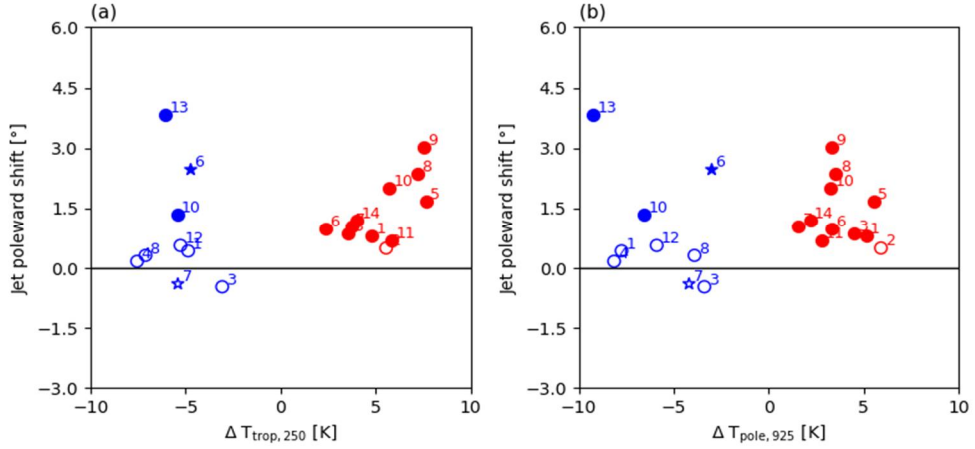


Figure 3.7. The relationship of jet latitude change to (a) $\Delta T_{\text{trop}250}$ and (b) $\Delta T_{\text{pole}925}$ in the LGM-PI (blue) and ECP4.5-PI (red) differences in austral winter (JJA). The stars denote the models with a flattened eddy-driven jet in the LGM simulations. The filled circles indicate the models which have statistically significant jet latitude changes as in Fig. 3.3.

3.2.3. Update to state-of-the-art models

We further extend the above analysis using state-of-the-art climate models. The three PMIP phase 4 (Kageyama et al. 2018) models which have both LGM and PI scenarios, i.e., AWI-ESM-1-1-LR, MIROC-ES2L, and MPI-ESM1-2-LR, are investigated (Table 2.3). The results from PMIP4 LGM models are summarized in Fig. 3.8. Although less robust in the annual mean (Fig. 3.8a), the three models exhibit the equatorward shift of the HC edge and the poleward shift of the jet latitude in the austral winter in the SH (Fig. 3.8b). These opposing HC–jet changes in PMIP4 models Comparison of Figs. 3.8a and 3.8b reveal that the PMIP3 and PMIP4 models reproduce similar results of HC-edge and jet-latitude

changes in the austral winter LGM condition compared to the PI condition.

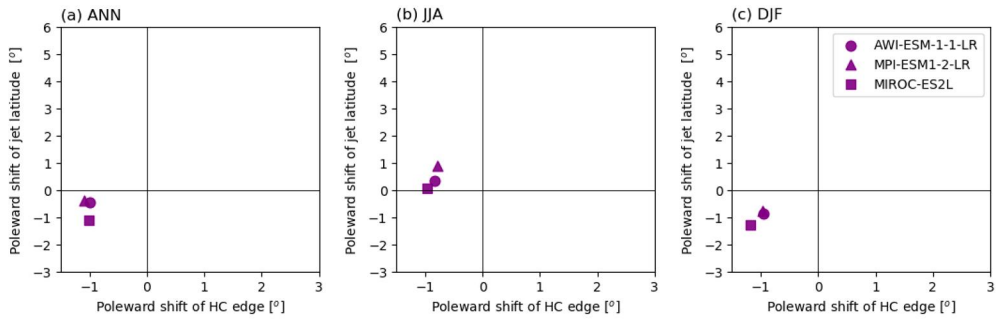


Figure 3.8. Same as Fig. 3.3 (a-c) but for PMIP4 models.

3.3 Role of tropical and polar temperature in the opposing HC–jet change

It is well documented that both the HC edge and jet latitude are controlled by eddy momentum fluxes (Walker and Schneider 2006; Caballero 2007; Lu et al. 2008; Son et al. 2018b). Since eddy fluxes are sensitive to thermal forcings, the zonal-mean circulation changes have often been related to meridional and/or vertical temperature gradient changes. Under global warming, the tropical upper-tropospheric warming acts to increase static stability in the subtropics and an equator-to-pole temperature gradient in the upper troposphere (e.g., Fig. 3.1a). This tends to drive an HC expansion and a poleward jet shift in both

idealized and comprehensive general circulation model simulations (e.g., Butler et al. 2010; Gerber and Son 2014). In contrast, the polar amplification could cancel such circulation changes by reducing the equator-to-pole temperature gradient near the surface (e.g., Barnes and Polvani 2015).

Based on Figs. 3.1a and d, the LGM and ECP4.5 thermal forcings are quantified by the tropical temperature changes at 250 hPa averaged over 0° – 30° S ($\Delta T_{\text{trop},250}$) and the Antarctic near-surface temperature changes at 925 hPa averaged over 55° – 75° S ($\Delta T_{\text{pole},925}$), with respect to the PI condition. These temperature indices are first compared to the latitudinal jet shifts. It turns out that the jet latitude change is not directly related to each index (Fig. 3.9) or their linear combination (not shown).

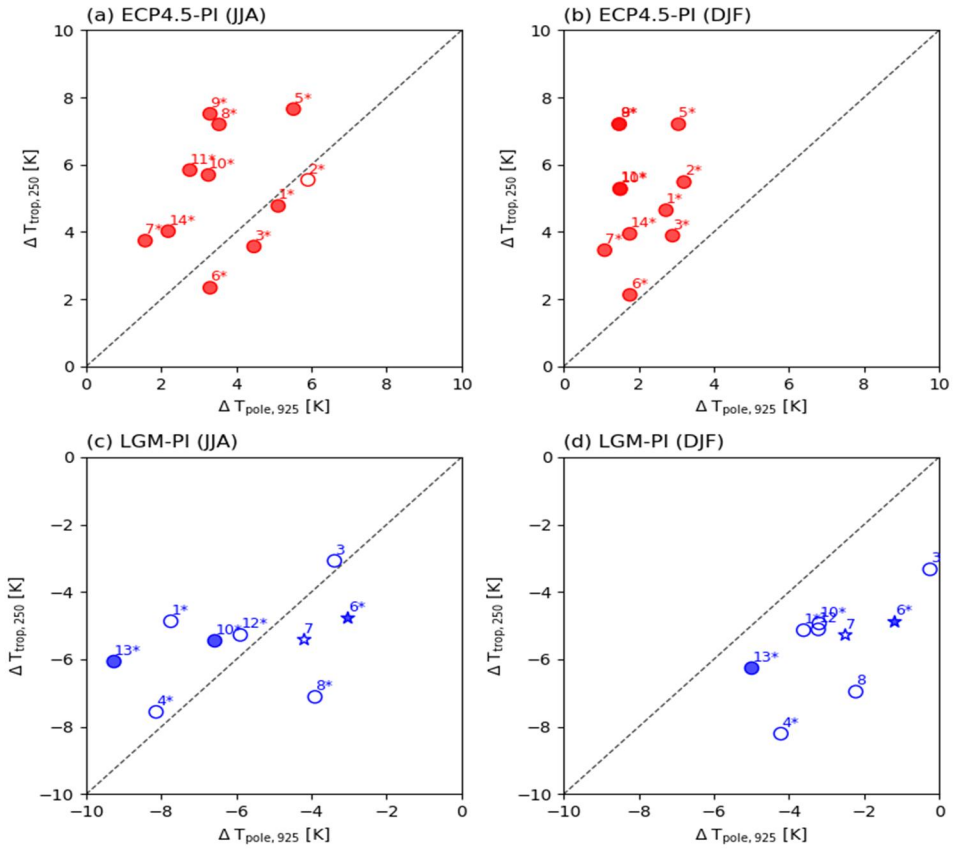


Figure 3.9. Polar temperature changes at 925 hPa ($\Delta T_{\text{pole},925}$) and tropical temperature changes at 250 hPa ($\Delta T_{\text{trop},250}$) in austral winter (left) and summer (right) for the ECP4.5-PI differences (top) and the LGM-PI differences (bottom). The model that shows a statistically significant jet latitude change is denoted with a filled circle, while that with an insignificant change is denoted with an open circle as in Fig. 3.3 and Fig. 3.7. The asterisk indicates the model showing a poleward jet shift.

The relative importance of tropical and polar temperature changes in the zonal-mean circulation change is qualitatively evaluated in Fig. 3.9 for both the LGM and ECP4.5 simulations. It is apparent from Figs. 3.9a and b that most models have comparable or greater tropical

warming than the Antarctic warming in the ECP4.5 scenario (values around or above the diagonal axis). This result suggests that a coherent poleward shift in the HC edge and jet latitude from the PI to ECP4.5 scenarios is likely related to the greater impact of the tropical upper-tropospheric warming than that of the high-latitude near-surface warming. This result, implying upper-tropospheric driving rather than lower-tropospheric driving, is consistent with previous findings (e.g., Lu et al. 2008; Gerber and Son 2014; Grise and Polvani 2016).

The upper-tropospheric driving, however, is unlikely to hold in the LGM scenario (Figs. 3.9c and d). As discussed in Rojas (2013) and Chavaillaz et al. (2013), the Antarctic temperature response ($\Delta T_{\text{Pole},925}$) has a larger intermodal spread in the LGM scenario than the ECP4.5 scenario. In DJF, the tropical upper-tropospheric cooling in the LGM scenario is still stronger than the Antarctic cooling (values below the diagonal axis in Fig. 3.9d), as in the ECP4.5 scenario. However, this is not the case in LGM JJA. Only three models (FGOALS-g2, GISS-E2-R, and IPSL-CM5A-LR) show a stronger tropical cooling than the polar cooling (Fig. 3.9c), while others show a comparable or weaker tropical cooling than the polar cooling. Among them, five models (CCSM4, COSMOS-ASO, MIRO-ESM, MPI-ESM-P, and MRI-CGCM3) show the near-surface polar cooling greater than -6 K. Such a large polar temperature change does

not appear in the ECP4.5 scenario. None of 11 ECP4.5 simulations show the polar warming greater than 6 K (Figs. 3.9a and b).

This difference, i.e., strong JJA polar cooling in the LGM simulation, may explain the opposing HC-jet change in the LGM condition. Although the JJA jet changes are not linearly related to the near-surface polar temperature changes, all the models which have a stronger polar cooling than the tropical cooling show a poleward jet shift from the PI to LGM scenarios. This, however, cannot be generalized. There are two exceptional models that show a poleward jet shift under a rather weaker polar cooling condition. These models have a polar cooling weaker than the tropical cooling in JJA. Note that although FGOALS-g2 (6 in Fig. 3.9c) exhibits a large jet latitude change of approximately 2.5° , this change may not be physically meaningful as the jet is not well defined in this model (see section 2.1).

3.4 Global cooling-like experiments: dynamic-core GCM

3.4.1 Motivation

Although the opposing HC-jet change is tested with idealized model experiments, its detailed mechanism is still unclear. In particular, the role of eddies remains to be determined in the opposing HC-jet changes. The jet changes in response to temperature changes likely occur

through the changes in eddy activities, such as growth, propagation, and dissipation of baroclinic eddies (Son and Lee 2005; Chen and Held 2007; Lu et al. 2010; Kidston et al. 2010; 2011; Lorenz 2014). However, previous studies have mostly focused on the circulation changes under global warming or global warming-like climate states. No studies have examined eddy activity changes in the LGM-like climate states.

The goal of this section is to examine the mechanism of the opposing HC-jet changes in the LGM-like climate and the role of baroclinic eddies in such a change. Instead of using a coupled model, a simple GCM is utilized to address the dynamical mechanism. Specifically, a dry dynamical-core GCM is integrated by varying thermal forcings in the tropical upper troposphere and on the polar surface as in Son and Lee (2005). Note that similar experiments were already performed in KS20. In this study, their experiments are extended to much wider climate states. Moreover, the same parameter sweep experiments are also conducted for the global warming-like climate states to identify the possibility of the opposing HC-jet change in a future climate.

Section 3.4 is organized as follows. The model and the imposed thermal forcings are introduced in sections 2.2.1 and 2.2.2. The zonal-mean atmospheric changes in the control simulation from the model are found in section 3.4.2. Section 3.4.3 presents the HC and jet responses to

the LGM-like cooling forcings. In section 3.4.4, we provide the experiments with varying amplitudes of tropical and polar thermal perturbations.

3.4.2 Control experiment

The zonal-mean state in CTRL is illustrated in Fig. 3.10 in contours. From top to bottom, temperature, mass stream function, and zonal wind are presented. The zero-crossing latitude of Ψ_{500} , i.e., the HC edge, locates at 27.0°S (second row), which is comparable to the one in the reanalysis. The midlatitude zonal wind (third row) is westerly throughout the troposphere. Its maximum intensity of approximately 36.2 m s^{-1} appears at 250 hPa and 42°S . In the lower troposphere, the zonal wind switches its direction with latitudes, from easterly to westerly around the HC edge and back to easterly at the poleward boundary of the Ferrell cell ($\sim 60^{\circ}\text{S}$). The maximum zonal wind at 850 hPa appears at about $\sim 40^{\circ}\text{S}$. These features of zonal-mean circulations are well reported in the literature (e.g., Son and Lee 2005; Butler et al. 2010).

3.4.3 Reference Cooling experiment

We start by examining zonal-mean temperature and circulation responses in the three cooling experiments: i.e., tropical cooling-only experiment with $(q_{\text{trop}}, q_{\text{pole}}) = (-0.3, 0.0)$ K day⁻¹, polar cooling-only experiment with $(q_{\text{trop}}, q_{\text{pole}}) = (0.0, -1.2)$ K day⁻¹, and multiple cooling experiment with $(q_{\text{trop}}, q_{\text{pole}}) = (-0.3, -1.2)$ K day⁻¹. The responses are quantified by the differences from CTRL (cooling experiments – CTRL; shading in Fig. 3.10). These three experiments are selected to examine the relative role of tropical and polar cooling on the zonal-mean circulation changes under the LGM-like climate states. Although not shown, the temperature difference shown in Fig. 3.10c resembles that of LGM minus PI climate states obtained from the PMIP3 multi-model mean (KS20).

The tropical cooling experiment exhibits a maximum cooling of 4 K in the tropical upper troposphere centered at 250 hPa that extends to ~40°S (blue shading in Fig. 3.10a). In response to the weakened static stability in the subtropics, the mass stream function becomes weak at the HC edge (red shading in Fig. 3.10d) and strong in the deep tropics, indicating a contraction and strengthening of the HC. The westerly jet shows distinct dipolar changes. The jet is weakened on its poleward flank near 50 ° S (blue shading in Fig. 3.10g) but strengthened on the

equatorward flank centered at 30°S. This zonal wind change indicates an equatorward shift of the jet latitude. In summary, both the HC edge and the jet latitude shift equatorward in response to the tropical cooling. Here it is noteworthy that zonal wind is also strengthened in the equatorial upper troposphere (see red shading at 200 hPa from 15°S to the equator). This anomalous westerly in the deep tropics is consistent with the acceleration of the subtropical jet by the strengthened HC (blue shading in Fig. 3.10d). As shown later, the same zonal wind change is observed in the two-dimensional model simulation in which eddies are not permitted with the same tropical cooling.

The middle column of Fig. 3.10 shows the zonal-mean circulation response to the polar cooling. A polar cooling of ~ 11 K is found, which extends up to $\sim 50^\circ\text{S}$ in latitude and 700 hPa in the vertical (blue shading in Fig. 3.10b). No significant temperature change is observed in the tropics. The mean meridional circulation changes are characterized by an anomalous anticlockwise circulation near the HC edge (blue shading in Fig. 3.10e), indicating the poleward shift of the HC edge. Similarly, the zonal wind change shows a strengthened jet on the poleward flank of the jet (red shading in Fig. 3.10h). Such circulation changes represent a systematic poleward shift of the HC edge and the jet latitude in response to the polar cooling. These circulation changes are exactly the opposite

of the tropical-cooling-induced circulation changes, although their magnitudes are relatively weak (Figs. 3.10e and 3.10h).

The competing roles between tropical cooling versus polar cooling are similarly found in the global warming scenario with a switched sign (e.g., Butler et al. 2010; Yuval and Kaspi 2016). Their relative importance is tested by conducting the model experiment with both tropical and polar cooling (Fig. 3.10c). Figures 3.10f and 3.10i portray that both the HC edge and jet latitude shift equatorward, indicating the dominant impact of tropical cooling in this multi-cooling experiment. The linear summation of atmosphere responses from tropical-cooling and polar-cooling experiments well coincides with the response from the multi-cooling experiments (not shown). This additivity suggests that the zonal-mean circulation change in the multi-cooling experiment can be to a large extent understood by considering tropically-induced and polar-induced circulation changes.

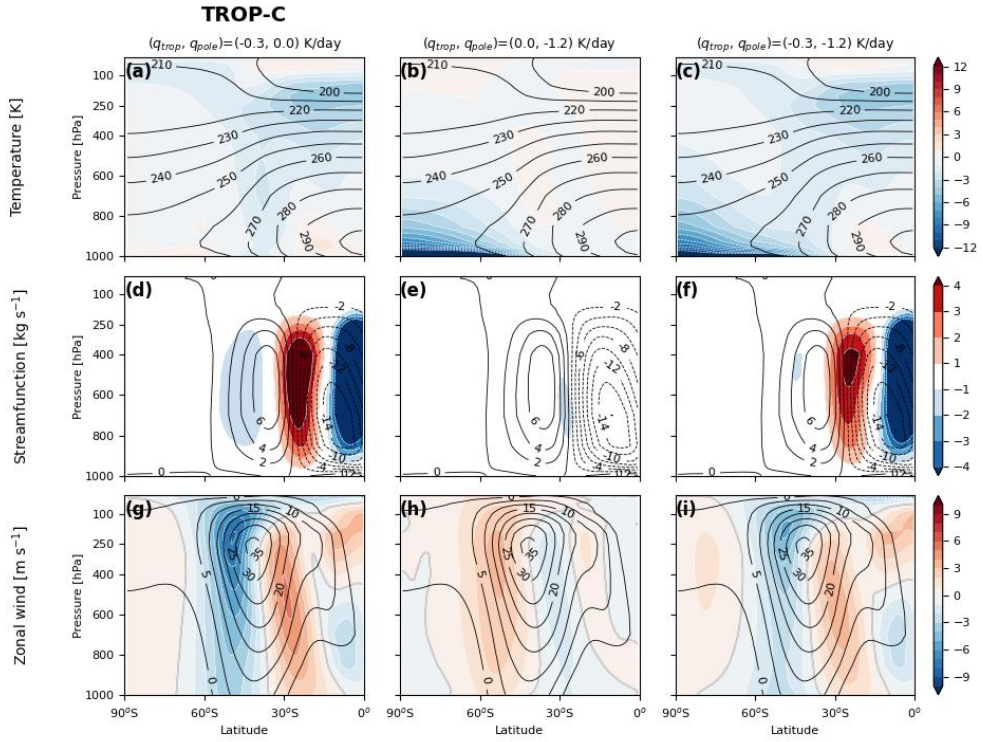


Figure 3.10. (top) Climatological zonal-mean temperature (unit: K), (middle) mass stream function (unit: $10^{10} \text{ kg s}^{-1}$), and (bottom) zonal wind (unit: m s^{-1}) in CTRL (contours) and their responses to the thermal forcings (shading) when $(q_{\text{trop}}, q_{\text{pole}}) = (-0.3, 0.0)$, $(0.0, -1.2)$, and $(-0.3, -1.2) \text{ K day}^{-1}$ from left to right columns. The contours in (a–c) are from 200 K to 310 K with an interval of 10 K in (a–c), from $-20 \times 10^{10} \text{ kg s}^{-1}$ to $20 \times 10^{10} \text{ kg s}^{-1}$ with an interval of $2 \times 10^{10} \text{ kg s}^{-1}$ in (d–f), and from 0 to 40 m s^{-1} with an interval of 5 m s^{-1} in (g–i). In the bottom row, zero lines of shading are indicated in thick gray lines. The experiment denoted with TROP-C is further examined in Chapter 4.

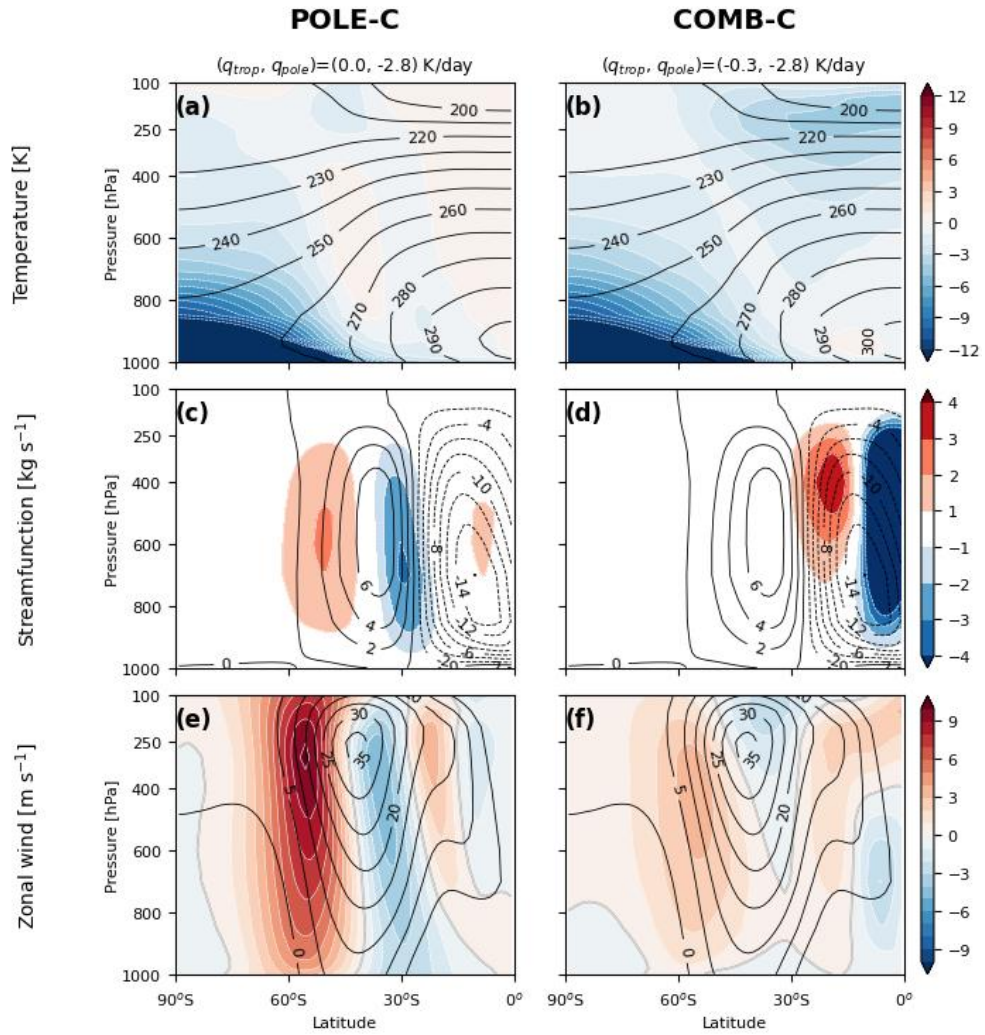


Figure 3.11. Same as Fig. 3.10 but for experiments with $(q_{\text{trop}}, q_{\text{pole}}) =$ (left) $(0.0, -2.8)$ and (right) $(-0.3, -2.8)$ K day⁻¹. The experiments denoted with POLE-C and COMB-C are further examined in Chapter 4. Figure formats are identical to those in Fig. 3. 10.

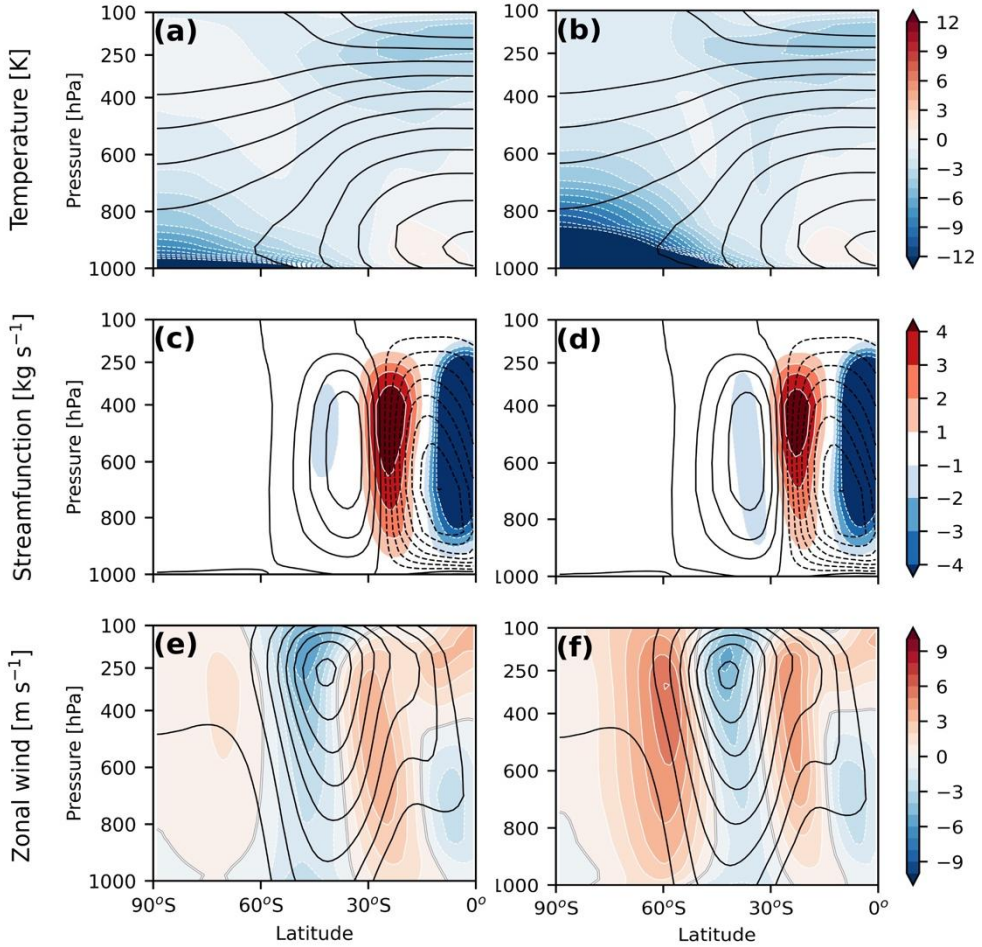


Figure 3.12. (left) Temperature, mean meridional circulation, zonal wind in the linear summation of experiments with $(q_{\text{trop}}, q_{\text{pole}}) = (-0.3, 0.0)$ K day^{-1} and $(q_{\text{trop}}, q_{\text{pole}}) = (0.0, -1.2)$ K day^{-1} , which are represented in the left two columns of Fig. 3.10. (right column) Same as (a, c, e) but for the linear summation of experiments with $(q_{\text{trop}}, q_{\text{pole}}) = (-0.3, 0.0)$ K day^{-1} and $(q_{\text{trop}}, q_{\text{pole}}) = (0.0, -2.8)$ K day^{-1} with the former same as the left column of Fig. 3.10 and the latter shown in the right column of Fig. 3.11. Figure formats are identical to those in Fig. 3. 10.

Figure 3.11 illustrates the circulation responses to the same tropical cooling but with the enhanced polar cooling compared to Fig. 3.10. The enhanced polar-only cooling produces the poleward shifts of

the HC edge and jet latitude (Figs. 3.11a,c,e), which are similar but stronger than the effect found in the moderate polar-only cooling experiment (Figs. 3.10b,e,h). When combining tropical and enhanced polar cooling (right column of Fig. 3.11), the temperature response resembles that of the LGM minus PI climate states in PMIP3 (compare Fig. 3.11b to Fig. 3.1d). Overall changes in the combined experiment (right columns of Fig. 3.11) are again qualitatively similar to those in the linear summation of single-forcing experiments (right column of Fig. 3.12), although the magnitudes of circulation responses are slightly weaker. It is of note that the jet-latitude change is still dominated by polar cooling in this combined cooling experiment, but the HC-edge change is more strongly influenced by tropical cooling. This opposing effect results in a *poleward* shift of the jet latitude by 1.2° and an *equatorward* shift of the HC edge by 1.6° with respect to the CTRL (Figs. 3.11d and f). This opposing HC–jet shift is qualitatively similar to the circulation changes found in the selected PMIP3 simulations as discussed in KS20.

A comparison of the rightmost columns of Fig. 3.10 and Fig. 3.11 reveals that polar amplification plays a critical role in the opposing HC–jet shift under the LGM-like climate state. The HC edge and jet latitude, which shift equatorward together when polar cooling is weak (rightmost in Fig. 3.10), shift in the opposite direction with an enhanced polar

cooling (right in Fig. 3.11; COMB-C). To quantitatively determine such opposing circulation changes to the cooling forcing, the cooling experiments are extended to a broader range of climate states in the following section.

3.4.4 Parameter sweep study

Figure 3.13a summarizes the parameter sweep experiments in terms of the HC-edge and jet-latitude changes from the CTRL as a function of q_{trop} and q_{pole} . The HC edge (upper number in each box in Fig. 3.13a) systematically shifts equatorward in response to decreasing q_{trop} and poleward in response to decreasing q_{pole} . It moves farther with an increase in the forcing amplitude and is more sensitive to q_{trop} than q_{pole} . Figure 3.13a also reveals that the HC edge always appears on the equatorward side of the CTRL HC when tropical cooling is non-zero ($q_{\text{trop}} \neq 0$). Such an equatorward shift of the HC edge is robustly found although it becomes weaker with increasing magnitude of q_{pole} (second to fourth columns). Similar to the HC-edge change, the jet latitude shifts equatorward with an increasing magnitude of q_{trop} and poleward with an increasing magnitude of q_{pole} (lower number in each box in Fig. 3.13a). However, the jet-latitude change exhibits both equatorward and poleward shifts in the combined experiments. A poleward jet shift occurs

in ~29% of combined-cooling experiments (6 out of 21 combined cooling experiments; dark blue in Fig. 3.13a), indicating that an opposing HC–jet shift, i.e., a poleward jet-latitude shift with an equatorward HC-edge shift, is not rare.

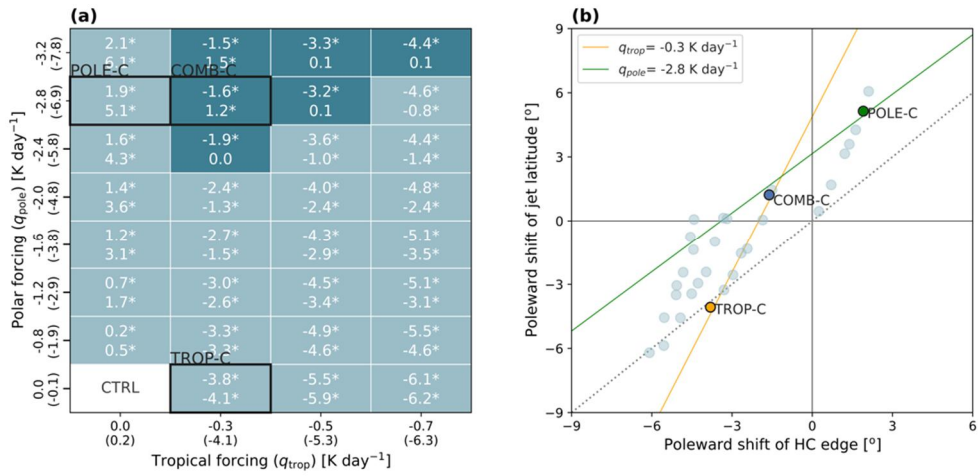


Figure 3.13. (a) The HC-edge and jet-latitude changes with respect to CTRL as a function of tropical forcing (q_{trop} in x-axis) and polar forcing (q_{pole} in the y-axis) in all cooling experiments. The upper and lower numbers in each box indicate the HC-edge and jet-latitude shifts from CTRL. The experiments with opposing circulation changes, i.e., an equatorward HC-edge shift but a poleward jet-latitude shift, are denoted in dark blue. The experiments, which are examined in detail in Chapter 4, are denoted with TROP-C, POLE-C, and COMB-C. (b) The relationship between the HC-edge and jet-latitude changes in experiments shown in (a). The experiment showing a significant jet-latitude shift at the 99% confidence level is denoted with a black edge, while the one with an insignificant shift is denoted with no edge.

The fact that the HC edge always shifts equatorward in all combined cooling experiments, but the jet latitude often shifts poleward

suggests a larger influence of the polar cooling on the jet-latitude change than on the HC-edge change. For instance, when $q_{trop} = -0.3 \text{ K day}^{-1}$ (second column in Fig. 3.13a), the jet shifts farther poleward by 5.3° from 0 K day^{-1} to -2.8 K day^{-1} of q_{pole} , eventually resulting in a poleward shift of the jet in the COMB-C with respect to the CTRL ($+1.2^\circ$), but the HC edge shifts poleward to a lesser extent by 2.2° and remains on the equatorward side of the CTRL HC edge (-1.6°). To further quantify the circulation changes in response to the thermal forcings, regression analyses are conducted as below:

$$\Delta\phi_{HC} = \alpha_{HC} q_{trop} + \beta_{HC} q_{pole} \quad (4),$$

$$\Delta\phi_{Jet} = \alpha_{Jet} q_{trop} + \beta_{Jet} q_{pole} \quad (5).$$

Here α and β are the latitudinal shifting rates of the circulation change ($\Delta\phi$) to the tropical and polar forcings, respectively. The subscripts, HC and Jet , denote the HC edge and the jet latitude, respectively. For instance, $\alpha_{HC} = -8.8^\circ / (\text{K day}^{-1})$ indicates an equatorward HC-edge shift ($\Delta\phi_{HC}$) of 8.8° when the tropical cooling increases by 1 K day^{-1} . Likewise, $\beta_{HC} = 0.7^\circ / (\text{K day}^{-1})$ indicates that the HC edge shifts poleward by 0.7° with an increase in polar cooling of 1 K day^{-1} .

Table 3.1. The shifting rates of the HC edge and jet latitudes to tropical/polar thermal forcings and the HC edge-to-jet latitude shifting

ratio (“HC-jet ratio”) for each forcing. The plus sign indicates a poleward shift.

Shifting rate	HC shifting rate	Jet shifting rate	HC-jet ratio
1 K day ⁻¹ cooling of tropics	-8.8 °K ⁻¹ day	-8.2 °K ⁻¹ day	0.93
1 K day ⁻¹ cooling of polar surface	0.7 °K ⁻¹ day	2.0 °K ⁻¹ day	2.81
1 K day ⁻¹ warming of tropics	10.2 °K ⁻¹ day	14.3 °K ⁻¹ day	1.40
1 K day ⁻¹ warming of polar surface	-1.0 °K ⁻¹ day	2.2 °K ⁻¹ day	2.10

Both the HC-edge and jet-latitude changes are quasi-linearly related to q_{trop} and q_{pole} changes, with determination coefficients (R^2) of 0.94 and 0.90, respectively. More importantly, the jet-latitude change is more sensitive to polar cooling than the HC-edge change. When tropical cooling increases, the HC edge and jet latitude shift almost equally (see Table 3.1). This is understood by the ratio of HC-edge-change to jet-latitude-change (hereafter “HC-jet change ratio”) to tropical cooling ($\alpha_{\text{jet}}/\alpha_{\text{HC}}$) which is close to unity (0.9). However, as polar cooling increases, the jet latitude shifts by 2.8° when the HC edge shifts by 1° ($\beta_{\text{jet}}/\beta_{\text{HC}}=2.8$). Note that the individual HC-jet ratio for a given thermal forcing could vary depending on the magnitudes of thermal forcings. While the HC-jet ratio is 2.4 for $q_{\text{trop}}=-0.3$ K day⁻¹, it is 3.5 for $q_{\text{trop}}=-0.7$ K day⁻¹. This can be attributed to other factors, such as

the circulation change by the mean flow or eddy activity, as discussed later.

It should be noted from Fig. 3.13b that the opposing HC-jet shifts are not outliers from the linearity. Figure 3.5b presents that the opposing circulation changes in COMB-C with $(q_{\text{trop}}, q_{\text{pole}}) = (-0.3, -2.8) \text{ K day}^{-1}$ (blue circle in Fig. 3.5b) appear at the intersection of the linear regression lines of $q_{\text{trop}} = -0.3 \text{ K day}^{-1}$ (orange line) and $q_{\text{trop}} = -2.8 \text{ K day}^{-1}$ (green line). Similar linearity is consistently found for other opposing shift cases, accentuating that the opposing HC-jet changes can be explained by the linear combination of the circulation responses to the two external forcings.

Chapter 4. Dynamical mechanisms for opposing HC –jet change

4.1 Plausible mechanism(s)

Based on the results from Chapter 3, we expect the independent change of the HC edge, which is less affected by the polar cooling. Instead, the jet is influenced by both tropics and poles (e.g., Barnes and Screen 2015). These result in a higher sensitivity of the jet latitude in response to polar cooling than the HC-edge's one. Here we propose the dynamical process for the opposing HC–jet changes in the LGM, based on the proposed mechanisms for the jet changes under global warming introduced in Chapter 1 (e.g., Chen et al. 2007; Riviere et al. 2011; Kidston et al. 2011; Lorenz 2014). The enhanced polar cooling under the LGM condition could induce an increase in baroclinicity in the lower troposphere, contributing to the poleward shift of the wave source. This can be related to the poleward shift of the jet. On the other hand, the tropical cooling in the upper troposphere likely causes the equatorward shift of the critical latitude on the tropical flank of the jet. This is largely influenced by the equatorward shift of the HC edge.

Here we propose a mechanism explaining the opposing HC–jet change: eddies act differently in the midlatitudes and tropics due to modified wave reflection by enhanced polar cooling/warming. The

mechanism for the opposing HC–jet change can be summarized by the following, especially under global cooling-like conditions.

- *Mechanism 1*: The poleward shift of the jet latitude could be originated from the enhancement of the lower-level baroclinicity on its poleward flank.
- *Mechanism 2*: The equatorward shift of the HC edge is more influenced by the tropical cooling-induced critical latitude changes in the tropics than the polar cooling-induced baroclinicity changes in the midlatitudes.
- *Mechanism 3*: The poleward shifted jet can be reinforced by the increased wave reflection by the enhanced zonal wind on the poleward flank of the jet.

These processes for the opposing HC–jet change are confirmed by the proposed mechanisms in previous studies. A group of studies is associated with the impact of polar forcing. For instance, in COMB-C (in Chapter 3), where polar cooling has a significant impact on the poleward side of the jet, the maximum latitude of the EHF shifts poleward, inducing the poleward-shifted wave source region. This means the increase of static stability in the midlatitudes, confirming the importance of static stability change in modulating the jet as in Lu et al. (2008). The

key role of the increased reflective profile in shifting the jet, allowing more waves to break in higher latitudes, is in great agreement with the suggestion from Lorenz (2014). There are mechanisms in agreement with the eddy activities' change in the opposing case. Tropical cooling tends to increase the westerlies on the tropical flank, pushing the critical latitude away from the jet core into lower latitudes, which has been used to argue that the critical latitude is a crucial factor shifting the jet poleward (Chen et al. 2007). The results from TROP-C show that the mechanism of Chen et al. (2007; 2008), described above, is acceptable with tropical cooling as well as tropical warming. As such, the results of this study suggest that the mechanisms introduced here are acceptable simultaneously, but the dominant one is determined by the effects of tropical and polar temperature changes.

To better understand the poleward jet-latitude shift in the LGM austral winter condition, this study explores the poleward shift of the jet under the LGM condition using an idealized GCM. In Chapter 3, we found that the poleward jet shift in the LGM is particularly found when the polar cooling is sufficiently larger than the tropical cooling. Here we address some of these issues as we investigate in more detail the mechanisms by carrying out the equilibrium and spinup ensemble experiments using the same dry-dynamical core. The equilibrium experiments for the three-

dimensional and axisymmetric simulations are indicated in sections 2.2 and 2.3, respectively.

The mechanisms for the opposing HC–jet change is proposed in section 4.1 and then examined in sections 4.2 and 4.3. Section 4.2 presents the changes in eddy momentum and heat fluxes in response to global cooling-like thermal forcings. Their axisymmetric responses are found in section 4.3. Section 4.4 presents the evolving circulation changes in response to thermal forcings.

4.2 Eddy activities in the global cooling experiments

Although the HC edge and the jet latitude are associated with the eddy momentum fluxes (EMF) as shown in Chapter 1, it does not guarantee the linear relationship of the HC-edge and jet-latitude changes in PMIP3 LGM simulations (Chapter 3). If EMF undergoes a structural change, the HC edge and jet latitude could change independently. In this study, the EMF at 250 hPa (EMF250) is utilized to associate the HC-edge and jet-latitude changes related to the EMF changes.

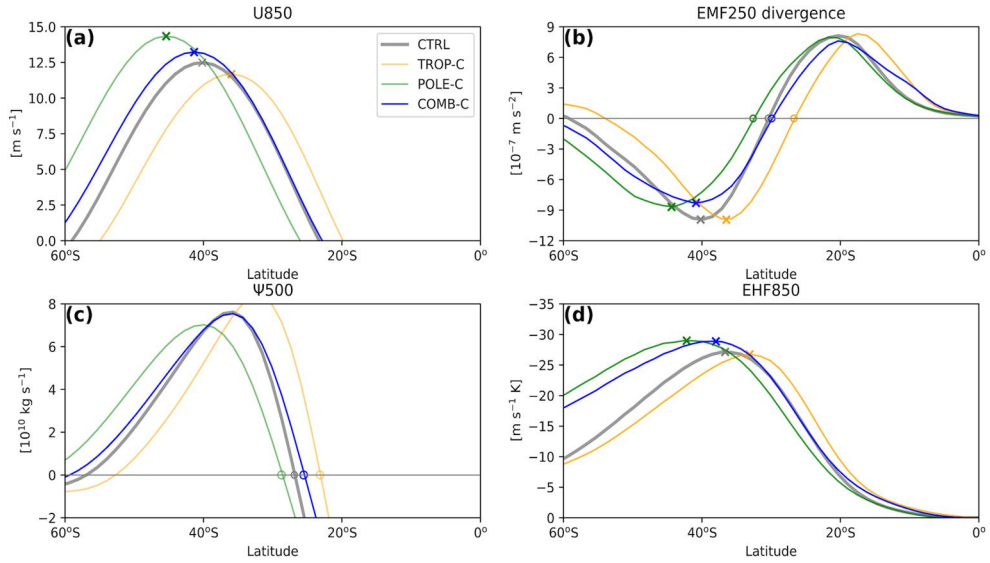


Figure 4.1. (a) The 850-hPa zonal wind (U850), (b) 250-hPa eddy momentum flux (EMF250) divergence, (c) 500-hPa mass stream function (Ψ 500), and (d) 850-hPa eddy heat flux (EHF850) in CTRL (gray), TROP-C (orange), POLE-C (green), and COMB-C (blue). The maximum latitudes of U850, EMF250 convergence, and EHF850 are denoted with “X” in (a), (b), and (d), respectively. The zero-crossing latitudes for EMF250 divergence and Ψ 500 are denoted with “O” in (b) and (c), respectively.

The latitudinal profiles of Ψ 500 and U850 are illustrated and compared with those of EMF250 divergence in Fig. 4.1. In the CTRL, the maximum EMF250 convergence appears at 40.2°S, which coincides well with the jet latitude (40.5°S; thick gray in Fig. 4.1a). It is surrounded by EMF250 divergence in the subtropics and high latitudes. The maximum divergence is found at 20.1 ° S, indicating wave breakings in the subtropics. The zero-crossing latitude of EMF250 divergence, which appears at 30.4°S, matches reasonably well with the HC edge (27.0°S, Fig.

4.1c). These results demonstrate that the QG dynamics is appropriate for explaining the HC edge and the jet latitude in a dynamical-core GCM (e.g., Son and Lee 2005; Butler et al. 2010; Yuval and Kaspi 2016).

The EMF250 divergences in the three reference experiments are illustrated in Fig. 4.1b. By comparing Fig. 4.1b with Figs. 4.1a and 4.1c, it is evident that the latitudinal changes of EMF250 divergence match well with those of the HC and jet. Both the latitude of maximum EMF250 convergence (“X” in Fig. 4.1b) and zero-crossing latitude (“O” in Fig. 4.1b) shift equatorward from CTRL (gray) to TROP-C (orange), similar to the jet-latitude and HC-edge changes. Oppositely, the poleward shifts of both the maximum and zero-crossing latitudes of EMF250 convergence are found in POLE-C (green) compared to the CTRL. The COMB-C (blue) shows the combined effect of TROP-C and POLE-C (blue). Unlike the systematic changes of EMF in TROP-C and POLE-C, the EMF250-convergence changes in COMB-C are rather subtle. Although weak, the EMF changes in COMB-C qualitatively reflect the opposing shifts of the circulations. While the zero-crossing latitude of EMF250 convergence is located slightly equatorward compared to that in CTRL (blue “O” in Fig. 4.1b), the latitude of the maximum EMF250 convergence still appears on the poleward side of CTRL (blue “X” in Fig. 4.1b).

The structural changes of EMF250 divergence can be largely explained by the baroclinicity changes which are often coupled to changes in the eddy heat flux at 850 hPa (EHF850). The EHF850 is used as a proxy of the baroclinic zone, i.e., stirring latitudes of baroclinic eddies, since the low-level EHF roughly represents the generation and vertical propagation of Rossby waves (Edmon et al. 1980). As shown in Fig. 3.2a, in TROP-C, tropical upper-tropospheric cooling acts to amplify baroclinic instability in the subtropics by reducing the static stability in the troposphere. This is consistent with an equatorward-shifted EHF850 compared to CTRL (orange in Fig. 4.1d), indicating an equatorward shift of the wave source region. The EMF250 also shifts equatorward (Fig. 4.1b), leading to an equatorward shift of both the HC edge and jet latitude in TROP-C compared to the CTRL (Figs. 4.1a, c). In contrast, when polar surface cooling is imposed in POLE-C, the baroclinic zone shifts poleward (green in Fig. 4.1d). The poleward-shifted EHF850 is followed by a poleward shift of EMF250 convergence (Fig. 4.1b).

In COMB-C, the enhanced meridional temperature gradient at high latitudes broadens the baroclinic zone poleward on its poleward flank as in POLE-C (blue in Fig. 4.1d). This matches the poleward shift of the maximum EMF250 convergence (Fig. 4.1b) and jet latitude (Fig. 4.1a). However, in the subtropics ($< 30^{\circ}\text{S}$), EHF850 in COMB-C does not change

significantly from the CTRL (compare blue and gray lines in Fig. 4.1d). This is likely due to the competition between the increase in high-latitude baroclinicity due to an increased meridional temperature gradient and the low-latitude baroclinicity increase due to a reduced static stability. Here it is important to note that the HC edge in COMB-C is located slightly equatorward of the CTRL HC edge although the maximum EHF850 appears on the poleward side of the CTRL EHF850 (Fig. 4.1d). This disagreement indicates that the equatorward shift of the HC edge in COMB-C cannot be simply explained by the polar cooling-induced changes in midlatitude baroclinic eddies, i.e., the EHF850 changes. Instead, additional factors, such as the advection of angular momentum by mean circulation and its modulation of subtropical eddy activity may also play an important role in determining the HC change. These additional factors may explain the different regression slopes shown in Fig. 3.13b (green and yellow lines).

It should be noted that the EHF850 change in COMB-C is largely related to the long waves induced by polar cooling (Fig. 4.2). Figure 4.2 clearly shows that the 850-hPa EHF is largely attributed to long waves with zonal wave number $k = 2$ to 5 in COMB-C (blue solid in Fig. 5.10). A similar increase of EHF at 850 hPa is found in POLE-C (green dashed) but

not in TROP-C (orange dotted). This indicates that EHF at 850 hPa by long waves is driven by polar cooling rather than tropical cooling.

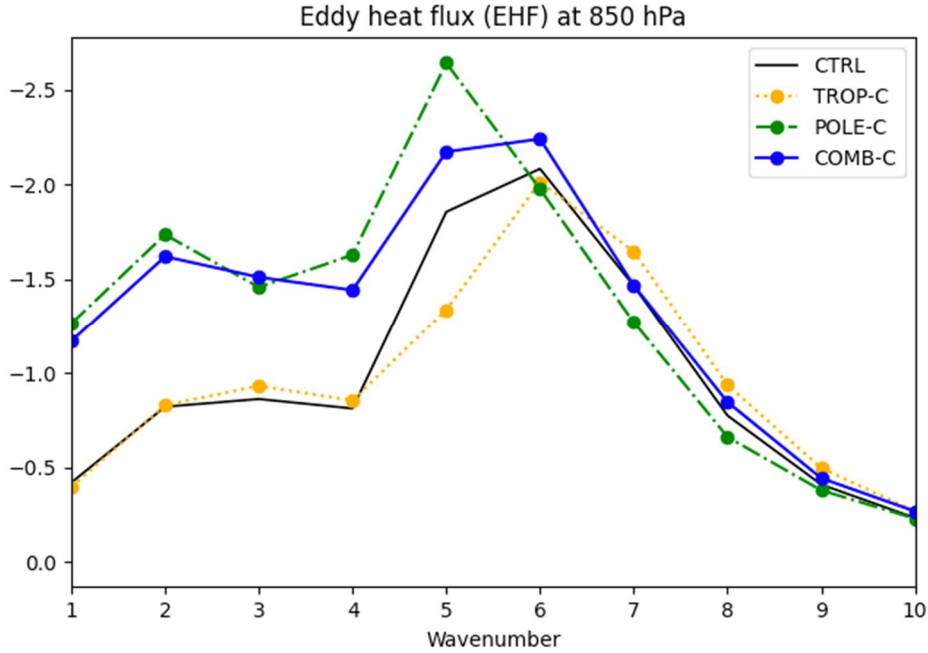


Figure 4. 2. Eddy heat flux at 850 hPa along with the zonal wavenumber (x-axis) in CTRL (gray), TROP-C (orange dotted), POLE-C (green dashed), COMB-C (blue solid) (unit: $\text{m s}^{-1} \text{ K}$).

To investigate the nature of the EMF250 changes, eddy cospectra are analyzed as a function of latitude (ϕ) and angular phase speed (c) (Fig. 4.3; Randel and Held 1991, Son and Lee 2005). In the CTRL (Fig. 4.3a), EMF250 convergence peaks at the phase speeds of 5–15 m s^{-1} at $\sim 40^\circ\text{S}$ where the jet is located. Its divergence has two peaks, i.e., one in the subtropics centered at $\sim 20^\circ\text{S}$ and the other at high latitudes centered at $\sim 69^\circ\text{S}$, with the former being much stronger than the latter (see also Fig. 4.1b). Both divergence peaks roughly appear along the curve of

background zonal wind (thick gray curve in Fig. 4.1a), where the waves meet their critical latitudes and are absorbed in the linear wave dynamics.

Figure 4.3 shows the eddy cospectra in TROP-C, POLE-C, and COMB-C. The equatorward shifts of both the convergence in the midlatitudes and the divergence in the subtropics in TROP-C, compared to CTRL (orange in Fig. 4.1b), are attributable to waves with nearly all phase speeds (shading in Fig. 4.3b). They correspond to the equatorward shift of the zonal wind (thick orange curve in Fig. 4.3b; see also shading in Fig. 3.10g). The changes of EMF250 divergence in POLE-C (shading in Fig. 4.3c) mostly oppose those in TROP-C (Fig. 4.3b), but its tropical response is weaker than that in TROP-C. This indicates a weak influence of the polar cooling on the tropical EMF divergence.

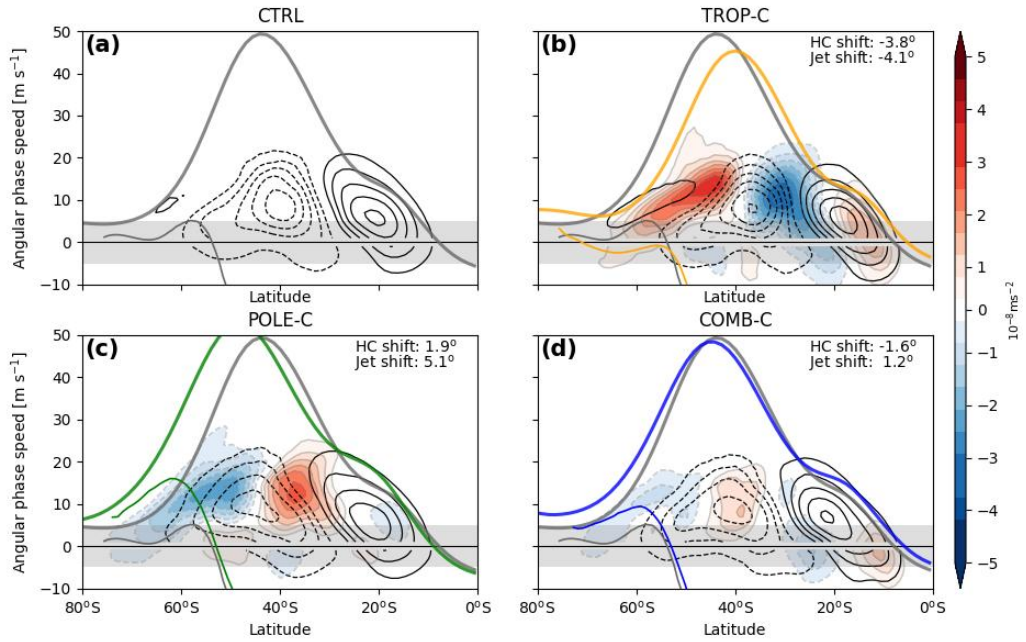


Figure 4.3. EMF250 divergence cospectra (10^{-8} m s^{-2} , contours) as a function of angular phase speed and latitude in (a) CTRL, (b) TROP-C, (c) POLE-C, and (d) COMB-C. (b–d) The differences in EMF divergence in each experiment from CTRL (e.g., TROP-C *minus* CTRL) are shaded, with anomalous divergence in blue and convergence in red. Contours are depicted from $-6 \times 10^{-8} \text{ m s}^{-1} \text{ day}^{-1}$ to $6 \times 10^{-8} \text{ m s}^{-1} \text{ day}^{-1}$ with intervals of $1 \times 10^{-8} \text{ m s}^{-1} \text{ day}^{-1}$, and the shading range is from $-5 \times 10^{-8} \text{ m s}^{-1} \text{ day}^{-1}$ to $5 \times 10^{-8} \text{ m s}^{-1} \text{ day}^{-1}$ with intervals of $0.4 \times 10^{-8} \text{ m s}^{-1} \text{ day}^{-1}$. Thick and thin curves indicate the critical latitude and the reflective latitude for zonal wavenumber 6, respectively, for CTRL (gray) and cooling experiments (colored). Gray shaded phase speed range of -5 to 5 m s^{-1} denotes a *slow* phase speed range.

The eddy cospectra in COMB-C (Fig. 4.3d) largely resemble the summation of those in TROP-C and POLE-C (Fig. 4.4). More importantly, the influences of tropical and polar cooling are well separated by latitudes in COMB-C. The latter is determined by slow waves, contrasting with the eddy flux changes in the midlatitudes which are controlled by

fast waves. This suggests that *fast* and *slow* waves have opposite roles in modulating the HC-jet shifts in COMB-C (Fig. 4.3d). The EMF250-divergence changes in midlatitudes are driven by *fast* waves with phase speeds of 5 to 15 m s⁻¹, creating a poleward shifted jet in the midlatitudes. The dominance of fast eddies in the jet movement has also been noted by Son and Lee (2005). In contrast, those in low latitudes ($\phi < 30^\circ\text{S}$) are dictated by *slow* waves with phase speeds of -5 to 5 m s⁻¹ (gray shaded area in Fig. 4.3d). They correspond to an equatorward HC-edge shift which is more strongly influenced by *slow* waves at low latitudes.

The phase speed-dependent EMF250 changes in the COMB-C occur partly due to the reflective- and critical-latitude changes in the context of linear wave dynamics. The reflective latitudes, which are computed following Harnik and Lindzen (2001), are depicted as thin curves from 80°–60°S in Fig. 4.3. They are displayed only for waves with zonal wavenumber 6 that mostly contributes to EMF250 change (e.g., Lutsko et al. 2017). Here, the reflective latitude for a given wave is determined as the latitude where the wave's phase speed line meets the reflective latitude curve (thin curve). Likewise, the critical latitude is defined as the latitude where the given phase speed line meets the background zonal wind (thick curve). For instance, in the CTRL, the waves with a phase speed $c=5$ m s⁻¹ (upper boundary of gray shading) do

not meet the reflective latitude curve (thin gray curve). It instead meets the zonal wind in both flanks, i.e., $\sim 78^\circ\text{S}$ and $\sim 10^\circ\text{S}$ in the CTRL (thick gray in Fig. 4.3a). This indicates that there is no reflective latitude but two critical latitudes for the wave with a phase speed of 5 m s^{-1} in the CTRL.

On the poleward flank of the jet, as the zonal wind increases, the range of phase speeds that encounter the reflective latitude increases from the CTRL to POLE-C or COMB-C (thin colored curves in Figs. 4.3c and 4.3d compared to thin gray in each figure). The increase in wave reflection impedes wave breaking at high latitudes, as represented by the reduced EMF250 divergence (solid contours at $\sim 60^\circ$ in Fig. 4.3a but no contours in Fig. 4.3c). As shown in Figs. 4.3c and 4.3d, *fast* waves with phase speeds from 5 to 15 m s^{-1} , which break at the critical latitude at high latitudes in the CTRL, reflect back to the jet core in POLE-C and COMB-C, inducing a poleward eddy momentum flux. Likewise, the decrease in wave reflection is observed in response to tropical cooling, as represented in the enhancement of EMF divergence at high latitudes (solid contours at $\sim 60^\circ$ in Fig. 4.3b).

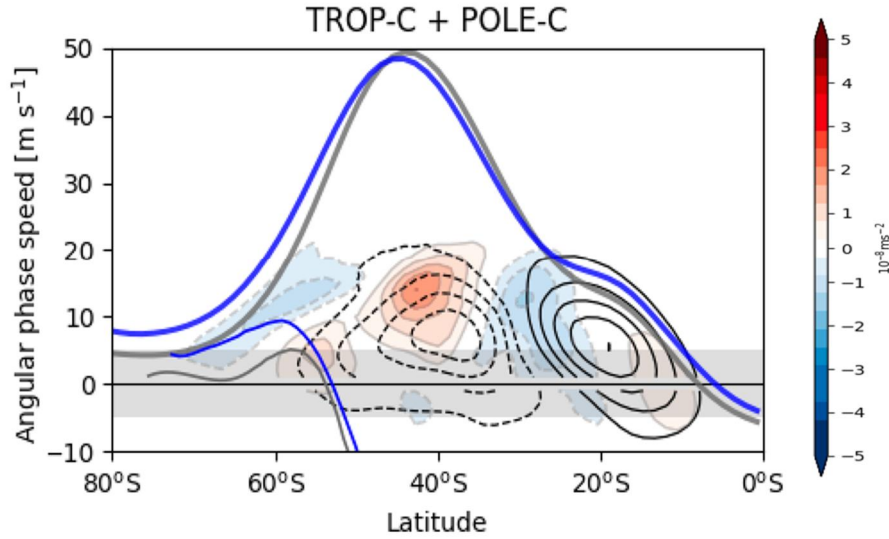


Figure 4.4. Eddy Momentum flux at 250 hPa (EMF250) divergence cospectra (10^{-8} m s^{-2} , contours) as a function of angular phase speed and latitude in the linear summation of TROP-C and POLE-C in Figs. 4.2b and c, respectively. The differences in EMF divergence in the summation from CTRL are shaded, with anomalous divergence in blue and convergence in red. Contours are depicted from $-6 \times 10^{-8} \text{ m s}^{-1} \text{ day}^{-1}$ to $6 \times 10^{-8} \text{ m s}^{-1} \text{ day}^{-1}$ with intervals of $1 \times 10^{-8} \text{ m s}^{-1} \text{ day}^{-1}$, and the shading range is from $-5 \times 10^{-8} \text{ m s}^{-1} \text{ day}^{-1}$ to $5 \times 10^{-8} \text{ m s}^{-1} \text{ day}^{-1}$ with intervals of $0.4 \times 10^{-8} \text{ m s}^{-1} \text{ day}^{-1}$. Thick and thin curves indicate the critical latitude and the reflective latitude for zonal wavenumber 6, respectively, for CTRL (gray) and cooling experiments (colored). Gray shaded phase speed range of -5 to 5 m s^{-1} denotes a slow phase speed range described in the text.

The critical latitude changes in the tropics largely influence the waves which propagate into the tropics and drive the EMF250 divergence. In TROP-C, the zonal wind strengthens on the equatorward flank of the jet ($0^\circ < \phi < \sim 35^\circ$) for waves with phase speeds of -5 to 40 m s^{-1} (thick colored line in Fig. 4.3b). This wind change causes an

equatorward shift of the critical latitude for a given wave phase speed, allowing equatorward-propagating waves to break at the deeper tropics. The net result is an equatorward shift of the EMF divergence, which is associated with the equatorward shift of the HC edge in TROP-C compared to the CTRL. In the COMB-C, the tropical zonal wind increase is found for the phase speed of -5 to 15 m s^{-1} (Fig. 4.3d).

In Figs. 4.3 and 4.4, we focus on the wave with zonal wavenumber $k = 6$ with phase speed $c = 5 \text{ m s}^{-1}$. This is selected based on the wavenumber-angular phase speed cospectra for the EMF convergence in the tropics and the midlatitudes (Fig. 4.5). Figure 4.5 reveals that the $k=6$ wave is one of the most important waves to simply explain the opposing HC-jet changes. For instance, in TROP-C, short waves with zonal wavenumbers $k=6\sim9$ are more responsible to the EMF divergence in the tropics compared to those in CTRL. On the other hand, in the midlatitude, the short waves with $k = 5$ to 7 have a larger contribution to the EMF convergence compared to the CTRL. The exact opposite is true for POLE-C. Their combinations are mostly attributed to the waves with $k = 5$ to 7 . Although not shown, change in wave propagation and reflection from the perturbed run to the CTRL run was also measured for other wavenumbers. The reflective profiles for other waves in response to thermal forcing broadly resemble the profiles in Fig. 4.3 except for the

profiles for waves with zonal wavenumber $k = 1-5$. The reflective profile is not seen by long waves with a positive phase speed for wavenumbers $k = 1-5$. This suggests that long waves, i.e., planetary ($k = 1-3$) and longer synoptic eddies (approximately $k = 4-5$), are rarely influenced by the change in reflective profiles.

The above result suggests that both the coherent and opposing HC-jet shifts are determined by the upper-tropospheric eddies, but the only difference is how much the eddies control the HC and the jet. The structural changes of the EMF related to the opposing HC-jet shifts imply that the eddy influences differently on the HC edge and the jet latitude in response to tropical/polar forcings.

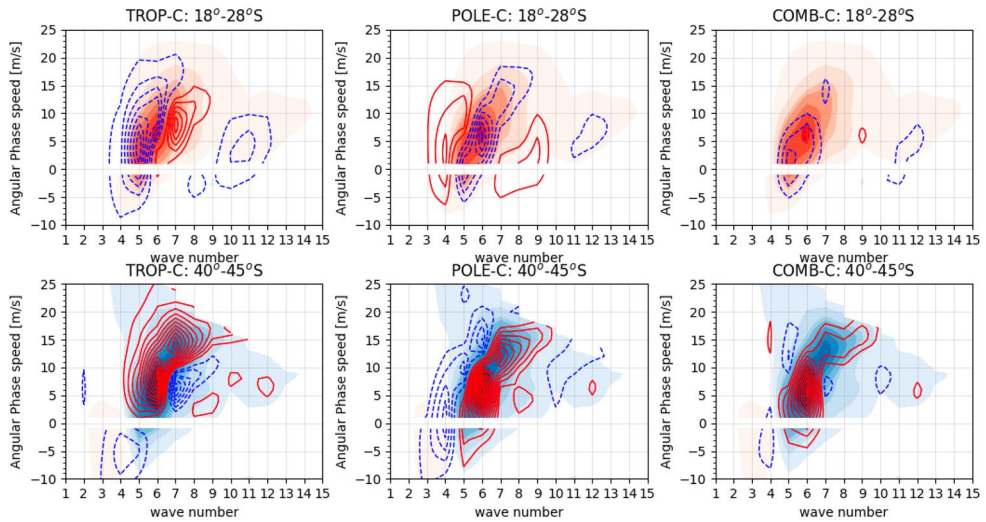


Figure 4.5. Zonal wavenumber-angular phase speed cospectra for the eddy momentum flux convergence at 250 hPa (a, b, c) at the tropics (18–28°) and (d, e, f) at the midlatitudes (40–45°) for (shading) CTRL (Unit:

$10^7 \text{ m s}^{-1} \text{ day}^{-1}$). The changes of the EMF divergence for (a, d) TROP-C, (b, e) POLE-C, and (c, f) COMB-C compared to CTRL are in contours. The contour and shading intervals are $0.5 \times 10^7 \text{ m s}^{-1} \text{ day}^{-1}$.

4.3 Axisymmetric circulation response to thermal forcing

To identify the role of baroclinic eddies in the opposing HC–jet changes, the axisymmetric experiments are further performed, and the results are compared to non-axisymmetric runs discussed in previous sections. The primary goal of this comparison is to isolate the influences of the baroclinic eddies on the HC-edge shifts. Although this comparison does not guarantee complete separation of the role of eddies from that of mean flow change because of the complex nature of the eddy-mean flow interaction (e.g., Kim and Lee 2001a), it still provides a helpful insight on the importance of eddies (e.g., Kim and Lee 2001a; 2001b). The axisymmetric (simply, “2D”) experiments performed here are identical to the non-axisymmetric experiments discussed in previous sections, except that the eddies are not permitted by integrating the model with a two-dimensional configuration. All 2D experiments are conducted for 1,500 days and the last 1,000 days are analyzed after discarding the first 500 days of spin-up time.

The 2D_CTRL experiment exhibits a well-defined HC (contours in Fig. 4.6d) and a subtropical jet on its poleward edge at 25.7°S (contours

in Fig. 4.6g). They are mostly driven by angular momentum conservation as discussed by Held and Hou (1980). In the absence of eddies, the HC edge in the 2D_CTRL is located closer to the equator than its counterpart in the eddy-permitting (simply, “3D”) experiment (27.0°S) (Kim and Lee 2001a; 2001b). No organized mean meridional circulations and midlatitude westerlies are found as eddies are not permitted (Kim and Lee 2001a). Figure 4.6 also illustrates the responses of temperature and zonal wind to tropical cooling, polar cooling, and both (2D_TROP-C, 2D_POLE-C, and 2D_COMB-C, respectively) in 2D simulations. As in 3D reference simulations, the zonal-mean circulation changes in the 2D_COMB-C (shaded in the right column of Fig. 4.6) are very similar to the sum of those in the 2D_TROP-C and 2D_POLE-C (Fig. 4.7). This is well corresponding to the small local Rossby number in the deep tropics which indicates the larger influences of angular momentum conservation in the tropics than eddy fluxes (Fig. 4.8).

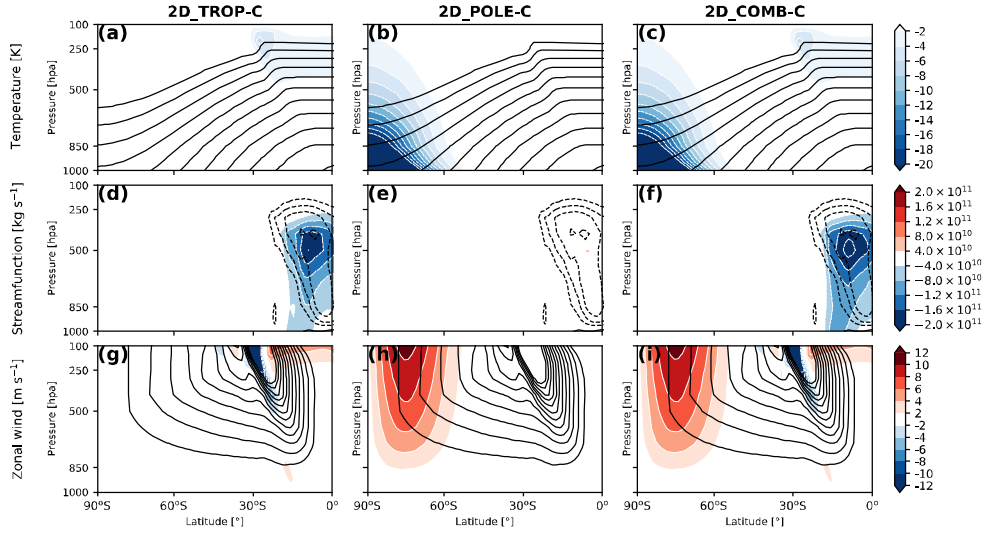


Figure 4.6. (top) Temperature (unit: K), (middle) mass streamfunction (unit: $10^{10} \text{ kg s}^{-1}$), and (bottom) zonal wind (unit: m s^{-1}) in 2D-CTRL (contours) and their responses to the thermal forcings (shading; 2D-EXP minus 2D-CTRL) in axisymmetric simulations with $(q_{\text{trop}}, q_{\text{pole}}) = (-0.3, 0.0)$, $(0.0, -2.8)$, and $(-0.3, -2.8) \text{ K day}^{-1}$ from left to right columns. See section 2.2.4 for the details of the model experiments. Contours for top, middle, and bottom panels are from 210 to 350 K, -1.2×10^{11} to $1.2 \times 10^{11} \text{ kg s}^{-1}$, and 5 to 60 m s^{-1} with their intervals 10 K, $10^{10} \text{ kg s}^{-1}$, and 5 m s^{-1} , respectively, excluding zero lines.

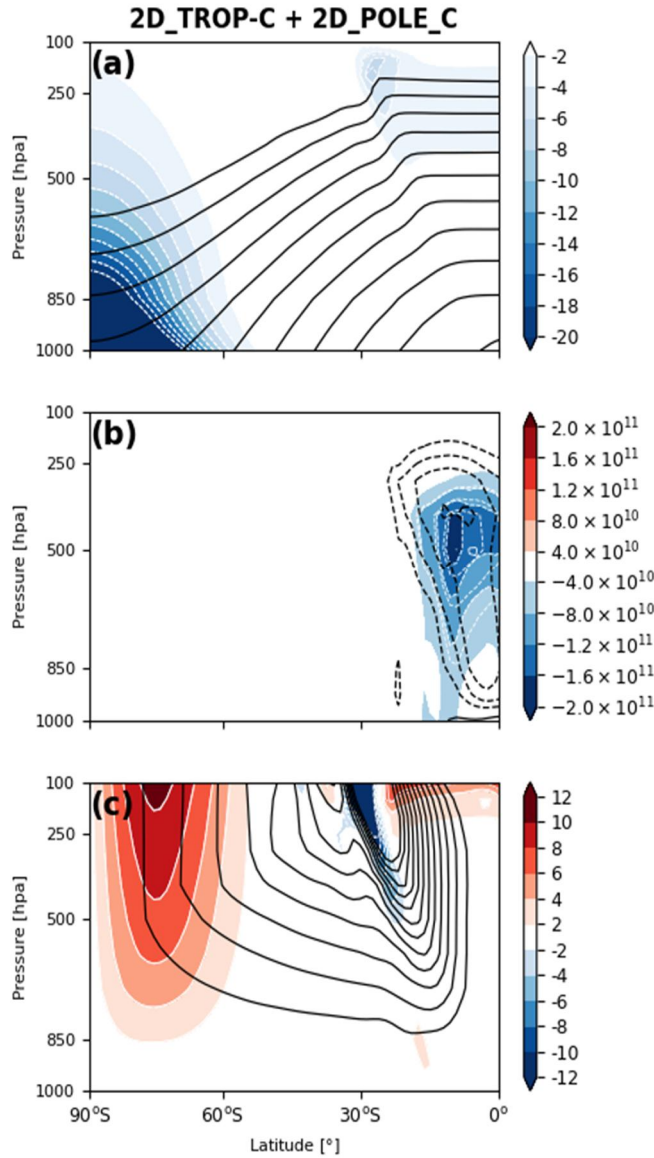


Figure 4.7. (a) Temperature (unit: K), (b) mass streamfunction (unit: $10^{10} \text{ kg s}^{-1}$), and (c) zonal wind (unit: m s^{-1}) in 2D-CTRL (contours) and their responses in the linear summation of 2D_TROP-C and 2D_POLE-C (shading; linear summation *minus* 2D-CTRL) in axisymmetric simulations. Contours for top, middle, and bottom panels are from 210 to 350 K, -1.2×10^{11} to $1.2 \times 10^{11} \text{ kg s}^{-1}$, and 5 to 60 m s^{-1} with their intervals 10 K, $10^{10} \text{ kg s}^{-1}$, and 5 m s^{-1} , respectively, excluding zero lines.

The axisymmetric HC changes in response to thermal forcing are quantified by conducting 2D parameter sweep experiments. As anticipated from previous studies (e.g., Held and Hou 1980), the HC becomes narrower as the equator-to-pole temperature gradient is reduced by the tropical cooling (Fig. 4.9). More importantly, the 2D-HC edge shifts equatorward as the magnitude of q_{trop} increases with the rate of $-6.4^\circ / (\text{K day}^{-1})$ (Fig. 4.9), which is comparable to that in the 3D simulation ($-8.8^\circ / (\text{K day}^{-1})$). This result suggests that an equatorward HC-edge shift in response to tropical cooling in the 3D simulations is driven not solely by eddy flux changes but also by axisymmetric circulation changes. This finding is consistent with the conjecture that low-latitude EMF250 divergence (and HC-edge) changes in the 3D simulation are not solely determined by changes in the midlatitude baroclinicity (Fig. 4.1).

By comparing the 2D_TROP-C and 2D_POLE-C, it is noticeable that the high-latitude westerlies are enhanced due to the polar cooling (Figs. 4.6d, e). This suggests that high-latitude zonal wind can be strengthened even without eddy. If this wind change interacts with waves in non-axisymmetric runs, wave reflection on the poleward flank of the jet could be enhanced (Lorenz 2014).

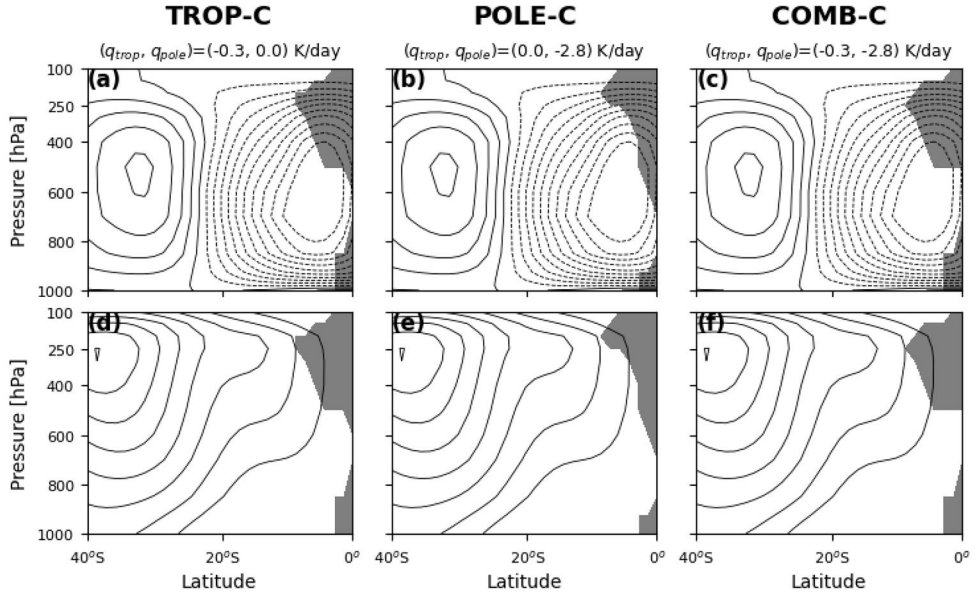


Figure. 4. 8. (contours) The mass streamfunction (upper) and the zonal wind (lower) for (a, d) TROP-C, (b, e) POLE-C, and (c, f) COMB-C. The results are from the three-dimensional (3D) equilibrium experiments shown in Figs. 3.10 and 3.11. The gray shading denotes the area where the local Rossby number is greater than 0.5. Contours are from -20 to $20 \times 10^{10} \text{ kg s}^{-1}$ with intervals of $2 \times 10^{10} \text{ kg s}^{-1}$ for mass stream function, and 0 to 40 m s^{-1} with the interval of 5 m s^{-1} for zonal wind.

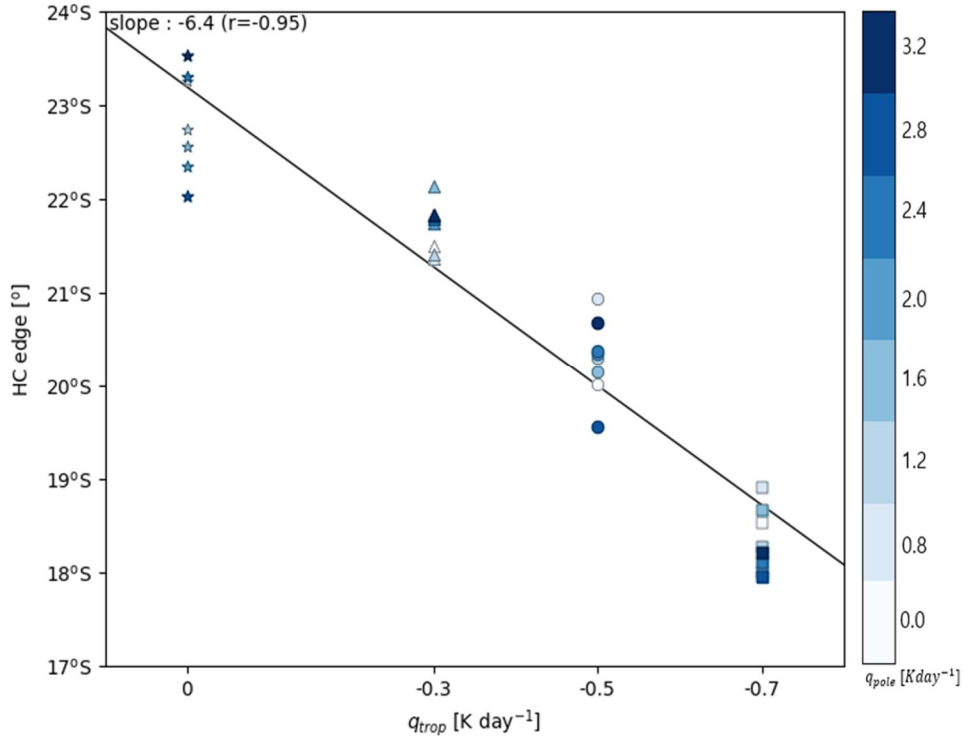


Figure 4. 9. The HC edges in response to tropical cooling (q_{trop}) in the axisymmetric cooling simulations. Color on markers denotes the amplitude of polar cooling (q_{pole}) from 0 to -3.2 K day^{-1} . The linear regression line is denoted in black line.

4.4 Transient response of circulation

4.4.1 Motivation

Although both the HC edge and jet latitude are related to the EMF, their mechanisms are quite different. Eddies allow the HC to extend and strengthen (e.g., Kim and Lee 2001; Walker and Schneider 2006; Caballero 2007; Ceppi and Hartmann 2013; Davis and Birner 2019). The HC edge is highly correlated with the latitude at which eddies deepen and reach the upper troposphere (e.g., Levin and Schneider, 2015). At that latitude, the Rossby wave propagates and dissipates, with impacts on the zonal momentum balance. However, since the HC is a thermally driven circulation, it can also be influenced by the upper tropospheric zonal wind associated with the HC itself (e.g., Sobel and Schneider 2009; Bordoni and Schneider 2010).

The above literature suggested that the opposing HC–jet change could be related to the Antarctic amplification in LGM, but the detailed mechanism is still unclear. Since the circulation changes are strongly tied to the eddy activities, it is essential to investigate how eddies act in the opposing HC–jet change. According to the linear wave theory, Rossby waves propagate from their source region to the critical latitudes, where their phase speeds are equal to the background zonal wind. The breaking waves, represented by EMF divergence, deposit the easterly momentum

decelerating the background wind. A bunch of studies proposed that the jet shift likely occurs in response to the temperature change via changes in eddy activities, such as the propagation, growth, and dissipation of baroclinic eddies (Son and Lee 2005; Chen and Held 2007; Lu et al. 2010; Kidston et al. 2010; 2011; Lorenz 2014). For example, Son and Lee (2005) showed that the response of fast-moving eddies to external thermal forcings is different from that of slow-moving eddies. Chen and Held (2007) suggested that the eddy phase speed change plays an important role in determining the jet latitude change in the recent past. Lorenz (2014) further highlighted the importance of eddy phase speed changes to determine the poleward flank of the jet in a poleward-shifted jet. On the other hand, Kidston et al. (2010; 2011) argued that the increased eddy length scale is likely the main cause of the poleward jet shift under global warming by altering static stability in the lower troposphere. Lu et al. (2010) claimed a linear relationship between the jet latitude and the maximum eddy heat flux (EHF) in the lower troposphere, which can generally be considered as a position of wave generation.

The majority of the above studies have been based upon the circulation changes under global warming or global warming-like climate states. The purpose of this section is to quantitatively investigate dynamics of the opposing HC-jet change under the global cooling

conditions. In this section we focus on the separate roles of tropical and polar thermal forcings in opposing HC-jet shifts. To better understand this opposing HC-jet shift, a set of cooling experiments is examined in detail.

4.4.2 Time evolution of circulation change

We utilize the dry dynamic core of GFDL GCM which is the same model used in Chapter 4. The only difference is that we focus on the spinup ensemble simulations in this section. See section 2.2 for a detailed description of the control simulation. The control simulation is conducted during 5,000 days. The perturbed transient experiments are indicated in section 2.2.3.

To examine the atmospheric change, the transient experiments' average evolutions of the latitudinal-pressure structure are investigated for both cases (Figs. 4.10 and 4.11). The transient experiments' average evolution of zonal mean temperature, zonal-mean zonal wind, mean meridional circulation (MMC), and the eddy momentum fluxes in EXP-C are shown in Fig. 4.10. Top two rows of Fig. 4.10 show the response to thermal forcing, which are presented as 10-day averages with the difference taken relative to the 5000-day mean of the control run. The bottom row presents the 100-200 day mean of the perturbed run

compared to the control run, indicating a quasi-equilibrium state. Similar results are found when displayed by the difference taken relative to the average of the equivalent 10 days of the control run.

In days 5 to 15, it is apparent that the tropical cooling decreases the temperature gradient equatorward of $\sim 30^\circ\text{S}$ latitude in the upper troposphere. This induces poleward flow and a westerly anomaly with increased vertical wind shear immediately to maintain thermal wind balance at the upper troposphere around 250 hPa.

The MMC response also appears near the beginning of the spinup (Fig. 4.10c). On days 5 to 15, the altered temperature gradient in the upper level will tend to drive an anomalous indirect circulation equatorward of $\sim 30^\circ$ latitude and a direct circulation poleward of this. It consists of strengthening of the Hadley cell and Ferrell cell in the tropics and the midlatitudes. This dipole pattern continues to increase in magnitude as time progresses and has extended throughout the depth of the troposphere. The strengthened Hadley cell coincides with the

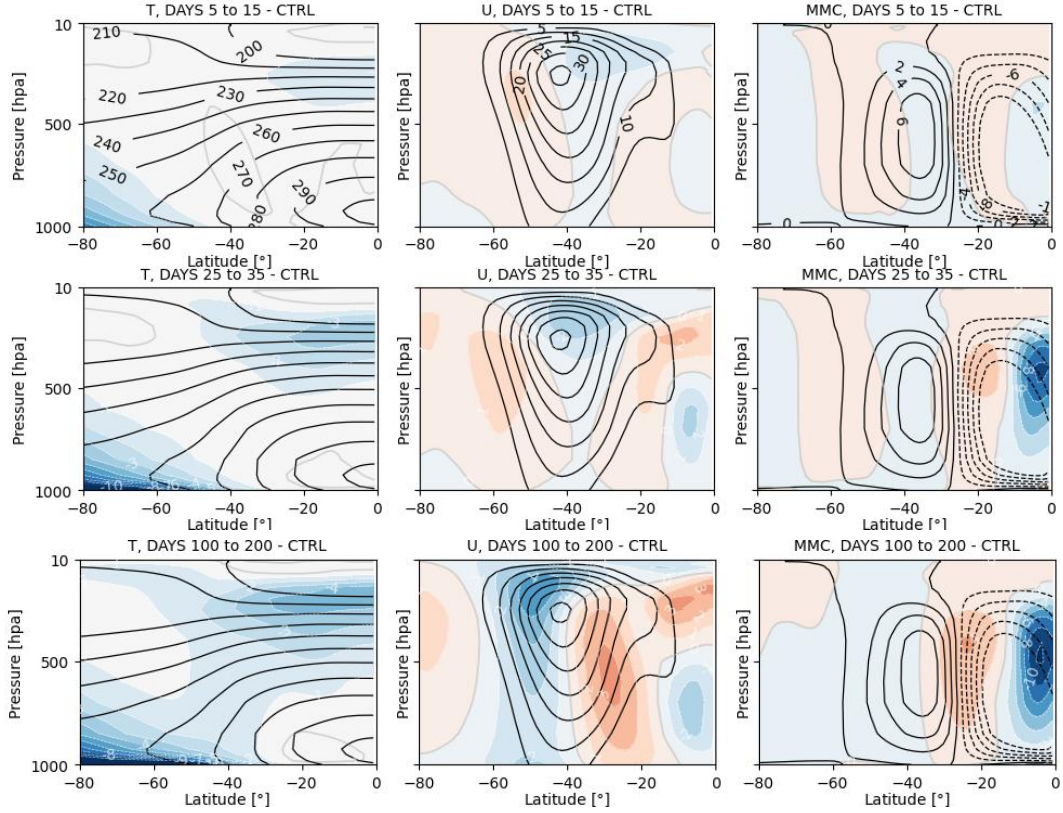


Figure 4.10. Evolution of zonal-mean temperature (unit: K), zonal wind (unit: m s^{-1}), mean meridional circulation (MMC; unit: $10^{10} \text{ kg s}^{-1}$), and eddy momentum flux (EMF; unit: $\text{m}^2 \text{ s}^{-2}$) fields for the coherent case. (top) Control run values; (middle) difference between 10-day averages of the transient and the control run for days 5 to 15, for days 25 to 35, and (bottom) difference between the last 100-day average quasi-equilibrium states and the control run. (bottom) The control run in the top row is presented again in gray lines for the comparison.

decreased upper-level temperature in the tropics. (The anomalous descent in the subtropics near 18°S induces adiabatic warming). In response to the tropical cooling, there is a horizontal dipole in the change in horizontal eddy momentum flux, which gives a triple of forcing. This triple corresponds to the latitudes of the three-cell pattern in the

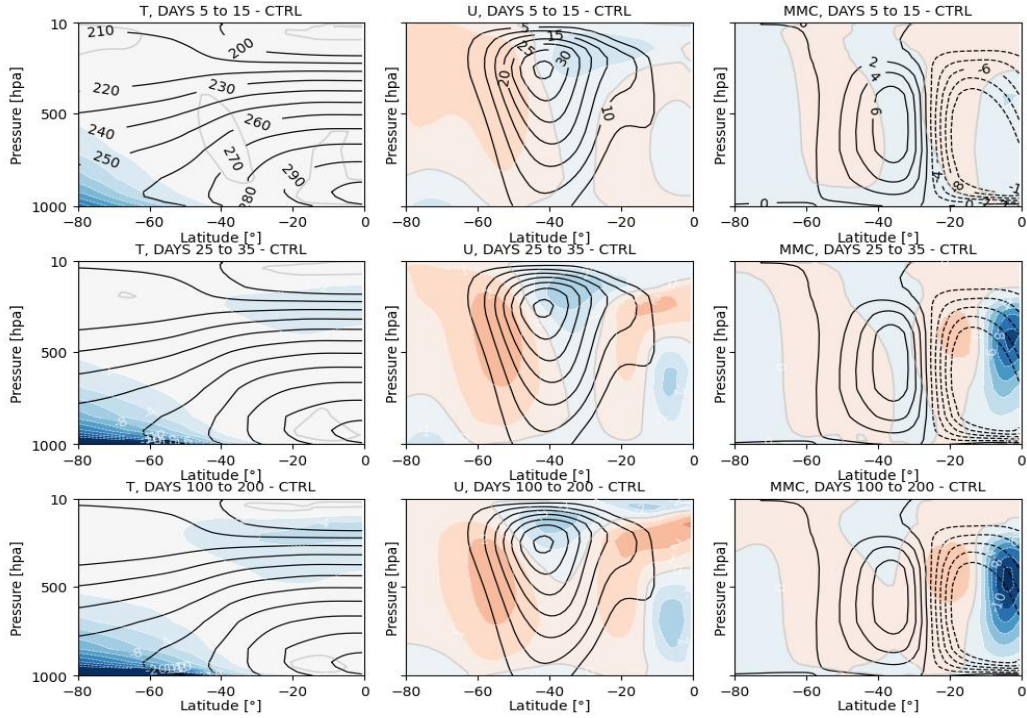


Figure 4.11. Evolution of zonal-mean temperature (unit: K), zonal wind (unit: m s^{-1}), mean meridional circulation (MMC; unit: $10^{10} \text{ kg s}^{-1}$), and eddy momentum flux (EMF; unit: $\text{m}^2 \text{ s}^{-2}$) fields for the EXP-O. The overall format of the figure is identical to the Fig. 4.10.

meridional circulation anomalies. Change in the convergence of poleward eddy heat flux acts to oppose these tropospheric temperature changes. As such, as the experiment meets the equilibrium state, the adiabatic cooling and convergence of the poleward eddy heat flux are in a balance. This is further demonstrated in the top panels of Fig. 4.14, which show the time series of the change in each of the forcing terms in Eq. (4.1) along with their sum and the zonal wind anomaly, averaged between 700 hPa and the top of the model.

The evolutions of circulation changes in EXP-O with -0.3 K day^{-1} of tropical cooling and -2.8 K day^{-1} of polar cooling are illustrated in Fig. 4.11. The zonal wind change starts at the very first time step, pronounced by the acceleration on the poleward flank, deceleration on the jet core, and acceleration in the subtropics. This triple change of the zonal wind quite resembles the equilibrium wind response of COMB-C as shown in Fig. 3.11(f). A response in mean meridional circulation is found in the third column of Fig. 4.11. As in the coherent case, during days 5 to 15, the anomalous clockwise circulation (positive) centered at 20°S and the anomalous counterclockwise circulation (negative contours) in the deep tropics from 15°S to 0°S are pronounced, starting in the upper troposphere. This results in the equatorward shift of the HC edge in this opposing case. The difference from the coherent MMC change is the MMC response in the high latitudes. While the high-latitude MMC change is negligible in the coherent case (see Fig. 4.10), an anomalous indirect circulation has also appeared at high latitudes. This three-cell pattern continues to increase in magnitude as time progresses.

Evolving changes of the HC edge and jet latitude are illustrated in Fig. 4.12. Circulation changes do not sensitive to the amplitude of the forcings, especially during the initial 20 days. While the HC edge shifts equatorward together at the very beginning of both experiments (Fig.

4.12a), the jet-jet latitude changes are peculiar (Fig. 4.12b). During the initial 20 days, the jet latitude shifts poleward together. The westerly change is thought of as a combination of the tropical cooling-induced equatorward shift and the polar cooling-induced poleward shift, the former forced by the decreased static stability and the latter being the result of midlatitude eddies. The jet latitude in the initial 20 days is dominated by the polar cooling. The jet latitudes in EXP-C and EXP-O become differentiated after 20 days. After the first 20 days, the jet latitude in EXP-C switches its sign, shifting equatorward rapidly during the initial 90 days, and then saturated (green in Fig. 4.12b). This reflects that the impact of tropical cooling overwhelms that of polar cooling after initial 20 days. By contrast, the jet latitude in EXP-O shifts further poleward but with a larger variability (blue in Fig. 4.12b). A poleward shift of the jet in EXP-O is a result of the dominant polar cooling beyond the tropical cooling. The jet latitudes in both experiments meet their equilibrium states after approximately 150 days.

To estimate the response time of the circulations to given thermal forcings, the e-folding time is quantified by fitting the evolutionary changes of the HC edges and jet latitudes to the exponential function as in Chemke and Polvani (2019). The longer response time indicates that the circulation meets its equilibrium state more slowly. Calculation of

response time for the HC edges reveals that the HC responds slowly as the polar cooling is stronger. While the HC edge takes 45 days in EXP-O, it takes 57 days in EXP-C. The jet change is more complex. The jet latitude in EXP-O only needs 18 days to meet its equilibrium state but the response time of the jet latitude in EXP-C is about 133 days. Such a much longer response time in EXP-C is primarily due to the switched sign of the jet latitude within the first 30 days. However, discarding first 30 days, EXP-C presents a longer response time than that in EXP-O.

Note that the response time for the jet latitude has a wider range compared to that for the HC edge. While the HC edges are saturated around day 50–60 in both EXP-C and EXP-O, the response time for the jet latitude in EXP-C, which is 133 days, becomes 18 days when polar cooling is enhanced (in EXP-O; blue in Fig. 4.12b). This implies a higher sensitivity of the jet latitude than that of the HC edge to the amplitude of polar cooling. This result is corresponding to a higher sensitivity of the jet to polar cooling forcing than its HC-edge counterpart in the equilibrium states from section 3.4.

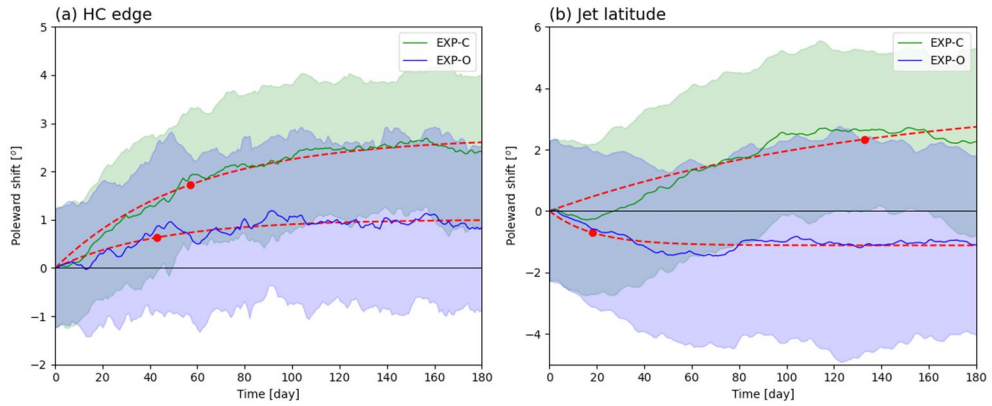


Figure 4.12. Time evolutions of (left) ensemble-mean HC edge and (right) jet latitude changes in EXP-C (green) and in EXP-O (blue) from CTRL. Their one-standard deviation range across ensembles are denoted by shading. A negative value denotes a poleward shift (southward shift).

4.4.3 Changes in mean meridional circulation (MMC)

The changes in mean meridional circulation (MMC) are further investigated with a focus on their changes at the midtroposphere. The zonal mean momentum budget can be written as

$$\frac{\partial \bar{u}}{\partial t} = (f + \zeta) \bar{v} - \bar{\omega} \frac{\partial \bar{u}}{\partial p} - \frac{1}{a \cos^2 \phi} \frac{\partial \overline{u'v'} \cos^2 \phi}{\partial \phi} - \frac{\overline{u'\omega'}}{p} - \bar{F} \quad (4.1)$$

where F denotes the surface friction, and other symbols follow meteorological conventions. Making the small Rossby number approximation ($f \gg \zeta$) and small aspect ratio approximation, the MMC at the mid-tropospheric level (≈ 500 hPa) can be diagnosed as

Ψ_{500}

$$\begin{aligned} &\equiv \frac{2\pi a \cos \phi}{g} \int_{500 \text{ hPa}}^0 \bar{v} dp \sim \frac{2\pi a \cos \phi}{gf} \left\{ \int_{500 \text{ hPa}}^0 \frac{\partial \bar{u}}{\partial t} dp \right. \\ &\quad \left. + \frac{1}{a \cos^2 \phi} \int_{500 \text{ hPa}}^0 \frac{\partial \overline{u'v'} \cos^2 \phi}{\partial \phi} dp \right\} \end{aligned} \quad (4.2)$$

where the subscript U denotes an average from the top of the atmosphere to $p_{500} = 500 \text{ hPa}$ and the upper tropospheric average of X is denoted as

$$\langle X \rangle \sim \frac{1}{p_{500}} \int_{500 \text{ hPa}}^0 X dp.$$

Figure 4.13 shows the 500-hPa MMC (Figs. 4.13.a, b) simulated in the model in comparison with the MMC (Figs. 4.13.c,d) diagnosed from the momentum budget above in EXP-C, and EXP-O. While the two disagree in the tropics equatorward side owing to a large Rossby number and nonlinear HC dynamics (e.g., Held and Hou 1980), the momentum budget provides a strong constraint on the MMC poleward of 15° . In contrast, for the subtropics ($20\text{--}40^\circ$), the MMC is dominated by the eddy momentum flux divergence, and less influenced by the zonal wind tendency in both cases (not shown). This indicates that the equatorward shift of the HC edge is primarily driven by the change of eddy momentum flux, while the interior of the HC is dominated by diabatic heating in the deep tropics. Note that the MMC change by eddy momentum flux near the HC edge of the CTRL run (dashed line) is stronger in EXP-C than in

EXP-O. This corresponds to the HC edge in EXP-C which shifts farther equatorward than the HC edge in EXP-O.

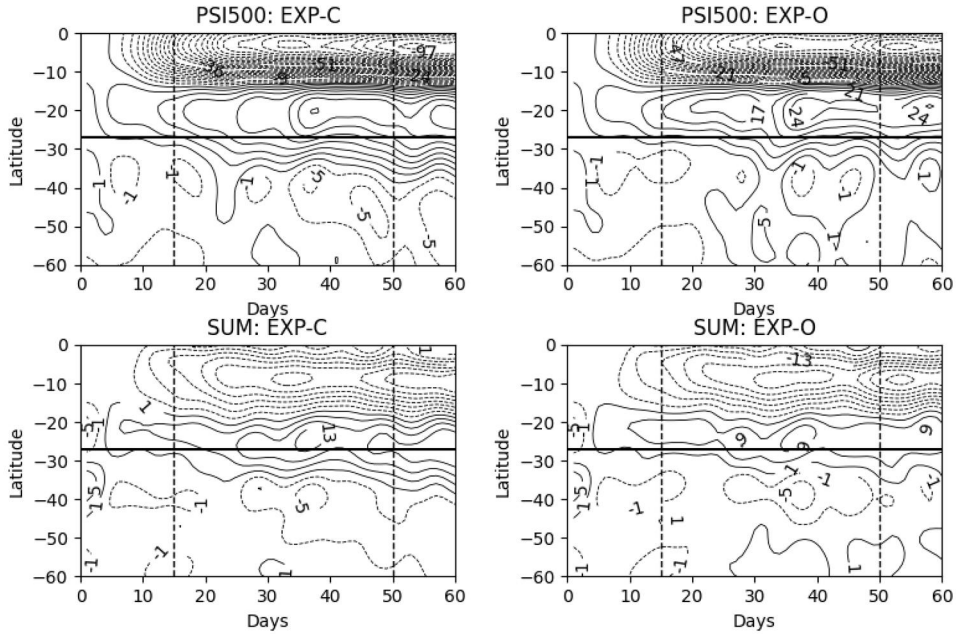


Figure 4. 13. Zonal and ensemble-mean transient responses of 500-hPa meridional streamfunction ($10^{10} \text{ kg s}^{-1}$) as a function of latitude and time: (a, b): simulated and (c, d) diagnosed from the momentum budget [Eq. (4. 2)].

4.4.4 Change in zonal winds

Recall the primitive equation of zonal-mean zonal momentum in Eq. (1.1). The first and second terms on the right-hand side of Eq. (1.1) indicate the convergence of meridional eddy momentum flux and the Coriolis force. The third, fourth, and fifth terms are meridional and vertical advection of zonal-mean zonal wind, and the convergence of

vertical momentum fluxes, respectively. The last two terms represent the surface damping term and the residual term.

To quantify the importance of eddy momentum flux, the zonal momentum balance, briefly introduced in the introduction in Chapter 1, is further analyzed here for both coherent and opposing cases. By ignoring the dependence of the ageostrophic terms to the zonal-wind term, the zonal momentum balance equation in Eq. (1.1) can be integrated in time 0 to t as below:

$$\begin{aligned}\bar{u}(t) - \bar{u}(0) = & \frac{1}{e^{kt}} \left[\int_0^t e^{kt} f \bar{v} dt \right. \\ & + \int_0^t -e^{kt} \frac{1}{a \cos^2 \varphi} \frac{\partial \overline{u'v'} \cos^2 \varphi}{\partial \varphi} dt \\ & \left. + \int_0^t e^{kt} (\text{ageostrophic terms}) dt \right]. \quad (4.3)\end{aligned}$$

The left-hand side term is a zonal wind anomaly. The zonal momentum budget is analyzed by averaging Eq. (4.3) from the top of the model to the 700 hPa, where $k=0$. Thus follow three terms act to change u : the Coriolis force acting on the anomalous mean meridional wind, the change in horizontal eddy momentum flux (EMF) convergence, and the ageostrophic terms. Mean meridional wind anomalies arise in response to thermal wind imbalances created directly by anomalous heating and by anomalous eddy fluxes. According to the QG dynamics, the first two terms, Coriolis and the EMF terms are balanced to each other.

The budget analysis is conducted for the quantities area-averaged over the two latitude ranges: 1) a poleward flank of the CTRL jet from 55°S to 58°S, and 2) the tropics (17°S to 20°S). The sensitivity of the latitudinal ranges is tested, and the results are quantitatively similar. The results from the zonal momentum balance budget are presented in Fig. 4.14. Figure 4.14 demonstrates that the sum of the RHS terms is well matching to the zonal wind anomalies on the left-hand sides. This is largely shown in all three latitude areas. Given the good agreement between the sum of the terms on the right-hand side of Eq. (4.3) and the u anomaly, this appears to be a reasonable approximation.

The leftmost figures in Fig. 4.14 depict the each of terms in Eq. (4.3) on the poleward flank of the jet. It is apparent that the EMF convergence and the Coriolis terms are two major components in modulating the zonal wind. Their imbalance is largely attributed to the zonal wind anomalies on the poleward flank of the jet (green curves). It is also notable that the EMF divergence term acts to decelerate the zonal wind in the very first 20 days. From day 20, in the opposing case, the EMF term switches its sign to the positive, indicating the EMF convergence and accelerating the zonal wind in this latitude. The Coriolis term follows the change of the EMF term, decelerating the zonal wind against the acceleration due to EMF convergence. This wind acceleration by EMF

convergence might be related to the extended EMF up to high latitudes in EXP-O (not shown). Similarly, the zonal wind change on the equatorward flank of the jet is well explained by the imbalance of EMF convergence and the Coriolis terms.

Overall changes of zonal wind anomalies and the forcing terms are similar in both coherent and opposing cases, again showing that the tropical wind change is less influenced by the polar cooling as shown in Chapter 3. It turned out that the EMF convergence term is much weaker in the tropics, compared to the higher latitudes. Instead, the right column of Fig. 4.14 presents that the term of vertical advection of zonal wind (gray dashed line) contributes to the zonal wind acceleration in the tropics. This likely results from the tropical cooling, which is identically imposed in both coherent and opposing cases. The tropical cooling reduces the meridional temperature gradient in the upper troposphere, inducing a decrease in vertical wind shear via thermal wind balance.

From the quasi-geostrophic scaling above, the midlatitude westerly wind can be roughly thought of as the result of the balance between the eddy momentum convergence and the surface friction. Indeed, the evolutions of the vertically integrated EMFC display a rather similar temporal structure to the near-surface wind (Fig. 4.15). The dominance of the eddy momentum forcing is further confirmed by a

direct calculation of the momentum advection by the zonal mean wind components: the latter in the extratropics is an order of magnitude smaller than the former.

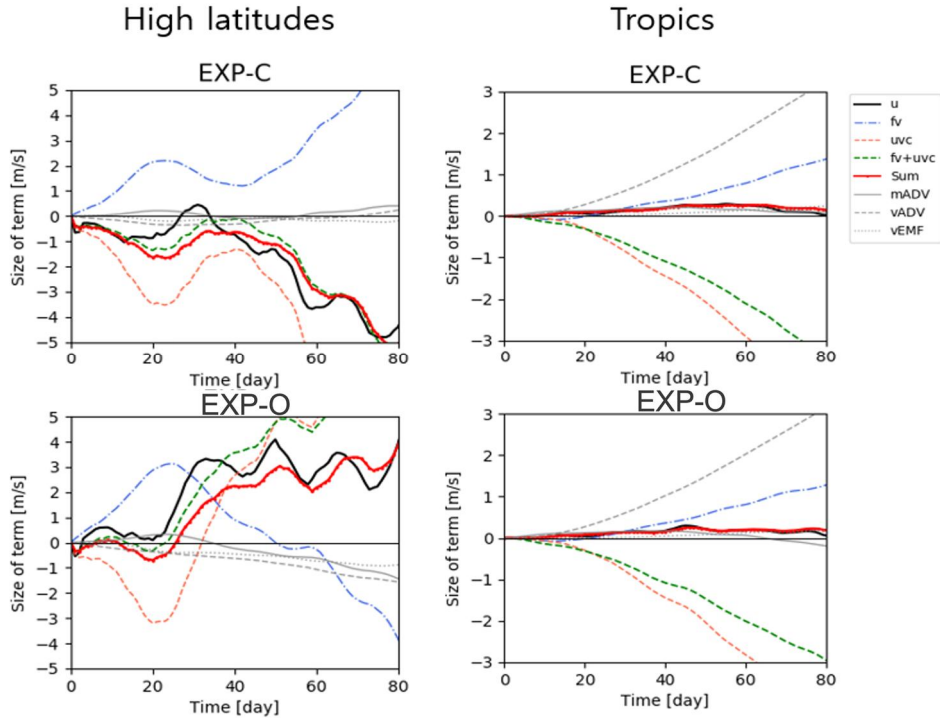


Figure 4.14. Ten-day running means of the change in each of the terms in Eq. (5.3) along with their sum (red solid) and the zonal wind anomalies (black solid) from the control run (top) in EXP-C (bottom) in EXP-O [$uvc = 2^{nd}$ term of Eq. (5.3)] averaged from the top of the model to 700 hPa.

Figure 4.15 provides the temporal evolutions of the zonal wind at the 850 hPa level and the vertically integrated EMFC. The coincidence between the zonal wind maximum and the EMFC maximum is well found in time, including the switched sign of the jet latitude in Phase 2 of EXP-

C. This again demonstrates that the jet-latitude change could be understood in terms of the EMFC.

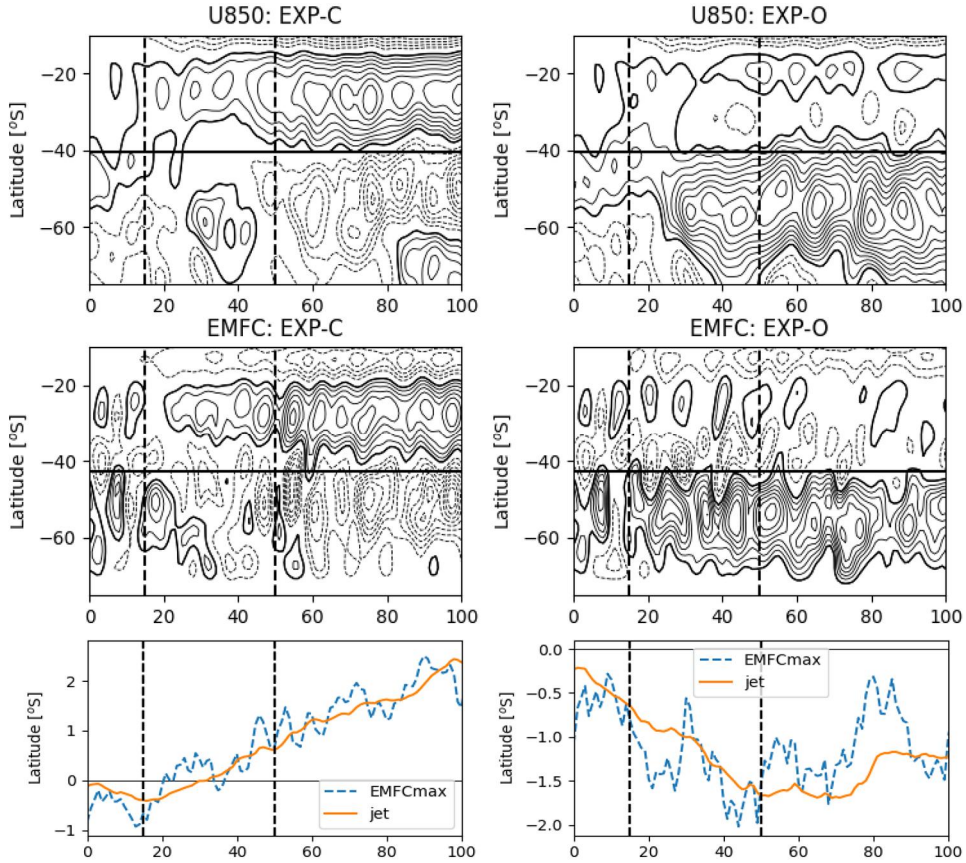


Figure 4.15. Zonal and ensemble-mean transient responses of 850-hPa zonal wind (unit: m s^{-1}) and vertically integrated eddy momentum flux convergence (EMFC; unit: m s^{-2}) as a function of latitude and time in (left) EXP-C and (right) EXP-O experiments.

4.4.5 Mechanisms of the tropospheric jet shift

Rossby waves break into two types: cyclonic wave breaking (CWB) and anticyclonic wave breaking (AWB). AWB and CWB give rise to the

contrasting impacts on the jet-latitude changes. While the AWB events push the jet poleward, the CWB events induce an equatorward shift of the jet (Thorncroft 1993).

Following Strong and Magnusdottir (2008), the wave-breaking types are computed based on the 340-PVU isentropic potential vorticity (PV) surface (Riviere 2009). We calculate the wave-breaking density, which is the frequency of occurrence of CWB and AWB per day. Figure 4.16 displays the difference between the two wave-breaking densities, AWB-CWB densities. It is of interest that the AWB-CWB densities in EXP-C and EXP-O have particularly diverged in Phase 2. The AWB-CWB densities are 0.08 in Phase 1, indicating that the AWB events occur a bit more than the CWB events. While the AWB-CWB density in EXP-C keeps its value during Phase 2, those in EXP-O rapidly increase in Phase 2, reaching to 0.15 at the end of Phase 2. In Phase 3, the wave-breaking difference densities are in a steady state.

Such evolutions of wave-breaking densities suggest a possibility of the wave-breaking-related processes in response to polar cooling. The relative increase of AWB events to CWB events leads to the poleward shift of the jet (Thorncroft 1993). Then, what makes such an increase in AWB events in Phase 2? This is driven by the polar cooling-induced low-level baroclinicity change. The polar cooling induces the enhancement of

baroclinicity on its poleward flank around 60° to 80°S (Fig. 4.17). This is clearly found in Phase 1 in both EXP-C and EXP-O. This increase in baroclinicity in high latitudes could lead to wave generation, particularly for long waves. This is well corresponding to the large contribution of long waves to the enhancement of low-level baroclinicity in response to strong polar cooling as found in the equilibrium simulations (Fig. 4.1). Overall processes are summarized in Fig. 4.18.

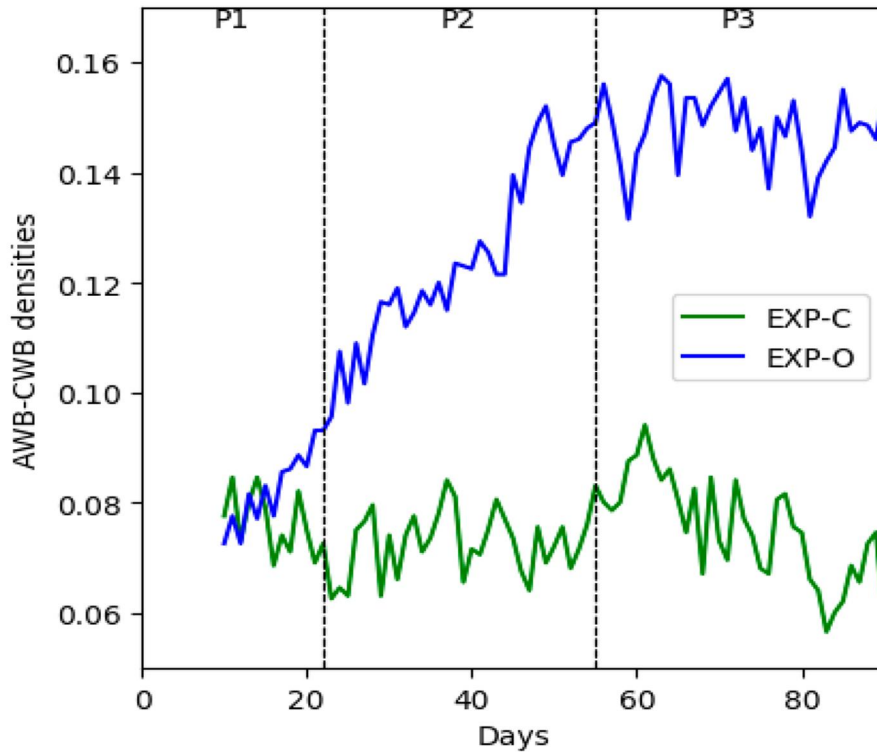


Figure 4.16. Anticyclonic wave breaking (AWB)-Cyclonic wave breaking (CWB) densities in time in EXP-C (green) and EXP-O (blue), respectively. All data displayed are the 11-days running mean of all 100 ensembles in

each day. AWB and CWB events are computed following Strong and Magnusdottir (2008). See text for more details.

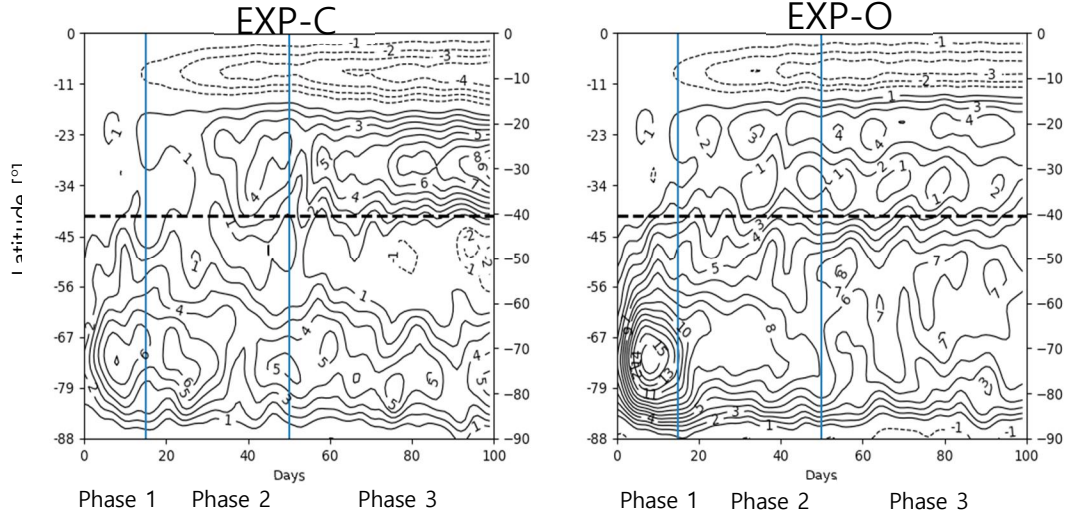


Figure 4.17. Zonal and ensemble-mean transient responses of Eady growth rate ($\sigma = 0.31g/(aN\Theta_0)(\partial\bar{\theta}/\partial\phi)$, unit: 10^7 s^{-1}) as a function of latitude and time in (left) EXP-C and (right) EXP-O.

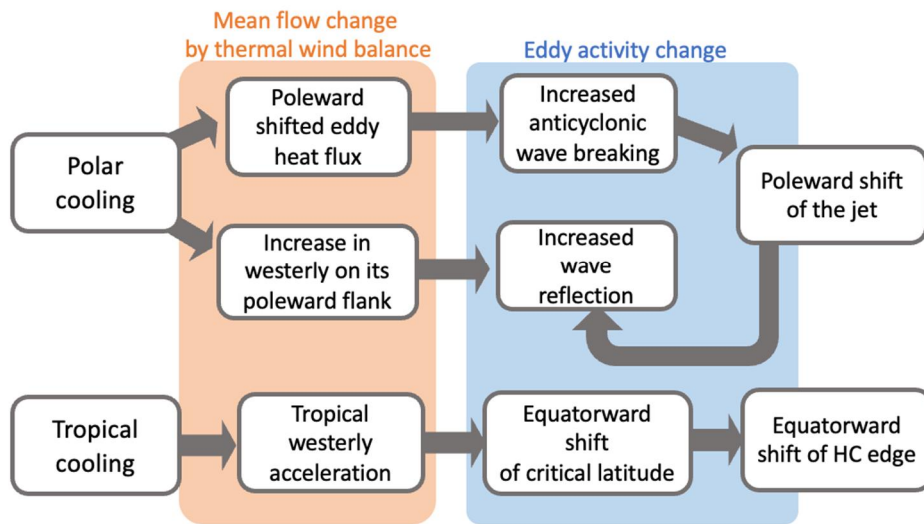


Figure 4.18. Schematic diagram for the possible dynamical mechanisms of the opposing HC–jet shifts under the global cooling condition. See the text for the details.

Chapter 5. The opposing HC–jet change in the LGM scenario: using a full GCM

5.1 Motivation

By using a dry-dynamical core, section 3.4 and Chapter 4 provide the condition for the *opposing* HC–jet change: a stronger polar cooling near the surface than tropical cooling in the upper troposphere. To be more specific, the jet shift in LGM simulations is simply explained by the cooling tug-of-war competitions: an equatorward shift in response to tropical cooling and a poleward shift in response to polar surface cooling; and the winner in the LGM is a polar cooling. On the other hand, the HC edge is less sensitive to the polar cooling. Such sensitivity changes of circulations can be understood in terms of Rossby wave dynamics in Chapter 4. Although Chapter 4 suggests the importance of polar cooling in the opposing HC–jet changes in the LGM condition, the dynamical processes proposed in Chapter 4 are based upon dry dynamics. However, it is still questionable that such a dynamical process works well in the comprehensive models. What is the cause of the enhanced polar cooling in the LGM? Does the enhanced polar cooling indeed induce the opposing circulation changes?

Many studies took lots of effort to address the above questions. One of the important causes of the strong polar cooling in the LGM period is the increased sea ice concentration and the ice sheet over the Antarctic in the LGM period, affecting the high-latitude atmospheric changes (Chavailiz 2013; Kim et al. 2017). Kim et al. (2017) especially demonstrated that the increased sea ice fraction in the LGM contributes to 60 % of the poleward shift of the jet in the SH. Furthermore, with the complicated wave dynamics in the tropics, the change of easterly winds in the tropics (e.g., Lee 1999) could have an impact on the Hadley circulation dynamics, possibly influencing the HC–jet relationship.

For instance, Kim et al. (2003) pointed out the importance of oceanic circulation in LGM conditions. Among the factors, sea-ice concentration (SIC) is particularly important in the Last Glacial Maximum (LGM) conditions. The SIC largely influences the jet shift, especially in the SH (e.g., Chavaillaz et al. 2013; Kim et al. 2017; Sime et al. 2016). Sime et al. (2016) presented that the changes in surface heat fluxes, due to sea ice changes, can have a very large impact on the jet, particularly when they are located close to the jet latitude. Lee et al. (2011) investigated the effect that wind jet shifts have on ocean circulation during the LGM using numerical models.

As such, the impacts of physical processes also deserve further analyses to deeply understand the broken HC–jet relationship. In this study, we revisit whether the dynamic process works with physics using a more comprehensive model. The goal of the present chapter is to explore the dynamic mechanism of the opposing HC–jet change in the LGM scenario, which is discussed in Chapter 4, in the atmospheric-ocean coupled model as well as a simplified dynamic core. To this end, we investigate the HC edge and jet latitude shift in the opposite way to each other in LGM scenarios in the model. To compare to the coherent case without sea ice change, the LGM but without sea ice scenario is also compared.

This chapter is organized as follows. Section 5.2 provides the zonal-mean circulation changes. The associated eddy activities are shown in section 5.3. Model information and the experiments used in this study are described in section 2.3.

5. 2 Zonal-mean atmospheric change

The zonal-mean atmospheric differences in the LowSIC and HighSIC are displayed in Fig. 5.1. The temperature and circulation differences in LowSIC are illustrated in the bottom row of Fig. 5.1. The zonal-mean temperature structure a little bit differs from the responses

to the full LGM conditions as shown in the upper row of Fig. 5.1. From this decreased Antarctic cooling, the zonal wind change is distinguishable from the LowSIC (Fig. 5.1(b)). The zonal wind change shows a rather equatorward-shifted jet, which is pronounced by the deceleration on the poleward flank and the acceleration of the equatorward flank of the jet, which is quite the opposite to the results from the LGM response. This is the opposite of the robust poleward shifted jet shown in HighSIC (Figs. 5.1e, f). On the other hand, the zonal wind change in the tropics is persistent, presenting anomalous easterlies in the subtropics (30°S to 15°S) and westerlies in the deep tropics (15°S to the equator) in the upper troposphere. By looking at the mean meridional circulation change, this is also shown (Fig. 5.1(f)). The sign of mean meridional circulation does not change much with the anomalous clockwise circulation with a greater magnitude compared to Fig. 5.1(f).

A comparison of the upper and bottom rows of Fig. 5.1 demonstrates that the SIC could play a critical role in modulating the HC-jet change relationship. The HighSIC well captures the responses of temperature, zonal wind, and mean meridional circulation in the PMIP3 models (compare the bottom line of Fig. 5.1 to Fig. 2.1). The leftmost figure in Fig. 5.1 presents the polar cooling extended up to 700 hPa in the

vertical and horizontally 60°S over the Antarctic. This is much greater than the tropical cooling in the upper troposphere about 30°S to the equator. The zonal wind structure change is characterized by the acceleration of the westerly wind on the poleward flank of the PI jet (~45°S) and the deceleration on the equatorward flank, indicating the poleward shifted polar-front jet in the LGM with respect to the PI scenarios, as consistent with the literature (Kim et al. 2017; Kim and Son 2020). The mean meridional circulation also presents the anomalous clockwise circulation on the tropics around 30 ° S, implying the equatorward shifted HC edge in the LGM compared to the PI climate states.

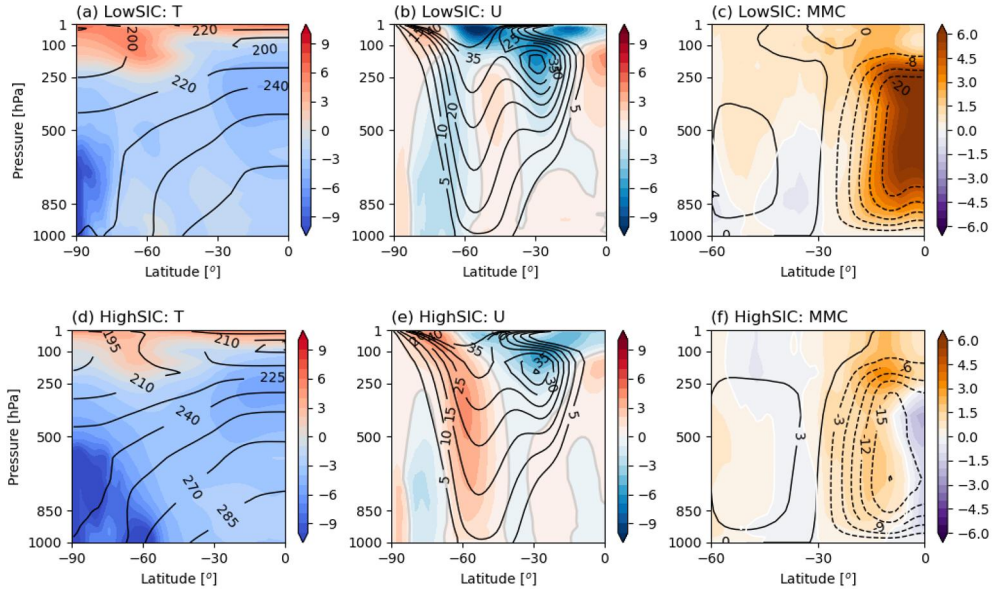


Figure 5.1. The zonal-mean temperature (unit: K), zonal wind (unit: m s^{-1}), and mean meridional circulation (MMC; unit: $10^{10} \text{ kg s}^{-1}$) responses (top) in the LowSIC and (bottom) in the HighSIC. Note that the latitudinal range in (c, f) is different from others.

Fig. 5.2 exhibits the clear separation of HC–jet relationship changes in the LowSIC and HighSIC. The HC edge and the jet latitude are quantified as in the same manner in Chapter 3. While the LGM presents the opposing HC–jet changes, or a poleward shift of the jet latitude but an equatorward shift of the HC edge, compared to the PI experiment, it shows their coherent equatorward shifts compared to the LowSIC. The magnitude of the shifts of the HC edge and jet latitude is comparable to the opposing/coherent HC–jet changes in PMIP3 models (compare to Fig. 2.3b). Figure 5.2a exhibits the temperature changes in LowSIC and HighSIC. The temperature changes, a greater polar cooling ($q_{\text{pole}} = \sim 9.3 \text{ K}$

area-averaged over the 75°S to 55°S at 925 hPa) than the tropical cooling ($q_{\text{trop}} = \sim 5$ K area-averaged over the 30°S to 0°S at 250 hPa) in the LGM experiment here, also confirms the findings of Kim and Son (2020) and the results of Chapter 4 which argue the importance of polar cooling in the opposing HC-jet change.

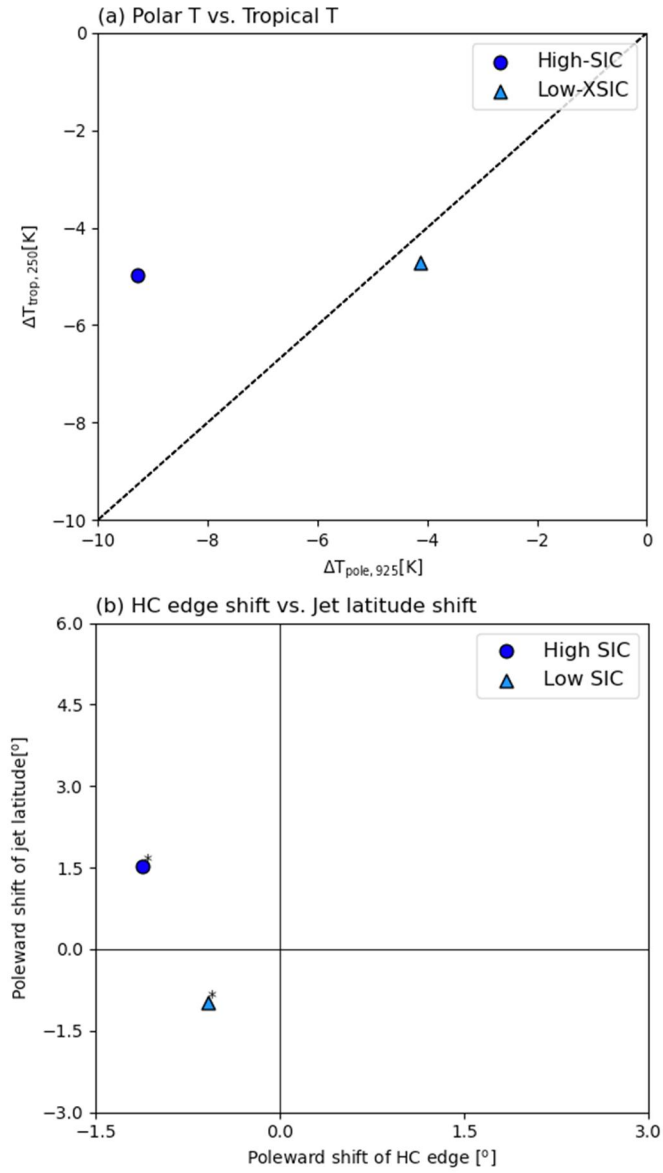


Figure 5.2. (a) The polar and tropical temperature changes in High-SIC (blue circle) and Low-SIC (skyblue triangle). (b) The HC edge shifts vs. jet latitude shifts High-SIC (blue circle) and Low-SIC (skyblue triangle).

5.3 The eddy activity change

To investigate the dynamics in such opposing and coherent cases, this section provides the eddy activities in these two sets of experiments. The eddy momentum fluxes (EMF), and eddy heat fluxes (EHF) are analyzed based on the daily-mean data.

The EMF divergences in LowSIC and HighSIC are shown in Fig. 5.3. The overall structure of EMF convergence/divergence, contoured in Fig. 5.3, is pronounced by the maximum convergence in the midlatitude, which is generally linked to the low-level temperature gradient maximum, considered as a stirring latitude. The EMF divergence occurs surrounding the convergence. The divergence of EMF is in the high-latitudes and the subtropics, which are related to wave dissipation.

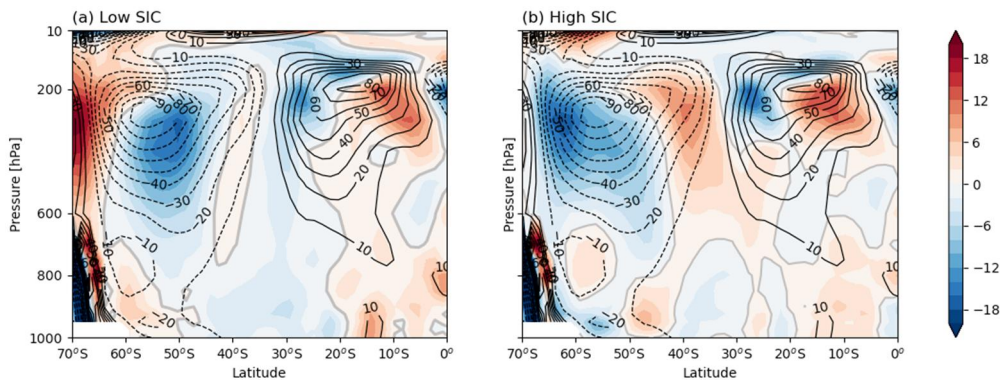


Figure 5.3. Eddy momentum flux divergence differences (shading, unit: 10^{-5} m s^{-2}) in (a) LowSIC and (b) in HighSIC. The contours eddy momentum flux divergence in the LGM scenario.

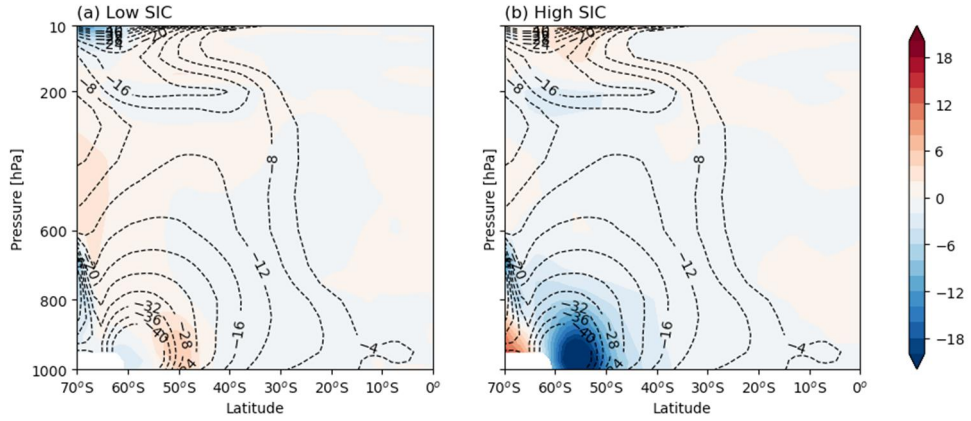


Figure 5. 4. Eddy heat flux differences(unit: K m s^{-1}) in (a) LowSIC and (b) in HighSIC (shading). The contours are eddy heat fluxes in LGM scenario. The negative eddy heat flux indicates the poleward (southward) eddy heat flux.

The EMF responses in the LowSIC and HighSIC are shown in Fig. 5.3. The biggest difference between the two experiments is found in the midlatitudes. The midlatitude EMF convergence in HighSIC provides its equatorward shift, which contrasts with the poleward shifts shown in LowSIC. The HighSIC response is pronounced by the poleward shift of EMF convergence and the equatorward shift of EMF convergence. There is another anomalous divergence in the higher latitude than 70°S which seems to be related to the increased height by the ice sheet over the Antarctic. However, this anomalous divergence does not effectively affect the shifts of the EMF convergence in the midlatitude and the associated jet latitude. We therefore do not focus on these EMF changes in the high latitudes in this section.

According to the mechanism introduced in Chapter 4, this might be related to the change in EHF in the lower troposphere (Figs 5.4). Figure 5.4 supports this speculation by presenting an extinct equatorward shift in the LowSIC but the poleward shifted EHF in the HighSIC. While the midlatitude change is the opposite to each other, the subtropical EMF divergence change is similar in both LowSIC and HighSIC experiments. This is also well found in Fig. 5.5 where the EHF at 850 hPa is focused on. This similar response in the subtropics well coincides with the equatorward shifted HC edge in the subtropics, which could be associated with the tropical cooling.

EHF at the 850 hPa changes in Fig. 5.5 are further investigated by decomposing by zonal wave numbers (k) (Fig. 5.6). The EHF850 contributions by long waves with zonal wavenumber k of 1 to 5 (dashed) and short waves with zonal wavenumber k of 6 and larger (dotted line). Figure 5.6 clearly reveals that the enhancement of EHF in the high latitudes is largely driven by long waves rather than short waves. This result supports *mechanism 1* proposed in section 4.1 whereby the increased EHF on its poleward flank leads to more unstable long waves (Riviere 2011), potentially breaking anticyclonically and pushing the jet poleward.

The results in the present section confirm that the broadened EMF convergence zone is characteristic of the opposing HC-jet change. The EMF convergence in LGM-SIC is consistent with the findings in Chapter 4, coinciding with the EMF changes in the opposing case in dynamic-core experiments, or the EXP-O. On the contrary, the EMF convergence change in the LowSIC does not resemble the change in HighSIC. Instead, the EMF in the upper troposphere in LowSIC presents the equatorward shifts of the EMF convergence in the midlatitude and EMF divergence in the subtropics, which is corresponding to that in the coherent case, i.e., EXP-C, in Chapter 4.

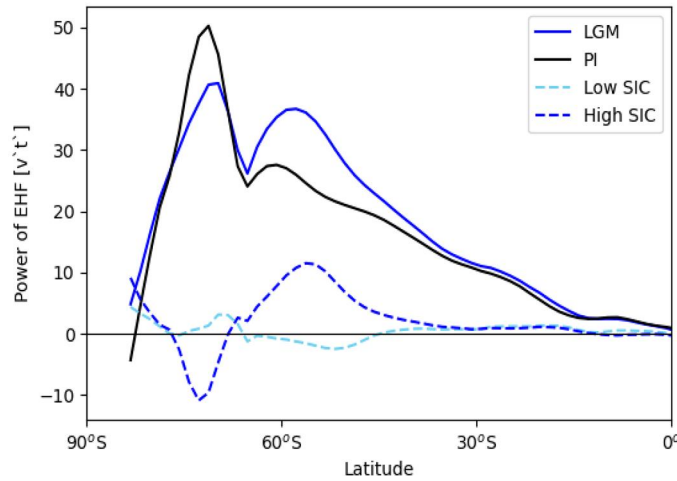


Figure 5. 5. (a) Eddy heat fluxes at 850 hPa for all waves in LGM (solid blue), PI (solid black), LowSIC (dotted), and HighSIC (dashed) experiments (unit: $\text{m s}^{-1} \text{K}$).

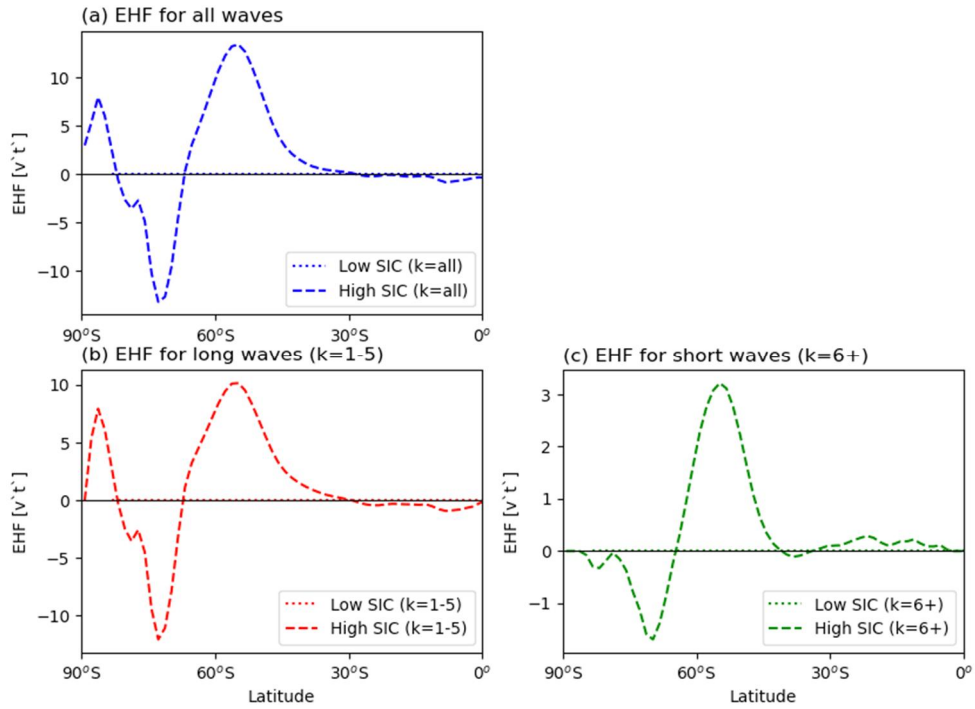


Figure 5.6. (a) Eddy heat fluxes at 850 hPa for all waves in LGM (solid blue), PI (solid black), LowSIC (dotted), and HighSIC (dashed) experiments (unit: $\text{m s}^{-1} \text{K}$). (b, c) Same as (a) but (b) for long waves with a range of zonal wavenumber k from 1 to 5, and (c) for short waves with a range of zonal wavenumber from 6 and larger, respectively. Note that the positive sign of the y axis indicates the poleward shift of the EHF in the SH.

Chapter 6. Conclusions

This study examines the HC–jet relationship in the SH from colder climates, in the context of the zonal mean. A coherent poleward displacement of the HC edge and jet latitude has been observed in the SH during the last few decades. This change is further projected to continue in the future, indicating coherent tropical and extratropical zonal-mean circulation changes from the present and a warmer climate. However, here we showed that such a systematic change in the zonal-mean circulation does not hold in a cold climate. This is successfully reproduced in a simplified GCM. Under global cooling-like simulations, when tropical cooling is greater than polar cooling, the HC edge and jet latitude shift equatorward together but they move in an opposite direction to each other with enhanced polar cooling. The HC-edge and jet-latitude changes are investigated with varying magnitudes of tropical cooling in the upper troposphere and polar cooling near the surface in the model. The opposing circulation shift occurs primarily due to the high sensitivity of the jet-latitude shift to polar cooling, compared to that of the HC-edge shift. When tropical cooling is dominant, both the HC edge and jet latitude shift equatorward. In contrast, the opposing HC–jet shift, i.e., a poleward shift of jet latitude and an equatorward shift of HC edge, is found when the polar cooling is much stronger than the tropical

cooling. This result confirms that the opposing HC–jet shift in the LGM, found in KS20, results from a dominant role of the lower-level baroclinicity change against the upper-level changes (e.g., Barnes and Screen 2015).

Our analysis suggests the following mechanism for the opposing HC–jet shifts under a cold climate. The polar cooling causes the HC edge and jet latitude to shift poleward as the baroclinic zone expands poleward. It accompanies the poleward shifts of the maximum eddy momentum flux convergence in the midlatitudes and the divergence in the tropics. The former change is much larger than the latter, as fast waves are effectively modulated by baroclinicity in the midlatitudes. As the jet shifts poleward, the upper-tropospheric zonal wind increases on its poleward flank, increasing wave reflection. Such an increased wave reflection again contributes to the poleward shift of the jet, leading to increased poleward eddy momentum flux (e.g., Lorenz 2014). Meanwhile, the HC edge is only weakly influenced by the polar cooling-induced baroclinicity change. It remains on the equatorward side of the control HC in all cooling experiments. This is partly due to the tropical cooling-induced equatorward shift of the subtropical critical latitude, whereby slow waves break. This critical latitude change is partly driven by the tropical cooling-induced axisymmetric circulation.

The above possible mechanisms for the opposing HC–jet shifts in an LGM-like climate in the equilibrium state. To fully understand the mechanisms of such circulation changes, we identify the eddy activity and the zonal-mean state change in response to weak polar cooling and strong polar cooling, respectively. The spin-up experiments improve our understanding of the opposing HC–jet shift, highlighting the role of stronger polar cooling than tropical cooling. The enhancement of the low-level baroclinicity due to strong polar cooling can induce long waves being unstable, further affecting the increase in anticyclonic wave-breaking events. This could contribute to the poleward shift of the jet.

Notwithstanding the limitations of the idealized model simulations, the dry dynamical core GCM used in this study succeeded in qualitatively reproducing the opposing HC–jet shifts seen in the PMIP3 simulations. To better understand such circulation changes, we revisit the impact of polar cooling in the LGM simulation by using the coupled model experiments in which the jet is influenced by and impacts the ocean and sea ice conditions in the LGM. We found that the opposing circulation change due to strong polar cooling is well reproduced in the atmospheric-coupled climate models.

We first examine the relationship between the HC edge and eddy-driven jet latitude in the SH from cold to warm climates (Chapter 3). All

analyses are conducted by comparing the LGM and ECP4.5 scenario simulations against the PI simulations archived for PMIP3 and CMIP5. Consistent with previous studies, the annual-mean HC edge and jet latitude move together toward higher latitudes under the ECP4.5 condition. Such a systematic change, however, does not appear in the LGM simulations. While the annual-mean HC edge shifts equatorward in all LGM simulations, the annual-mean jet shifts either equatorward or poleward depending on the models. Only three out of nine models show a coherent equatorward shift of the annual-mean HC edge and jet latitude from the PI to LGM scenarios. Other models show no relationship or even opposite jet changes from those of the HC edge. These nonsystematic changes are mainly caused by the inter-model differences in the jet latitude changes in austral winter (JJA). The ratio of the jet latitude change to the HC edge change under the LGM condition is independent of interannual HC-jet co-variability, indicating that the decoupled circulation changes in LGM JJA cannot be simply explained by intrinsic HC-jet dynamics.

Chapter 3 also includes the HC-edge and jet-latitude changes in the simplified model in an equilibrium state. In global cooling-like experiments, when tropical cooling is solely imposed, the HC edge and jet latitude shift equatorward together. Oppositely, they shift poleward

together when polar-surface cooling is imposed. Therefore, the opposing HC–jet change is found when tropical cooling is weak and the high-latitude cooling is strong: strong polar cooling tends to shift the jet latitude poleward against the equatorward-shifted HC edge. When polar warming is much stronger than tropical warming, the HC edge continues to shift poleward but the jet shifts equatorward rather poleward. This is mostly driven by the higher sensitivity of the jet latitude, especially to the polar cooling. While the HC edge is controlled by the tropical temperature-change induced equator-to-pole temperature gradient in the upper level, the jet-latitude change is more related to the equator-to-pole temperature gradient in the lower-level troposphere which is largely influenced by polar surface temperature. Therefore, unlike the competitive roles of tropical/polar temperature on the jet latitude, the HC edge is largely influenced by tropical temperature and associated with an equator-to-pole temperature gradient in the upper-level troposphere. This is consistent with literature that presents the importance of subtropical static stability (e.g., Son et al. 2018b).

The opposing HC–jet change, especially in cooling experiments with a poleward-shifted jet and an equatorward-shifted HC edge as shown in Chapter 3, is dynamically analyzed in Chapter 4. Both the HC edge and jet latitude shift equatorward in response to the tropical

cooling. When the polar cooling is additionally applied, they move poleward as the baroclinic zone is expanded poleward. The maximum latitude of eddy heat flux shifts poleward with the increasing polar cooling. This wave source change causes a poleward shift of the maximum eddy momentum flux convergence in midlatitudes and its zero-crossing latitude in the subtropics. The former change is much larger than the latter change as the fast waves are effectively modulated by the baroclinicity in high latitudes. When the polar cooling is sufficiently strong, the jet latitude is located on the poleward side of the jet in the control run. In such a case, the high-latitude critical latitude is replaced by the turning latitude. The HC edge is only weakly influenced by the polar cooling-induced baroclinicity change. It remains on the equatorward side of the control HC in all cooling experiments. This is partly due to the tropical cooling-induced critical latitude change. Even under the strongest polar cooling, the critical latitude appears on the equatorward side of that in the control run. This makes the slow waves break in the deep tropics. Although further analyses are needed, the maintenance of the critical latitude can be partly attributed to the axisymmetric (2-dimensional) circulation change by the tropical cooling.

To investigate the proposed mechanism of the opposing HC–jet changes in the LGM climate, we examine the coherent and opposing cases,

EXP-C and EXP-O, respectively, as the transient experiments using an idealized model in Chapter 4. By comparing the weak and strong polar cooling and the same tropical cooling, we found that the polar cooling-induced lower-level baroclinicity change plays an important role in determining the jet latitude, by increasing the AWB events. To be more specific, the enhanced polar cooling results in the increase of the lower level baroclinicity in Phase 1, driving long waves to become more unstable compared to short waves. The long waves break anticyclonically, pushing the jet poleward in Phase 2, particularly in EXP-O. This could contribute to a poleward shift of the jet latitude in EXP-O, which is identical to COMB-C in Chapters 3 and 4, giving us a dynamical interpretation of the role of altered wave source regions in opposing HC and jet under the global cooling condition (*Mechanism 1; see section 4.1 for details*). To confirm the proposed mechanism of the opposing HC–jet changes in the LGM climate, EXP-C and EXP-O are further examined as the transient experiments in Chapter 4. By comparing the weak and strong polar cooling and the same tropical cooling, we found that the polar cooling-induced lower-level baroclinicity change plays an important role in determining the jet latitude, by increasing the AWB events. To be more specific, the enhanced polar cooling results in the increase of the lower level baroclinicity in Phase 1, driving long waves to

become more unstable compared to short waves. The long waves break anticyclonically, pushing the jet poleward in Phase 2, particularly in EXP-O. This could contribute to a poleward shift of the jet latitude in EXP-O, which is identical to COMB-C in Chapters 3 and 4, giving us a dynamical interpretation of the role of altered wave source regions in opposing HC and jet under the global cooling condition.

Chapter 5 examines dynamics of the opposing HC–jet change by using a more realistic model. In particular, the increase in sea ice concentration over the Antarctic could lead to a poleward increase of low-level baroclinicity, activating long waves. This results in the poleward shift of the EMF convergence and an equatorward EMF divergence in the upper level. Although these processes are based on the simplified GCM study, the results from this chapter suggest that the mechanisms are possibly acceptable in a more realistic model.

Although the results from Chapter 5 of this study reveal that sea-ice concentrations play an important role in modulating the opposing HC–jet changes, there are still several issues to circumvent. For instance, there is the absence of stationary waves. The idealized model used in Chapters 3 and 4 does not include any topography or land-sea contrast. This restricts the generation of stationary waves. In general, this is conceptually accepted for the dynamic study focused on the southern

hemisphere. However, the situation could differ for the LGM conditions which include an extremely large amount of the ice sheet in the Antarctic. As well as influencing the polar cooling, this ice sheet plays a role in mediating the stationary wave in the atmosphere.

Chapter 7. Further work: global warming-like simulations

It should also be emphasized that the opposing HC-jet change is not a confined phenomenon that occurs only under global cooling-like conditions but also under global warming-like conditions. Can the opposing HC-jet change appear in global warming scenarios? In the present and near-future climates, tropical warming is dominant, so it satisfies the conditions of opposing HC-jet change. However, the results of the present study imply that if Arctic warming is further enhanced, the HC-jet relationship can be broken in a future climate. This highlights that the opposing HC-jet change is further needed to be studied under global warming scenarios.

Are the opposing HC-jet changes unique only in a cold climate? To address this question, a parameter sweep study described in section 3.4.4 is repeated with warming forcings, i.e., $q_{\text{trop}} \geq 0$ and $q_{\text{pole}} \geq 0$ (Fig. 7.1).

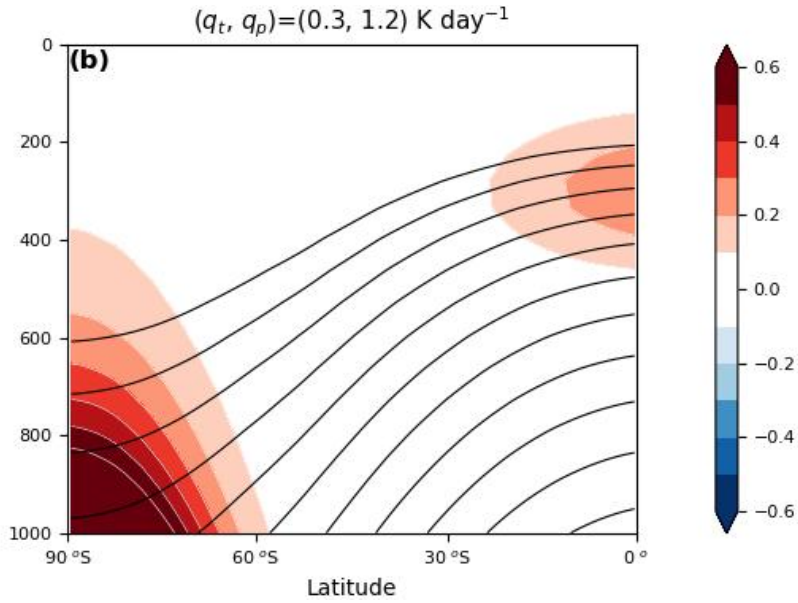


Figure 7.1. The equilibrium temperature profile (black contours) and the additional tropical, q_{trop} , and polar thermal forcings, q_{pole} , for heating experiments. The additional forcings are introduced to mimic global-warming-like climate states, respectively. The contour intervals are 20 K, and shading intervals are 0.2 K day^{-1} .

Figure 7.2 illustrates the responses of the time mean zonal-mean temperature, zonal wind, and mass stream function for warming experiments with the same amplitude of tropical/polar/multiple thermal forcings as shown in Fig. 2.1. As seen in Fig. 7.2a, warming in the tropical upper troposphere takes place from the equator to 40°S with a compensating cooling in the polar upper troposphere. This meridional temperature dipole pattern in the upper troposphere is presumably related to the strengthened Brewer-Dobson circulation (Kim and Son 2015). When polar forcing is imposed only, the temperature response to

polar warming is quite similar to the response to polar cooling with a comparable amplitude but with an opposite sign.

The opposite responses of circulation to tropical/polar forcings are found in warming experiments (Figs. 7.2d, g, e, and h). Tropical warming tends to drive the stronger and poleward-shifted HC edge and jet latitude (Figs. 7.2d and g), while polar warming leads to the equatorward shifts of the HC edge and jet latitude (Figs. 7.2e and h). The multi-forcing experiment, shown in the third column of Fig. 7.2, exhibits the poleward-shifted HC and the weakened and poleward-shifted zonal wind (Figs. 7.2c, f, and i). The results of Figs. 7.2f and 7.2i are largely in agreement with earlier studies (e.g., Butler et al. 2010; Yuval and Kaspi 2016).

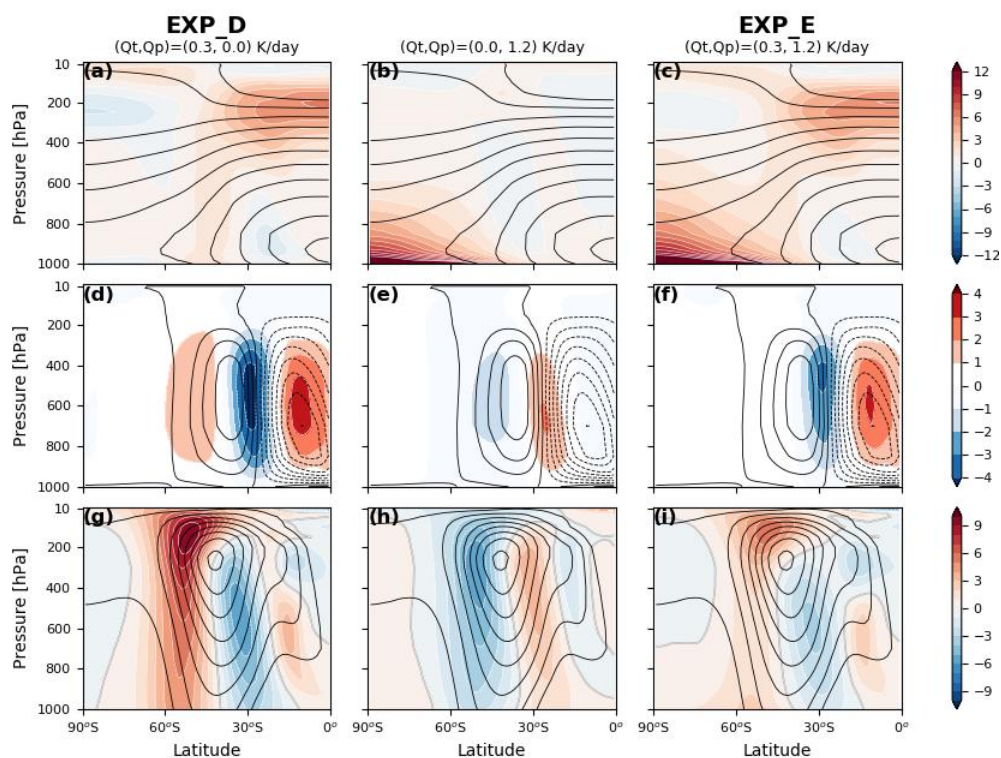


Figure 7.2. Same as Fig. 3.10 but from heating experiments $(q_{\text{trop}}, q_{\text{pole}}) = (0.3, 0.0)$, $(0.0, 1.2)$, and $(0.3, 1.2)$ K day⁻¹.

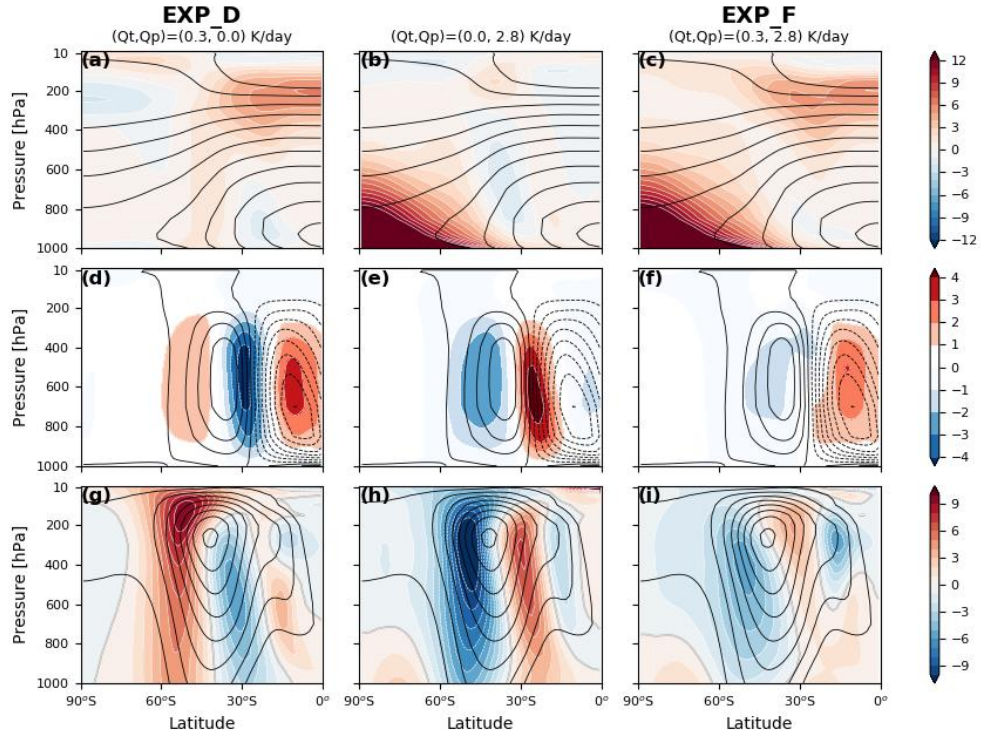


Figure 7.3. Same as Fig. 7.2 but with a stronger polar warming of $(q_{\text{trop}}, q_{\text{pole}}) = (-0.3, 0.0)$, $(0.0, 2.8)$, and $(0.3, 2.8)$ K day⁻¹. The left column is identical to the one in Fig. 7.2 and is shown here for comparison purpose.

Unlike the coherent shifts of the HC and jet, the warming experiment with enhanced polar warming yields the shifts of the HC and jet in the opposite direction to each other (right column of Fig. 7.3). In particular, the zonal wind with 2.8 K day⁻¹ of polar warming presents a different response to the experiment with $(q_{\text{trop}}, q_{\text{pole}}) = (0.3, 1.2)$ K day⁻¹, while the mean meridional circulation response (Figs. 7.3f) is quite similar to the response from weak polar warming experiment (Figs. 7.3f). The HC edge seems to shift further poleward in the upper troposphere compared to the mean meridional circulation change in the lower level.

It seems that the responses of lower-level mean meridional circulation to the tropical and polar forcings are canceled out to each other (see Fig. 7.3i; compared to Figs. 7.2g, 7.2h). Overall results from warming experiments suggest that the opposing HC-jet change can occur not only in global cooling conditions but also in global warming conditions.

To test whether the opposing HC-jet change can occur even in global warming-like climate states, we repeated the parameter sweep study shown in section 3.4.4 but with $q_{\text{trop}} > 0$ and $q_{\text{pole}} > 0$. As summarized in Fig. 7.4a, the results are largely opposite to those of the LGM-like cooling experiments (Compare to Fig. 3.13a). In the tropical-warming-only experiments (bottom row in Fig. 7.4a), both the HC edge and jet latitude shift poleward as q_{trop} increases. They shift equatorward with increasing q_{pole} when polar warming is solely applied (first column). This result confirms the previous studies arguing the competing roles of the tropical and polar warmings in determining the jet latitude (e.g., Butler et al. 2010; Barnes and Screen 2015).

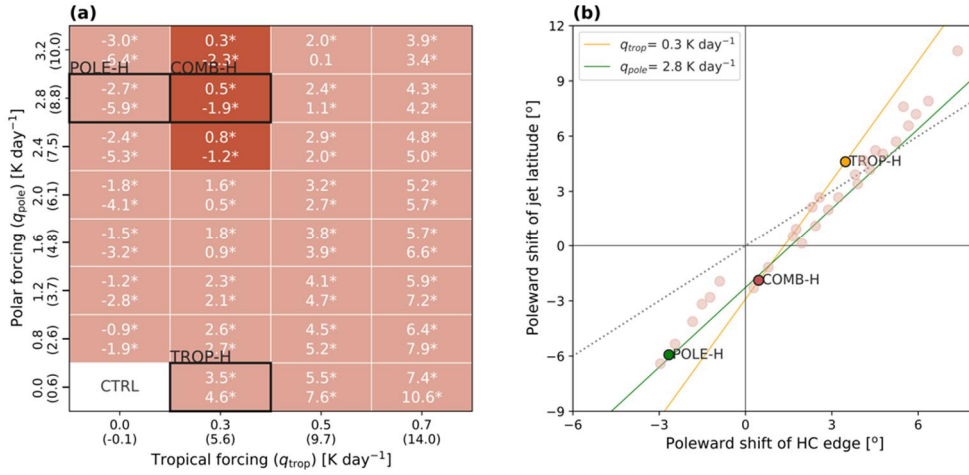


Figure 7.4. Same as Fig. 3.13 but for warming experiments. The experiments with opposing shifts of circulations, i.e., a poleward HC-edge shift and an equatorward jet-latitude shift, are denoted in dark red in (a). The three experiments, i.e., TROP-H, POLE-H, and COMB-H, are denoted with a black border. (b) The relationship between the HC-edge and jet-latitude changes in all experiments. The HC-jet change ratio to $q_{trop} = -0.3 K day^{-1}$ (orange) and $q_{pole} = -2.8 K day^{-1}$ (green) are denoted with colored lines. The one-to-one line is denoted with a dotted line in (b).

Compared with the cooling experiments (Fig. 7.4b), a stronger linearity emerges in the warming experiments. As the magnitude of tropical warming increases, the HC edge and jet latitude shift poleward with the rates of $10.2^{\circ}/(K day^{-1})$ and $14.3^{\circ}/(K day^{-1})$, respectively. They shift equatorward as polar warming increases at rates of $1.0^{\circ}/(K day^{-1})$ and $2.2^{\circ}/(K day^{-1})$, respectively. These results confirm the results of previous studies that have suggested competing roles of tropical and polar warmings in determining jet latitude (e.g., Butler et al. 2010; Barnes and Screen 2015). It is further found that the combined-warming

experiments are better explained by the linear correlation of tropical and polar forcings with a higher R^2 ($=0.99$) for both the HC edge and jet latitude than the cooling experiments. Indeed, the COMB-H experiment with $(q_{\text{trop}}, q_{\text{pole}}) = (0.3, 2.8)$ K day $^{-1}$ appears at the intersection of the regression lines of tropical-cooling and polar-cooling experiments (orange and green lines in Fig. 7.4b).

The circulation and eddy responses in the three reference warming experiments, indicated in Fig. 7.4, are further explored in Fig. 7.5. In short, the overall changes resemble those in cooling experiments with the sign opposed, including the phase-speed dependent eddy activity changes (Fig. 7.6). These results suggest that the opposing HC–jet shifts in global warming-like experiments can be largely explained by the same dynamical processes responsible for those in LGM-like experiments.

To identify the possible opposing changes in circulations in the future, global warming-like experiments are performed in this chapter. The opposing circulation shifts are also found in global warming-like experiments. A poleward shift of the HC edge and an equatorward shift of the jet latitude are observed when polar warming is sufficiently stronger than tropical warming. Overall processes that determine the opposing circulation shifts in the warming experiments are similar to

their counterparts in the cooling experiments but with a switched sign. This result suggests that the opposing HC-jet shifts are not unique in LGM-like climate states but can also occur in future climates if polar amplification is accelerated. This speculation has been partially confirmed by recent studies that proposed an equatorward shift of the eddy-driven jet in the Northern Hemisphere with projected Arctic amplification (e.g., Barnes and Polvani 2015; Coumou et al. 2018; Ronalds and Barnes 2019).

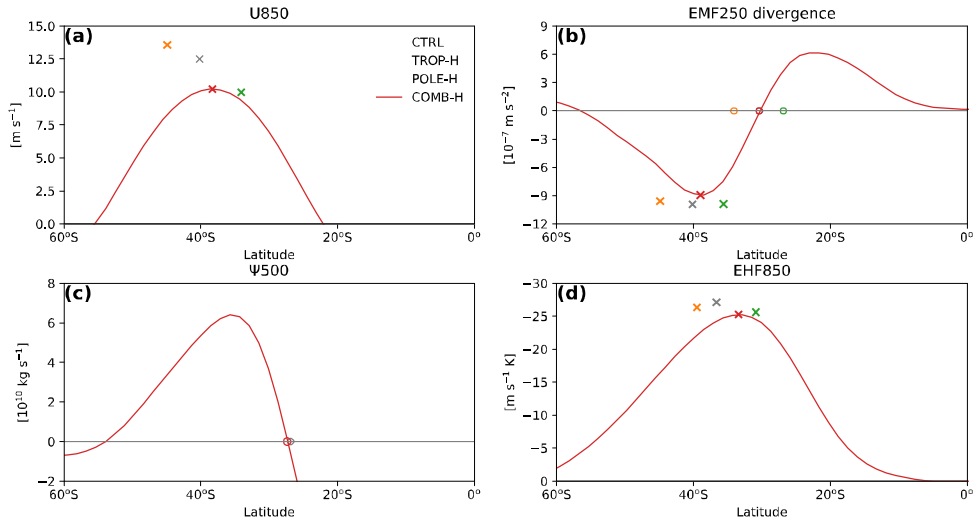


Figure 7.5. Same as Fig. 4.1 but for TROP-H (orange), POLE-H (green), and COMB-H (red). The maximum latitudes of U850, EMF250 convergence, and EHF850 are denoted with “X” in (a), (b), and (d), respectively. The zero-crossing latitudes for EMF250 divergence and Ψ500 are denoted with “O” in (b) and (c), respectively.

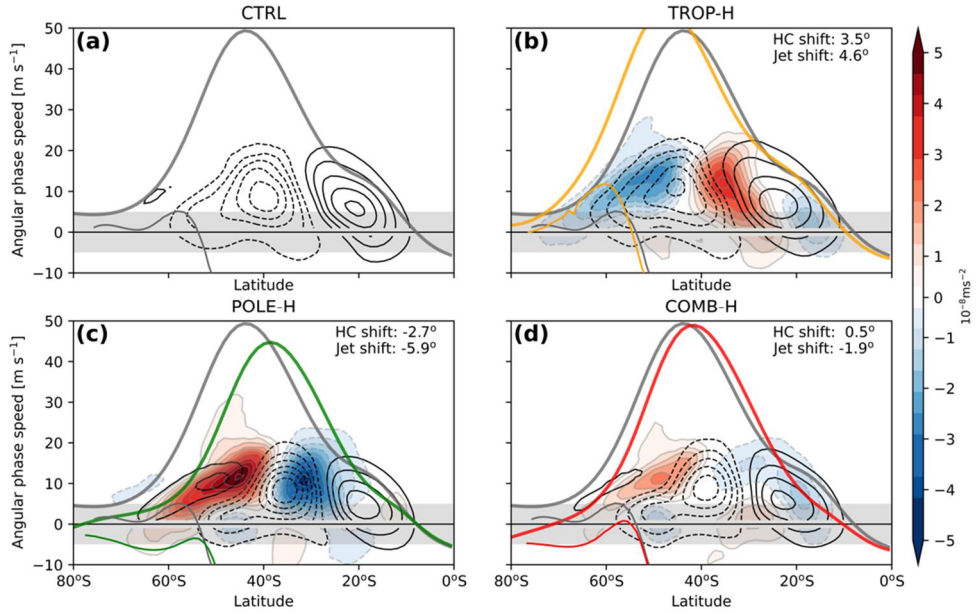


Figure 7.6. EMF250 divergence cospectra (10^{-8} m s^{-2} , contours) as a function of angular phase speed and latitude in (a) CTRL, (b) TROP-H, (c) POLE-H, and (d) COMB-H. (b–d) The differences in EMF divergence in each experiment from CTRL (e.g., TROP-H *minus* CTRL) are shaded, with anomalous divergence in blue and convergence in red. Contours are depicted from $-6 \times 10^{-8} \text{ m s}^{-1} \text{ day}^{-1}$ to $6 \times 10^{-8} \text{ m s}^{-1} \text{ day}^{-1}$ with intervals of $1 \times 10^{-8} \text{ m s}^{-1} \text{ day}^{-1}$, and the shading range is from $-5 \times 10^{-8} \text{ m s}^{-1} \text{ day}^{-1}$ to $5 \times 10^{-8} \text{ m s}^{-1} \text{ day}^{-1}$ with intervals of $0.4 \times 10^{-8} \text{ m s}^{-1} \text{ day}^{-1}$. Thick and thin curves indicate the critical latitude and the reflective latitude for zonal wavenumber 6, respectively, for CTRL (gray) and cooling experiments (colored). Gray shaded phase speed range of -5 to 5 m s^{-1} denotes a slow phase speed range.

References

- Adam, O., Grise, K. M., Staten, P., Simpson, I. R., Davis, S. M., Davis, N. A., Waugh, D. W., Birner, T., and A. Ming, 2018: The tropD software package (v1): standardized methods for calculating tropical-width diagnostics. *Geosci. Model Dev.*, **11**(10), 4339-4357.
- Barnes, E. A., and L. M. Polvani 2013: Response of the Midlatitude Jets, and of Their Variability, to Increased Greenhouse Gases in the CMIP5 Models. *J. Climate*, **26**, 7117-7135, doi:10.1175/JCLI-D-12-00536.1.
- , and D. W. J. Thompson, 2014: Comparing the roles of barotropic versus baroclinic feedbacks in the atmosphere's response to mechanical forcing. *J. Atmos. Sci.*, **71**, 177–194, <https://doi.org/10.1175/JAS-D-13-070.1>.
- , E. A., and J. A. Screen, 2015: The impact of Arctic warming on the midlatitude jet-stream: Can it? Has it? Will it?, *Wiley Interdisciplinary Reviews: Climate Change*, **6**(3), 277–286.
- Bordoni, S., and T. Schneider 2015: Regime transitions of steady and time-dependent Hadley circulations: Comparison of axisymmetric and eddy-permitting simulations. *J. Atmos. Sci.*, **67**(5), 1643-1654.
- Braconnot, P., S. P. Harrison, M. Kageyama, P. J. Bartlein, V. Masson-Delmotte, A. Abe-Ouchi, B. Otto-Bliesner, and Y. Zhao, 2012: Evaluation of climate models using paleoclimatic data. *Nat. Climate Change*, **2**, 417–424, <https://doi.org/10.1038/nclimate1456>.
- Butler, A. H., D. W. Thompson, and R. Heikes 2010: The steady-state atmospheric circulation response to climate change-like thermal forcings in a simple general circulation model. *J. Climate*, **23**(13), 3474–3496.
- Caballero, R. 2007: Role of eddies in the interannual variability of Hadley cell strength. *Geophys. Res. Lett.*, **34**(22).
- Ceppi, P., and D.L. Hartmann, 2013: On the speed of the eddy-driven jet and the width of the Hadley cell in the Southern hemisphere., *J. Climate*, **26**, 3450–3465.
- Chavaillaz, Y., F. Codron, and M. Kageyama, 2013: Southern westerlies in LGM and future (RCP4.5) climates. *Clim. Past*, **9**, 517–524, doi:10.5194/cp-9-517-2013.
- Chemke, R., and L. M., Polvani, 2019: Exploiting the abrupt 4× CO₂ scenario to elucidate tropical expansion mechanisms. *J. Climate*, **32**(3), 859-875.

- Chen, G. and I. Held, 2007: Phase speed spectra and the recent poleward shift of the Southern Hemisphere surface westerlies. *Geophys. Res. Lett.*, **34**, L21805, doi:10.1029/2007GL031200.
- , Lu, J., and D. W. Frierson, 2008: Phase speed spectra and the latitude of surface westerlies: Interannual variability and global warming trend. *J. Climate*, **21**, 5942–5959.
- Choi, J., S.-W. Son, J. Lu, and S. K. Min, 2014: Further observational evidence of Hadley cell widening in the Southern Hemisphere. *Geophys. Res. Lett.*, **41**(7), 2590–2597.
- Choi, J., S.-W. Son, and R. Park 2019: Aerosol versus greenhouse gas impacts on Southern Hemisphere general circulation changes, *Clim. Dynam.*, **52**, 4127–4142, <https://doi.org/10.1007/s00382-018-4370-5>.
- Coumou, D., Di Capua, G., Vavrus, S., Wang, L., and Wang, S., 2018: The influence of Arctic amplification on mid-latitude summer circulation. *Nat. Comms.*, **9**(1), 1-12.
- D’Agostino, R. P. Lionello, O. Adam, and T. Schneider 2017: Factors controlling Hadley circulation changes from the Last Glacial Maximum to the end of the 21st century, *Geophys. Res. Lett.*, **44**, 8585–8591, doi:10.1002/2017GL074533.
- Davis, N. A., and T. Birner, 2019: Eddy influences on the Hadley circulation. *J. Adv. Model Earth Syst.*, **11**, 1563–1581. <https://doi.org/10.1029/2018MS001554>.
- Davis, N. A., D. J. Seidel, T. Birner, S. M. Davis, and S. Tilmes, 2016: Changes in the width of the tropical belt due to simple radiative forcing changes in the GeoMIP simulations, *Atmos. Chem. Phys.*, **16**, 10083–10095.
- Davis, S. M., K. H. Rosenlof, 2012: A multidagnostic intercomparison of tropical-width time series using reanalyses and satellite observations. *J. Climate*, **25**(4), 1061-1078.
- Denton, G. H., Anderson R. F., Toggweiler, J. R., Edwards, R. L., Schaefer, J. M., and Putnam, A. E., 2010: The Last Glacial Termination, *Science*, **328**(5986), 1652–1656.
- Edmon Jr, H. J., B. J. Hoskins, and M. E. McIntyre, 1980: Eliassen-Palm cross sections for the troposphere. *J. Atmos. Sci.*, **37**(12), 2600-2616.

- Fyfe, J.C., and O. A. Saenko, 2006: Simulated changes in the extratropical Southern Hemisphere winds and currents. *Geophys. Res. Lett.*, **33**(6).
- Gerber P. E., and S.-W. Son, 2014: Quantifying the summertime response of the Austral jet stream and Hadley cell to stratospheric ozone and greenhouse gases. *J. Climate*, **27**, 5538–5559, doi: 10.1175/JCLI-D-13-00539.1
- Grise, K. M., and L. M. Polvani, 2016: Is climate sensitivity related to dynamical sensitivity?. *J. Geophys. Res. Atmos.*, **121**, 5159–5176.
- _____, S. M. Davis, I.R. Simpson, D. W. Waugh, Q. Fu, R. J. Allen, K. H. Rosenlof, C. C. Ummenhofer, K. B. Karneuskas, A. C. Maycock, and X. W. Quan, 2019: Recent tropical expansion: Natural variability or forced response?. *J. Climate*, **32**(5), 1551–1571.
- _____, and _____, 2020: Hadley cell expansion in CMIP6 models. *Atmos. Chem. Phys.*, **20**(9), 5249–5268.
- Harnik, N., and R. S. Lindzen, 2001: The effect of reflecting surfaces on the vertical structure and variability of stratospheric planetary waves. *J. Atmos. Sci.*, **58**(19), 2872–2894.
- Harrison, S. P., and Coauthors 2015: Evaluation of CMIP5 palaeo-simulations to improve climate projections. *Nat. Clim. Change*, **5**(8), 735–743.
- Held, I. M., and A. Y. Hou, 1980: Nonlinear axially symmetric circulations in a nearly inviscid atmosphere. *J. Atmos. Sci.*, **37**(3), 515–533.
- _____, 2001: The general circulation of the atmosphere: 2000 program of study in geophysical fluid dynamics. *Woods Hole Oceanographic Institution Tech. Rep.* WHOI-2001-03, 181 pp., <https://darchive.mblwhoilibrary.org/handle/1912/15>.
- _____, and M. J. Suarez, 1994: A proposal for the intercomparison of the dynamical cores of atmospheric general circulation models. *Bull. Amer. Meteor. Soc.*, **75**, 1825–1830.
- Hu, Y. and Q. Fu, 2007: Observed poleward expansion of the Hadley circulation since 1979. *Atmos. Chem. Phys.*, **7**(19), 5229–5236.
- Hu, Y., L. Tao, and J. Liu 2013: Poleward expansion of the Hadley circulation in CMIP5 simulations. *Adv. Atmos. Sci.*, **30**(3), 790–795.

- Hurrell, J. W., Holland, M. M., Gent, P. R., Ghan, S., Kay, J. E., Kushner, P. J., Lamarque, J. F., Large, W. G., Lawrence, D., Lindsay, K. and Lipscomb, W. H., 2013: The community earth system model: a framework for collaborative research. *Bull. Amer. Meteor. Soc.*, **94**(9), 1339–1360.
- Kageyama, M., Braconnot, P., Harrison, S.P., Haywood, A.M., Jungclaus, J.H., Otto-Bliesner, B.L., Peterschmitt, J.Y., Abe-Ouchi, A., Albani, S., Bartlein, P.J. and Brierley, C., 2018. The PMIP4 contribution to CMIP6–Part 1: Overview and over-arching analysis plan. *Geosci. Model Dev.*, **11**(3), 1033–1057.
- Kang, S. M., and L. M. Polvani 2011: The interannual relationship between the latitude of the eddy-driven jet and the edge of the Hadley cell. *J. Climate*, **24**(2), 563–568.
- Kidston, J., and Gerber, E. P. 2010: Intermodel variability of the poleward shift of the austral jet stream in the CMIP3 integrations linked to biases in 20th century climatology. *Geophys. Res. Lett.*, **37**(9).
- _____, G. K. Vallis, S. M. Dean, and J. A. Renwick, 2011: Can the increase in the eddy length scale under global warming cause the poleward shift of the jet streams?. *J. Climate*, **24**(14), 3764–3780.
- _____, and _____, 2012: The relationship between the speed and the latitude of an eddy-driven jet in a stirred barotropic model. *J. Atmos. Sci.*, **69**(11), 3251–3263.
- Kim, H.-K., and S. Lee, 2001a: Hadley cell dynamics in a primitive equation model. Part I: Axisymmetric flow. *J. Atmos. Sci.*, **58**, 2845–2858.
- _____, 2001b: Hadley cell dynamics in a primitive equation model. Part II: Nonaxisymmetric flow. *J. Atmos. Sci.*, **58**(19), 2859–2871.
- Kim, S.J., Flato, G., and Boer, G., 2003: A coupled climate model simulation of the Last Glacial Maximum, Part 2: approach to equilibrium, *Clim. Dynam.*, **20**, 635–661, 2003.
- Kim, S. J., Jun, S. Y. and Kim, B. M., 2017: Sensitivity of southern hemisphere westerly wind to boundary conditions for the last glacial maximum. *Quaternary International*, **459**, 165–174.
- Kim, S. Y., and S. W. Son, 2020: Breakdown of the linear relationship between the Southern Hemisphere Hadley Cell Edge and Jet Latitude Changes in the Last Glacial Maximum. *J. Climate*, **33**(13), 5713–5725.

-
- _____, 2023: Opposing Shifts of the Hadley Cell Edge and Eddy-Driven Jet Latitude in the Last Glacial Maximum: A Parameter Sweep Study Using a Dynamical Core GCM. *J. Climate*, **36**(3), 885-898.
- Kobayashi, S., and Coauthors, 2015: The JRA-55 reanalysis: General specifications and basic characteristics. *J. Meteor. Soc. Japan*, **93**(1), 5–48, doi:10.2151/jmsj.2015-001.
- Lau, W. K., and Kim, K. M., 2015: Robust Hadley circulation changes and increasing global dryness due to CO₂ warming from CMIP5 model projections. *Proc. Natl. Acad. Sci.*, **112**(12), 3630-3635.
- Lee, S. H., P.D. Williams, and T. H. Frame, 2019: Increased shear in the North Atlantic upper-level jet stream over the past four decades. *Nature*, **572**(7771), 639–642.
- Lee, S., 1999: Why are the climatological zonal winds easterly in the equatorial upper troposphere?. *J. Atmos. Sci.*, **56**(10), 1353-1363.
- Lee, S. Y., Chiang, J. C., Matsumoto, K., and Tokos, K. S. 2011: Southern Ocean wind response to North Atlantic cooling and the rise in atmospheric CO₂: Modeling perspective and paleoceanographic implications. *Paleoceanography*, **26**, PA1214.
- Levine, X. J., and T. Schneider, 2015: Baroclinic eddies and the extent of the Hadley circulation: An idealized GCM study. *J. Atmos. Sci.*, **72**(7), 2744–2761.
- Li, C., Stevens, B., and J. Marotzke, J. 2015: Eurasian winter cooling in the warming hiatus of 1998–2012. *Geophys. Res. Lett.*, **42**(19), 8131-8139.
- Lorenz, D. J., and D. L. Hartmann, 2001: Eddy–zonal flow feedback in the Southern Hemisphere. *J. Atmos. Sci.*, **58**, 3312–3327, doi:10.1175/1520-0469(2001)058<3312:EZF2.0.CO;2.
- _____, 2014: Understanding midlatitude jet variability and change using Rossby chromatography: Poleward-Shifted Jets in Response to External Forcing. *J. Atmos. Sci.*, **71**, 2370–2389.
- Lu, J., G. Vecchi, and T. Reichler, 2007: Expansion of the Hadley cell under global warming. *Geophys. Res. Lett.*, **34**, L06805, doi:10.1029/2006GL028443.

- _____, G. Chen, and D. M. W. Frierson, 2008: Response of the zonal mean atmospheric circulation to El Niño versus global warming. *J. Climate*, **21**, 5835–5851, doi:10.1175/2008JCLI2200.1.
- _____, G. Chen, G., and D. M. Frierson, 2010: The position of the midlatitude storm track and eddy-driven westerlies in aquaplanet AGCMs. *J. Atmos. Sci.*, **67**(12), 3984–4000.
- Lucas, C., B. Timbal, and H. Nguyen, 2014: The expanding tropics: A critical assessment of the observational and modeling studies. *Wiley Interdiscip. Rev.: Climatic Change*, **5**, 89–112, doi:10.1002/wcc.251.
- Lutsko, N. J., I. M. Held, P. Zurita-Gotor, and A. K. O'Rourke, 2017: Lower-tropospheric eddy momentum fluxes in idealized models and reanalysis data. *J. Atmos. Sci.*, **74**(11), 3787–3797.
- Mantsis, D. F., S. Sherwood, R. Allen, and L. Shi, 2017: Natural variations of tropical width and recent trends. *Geophys. Res. Lett.*, **44**(8), 3825–3832.
- Marshall, J., and K. Speer, 2012: Closure of the meridional overturning circulation through Southern Ocean upwelling, *Nat. Geosci.*, **5**, 171–180.
- Neale, R. B., and Coauthors, 2012: Description of the NCAR Community Atmosphere Model (CAM 5.0). NCAR Tech. Note NCAR/TN-4861STR, 268, <https://doi.org/10.5065/D6N877R0>.
- O'Rourke, A. K., and G. K. Vallis, 2016: Meridional Rossby wave generation and propagation in the maintenance of the wintertime tropospheric double jet. *J. Atmos. Sci.*, **73**(5), 2179–2201.
- Oleson, K., Lawrence, D. M., Bonan, G. B., Drewniak, B., Huang, M., Koven, C. D., and Coauthors, 2013: Technical description of version 4.5 of the Community Land Model (CLM) (No. NCAR/TN-503+STR). doi:10.5065/D6RR1W7M
- Randel, W. J., and I. M. Held, 1991: Phase speed spectra of transient eddy fluxes and critical layer absorption. *J. Atmos. Sci.*, **48**(5), 688–697.
- Riviere, G. 2009: Effect of Latitudinal Variatons in Low-Level Baroclinicity on Eddy Life Cycles and Upper-Tropospheric Wave-Breaking Processes. *J. Atmos. Sci.*, **66**, 1569–1592.

- Riviere, G., 2011: A dynamical interpretation of the poleward shift of the jet streams in global warming scenarios. *J. Atmos. Sci.*, **68**, 1253–1272.
- Rojas, M. 2013: Sensitivity of Southern Hemisphere circulation to LGM and 4 × CO₂ climates. *Geophys. Res. Lett.*, **40**(5), 965–970.
- Ronalds, B., and E. A. Barnes, 2019: A role for barotropic Eddy–Mean Flow Feedbacks in the Zonal Wind Response to Sea Ice Loss and Arctic Amplification. *J. Climate*, **32**(21), 7469–7481.
- Rotstayn, L. D., M. A. Collier, S. J., Jeffrey, J., Kidston, J. I., Syktus, and K. K. Wong, 2013: Anthropogenic effects on the subtropical jet in the Southern Hemisphere: aerosols versus long-lived greenhouse gases. *Env. Res. Lett.*, **8**(1), 014030.
- Russell, J. L., K. W. Dixon, A. Gnanadesikan, R. J. Stouffer, and J. R. Toggweiler, 2006: The Southern Hemisphere westerlies in a warming world: Propping open the door to the deep ocean. *J. Climate*, **19**(24), 6382–6390.
- Screen, J. A., T. J. Bracegirdle, and I. Simmonds, 2018: Polar climate change as manifest in atmospheric circulation. *Curr. Climate Change Rep.* <https://doi.org/10.1007/S40641-018-0111-4>
- Seidel, D. J., Q. Fu, W. J. Randel, and T. J. Reichler, 2008: Widening of the tropical belt in a changing climate. *Nature Geoscience*, **1**(1), 21–24.
- Sigman, D. M., Hain, M. P., and Haug, G. H., 2010: The polar ocean and glacial cycles in atmospheric CO₂ concentration, *Nature*, **466**, 47–55, doi:10.1038/nature09149.
- Sime, L.S., Hodgson, D., Bracegirdle, T.J., Allen, C., Perren, B., Roberts, S. and de Boer, A.M., 2016. Sea ice led to poleward-shifted winds at the Last Glacial Maximum: the influence of state dependency on CMIP5 and PMIP3 models. *Climate of the Past*, **12**(12), 2241–2253.
- Simpson, I.R., and L. M. Polvani, 2016: Revisiting the relationship between jet position, forced response and annular mode variability in the southern midlatitudes. *Geophys. Res. Lett.*, **43**(6), 2896–2903, doi:10.1002/2016GL06789.

- Sobel, A. H., and T. Schneider, 2009: Single-layer axisymmetric model for a Hadley circulation with parameterized eddy momentum forcing. *J. Adv. Model Earth Syst.*, **1**, doi:10.3894/JAMES.2009.1.10.
- Son, S.-W., and S. Lee, 2005: The response of westerly jets to thermal driving in a primitive equation model. *J. Atmos. Sci.*, **62**(10), 3741–3757.
- _____, N. F. Tandon, L. M. Polvani, and D. W. Waugh, 2009: Ozone hole and Southern Hemisphere climate change. *Geophys. Res. Lett.*, **36**(15).
- _____, and Coauthors: 2010: Impact of stratospheric ozone on Southern Hemisphere circulation change: A multimodel assessment. *J. Geophys. Res. Atmos.*, **115**(D3).
- _____, B. R. Han, C. I. Garfinkel, S. Y. Kim, R. Park, N. Abraham, G. Zeng, and coauthors, 2018a: Tropospheric jet response to Antarctic ozone depletion: an update with Chemistry-Climate Model Initiative (CCMI) models. *Environ. Res. Lett.*, **13**, 054024.
- _____, S.-Y. Kim, and S. Min, 2018b: Widening of the Hadley cell from Last Glacial Maximum (LGM) to future climate. *J. Climate*, **31**, 267–281.
- Staten, P., W., J. Lu, K. M. Grise, S. M. Davis, T. Birner, 2018: Re-examining tropical expansion. *Nat Clim Chang.* **8**, 768–775.
- Strong, C., and Magnúsdóttir, G., 2008: Tropospheric Rossby wave breaking and the NAO/NAM. *J. Atmos. Sci.*, **65**(9), 2861–2876.
- Sun, L., G. Chen, and J. Lu, 2013: Sensitivities and mechanisms of the zonal mean atmospheric circulation response to tropical warming. *J. Atmos. Sci.*, **70**(8), 2487–2504.
- Taylor, K. E., R. J. Stouffer, and G. A. Meehl, 2012: An overview of CMIP5 and the experiment design. *Bull. Amer. Meteor. Soc.*, **93**(4), 485–498
- Thompson, D. W., and J. M. Wallace, 2000: Annular modes in the extratropical circulation. Part I: Month-to-month variability. *J. Climate*, **13**(5), 1000–1016.

- Thorncroft, C. D., B. J. Hoskins, and M. E. McIntyre, 1993: Two paradigms of baroclinic-wave life-cycle behaviour. *Q. J. R. Meteorol. Soc.*, **119**(509), 17-55
- Toggweiler, J. R., Russell, J., and Carson, S. R., 2006: Midlatitude westerlies, atmospheric CO₂, and climate change during the ice ages, *Paleoceanography*, **21**, PA2005, doi:10.1029/2005PA001154, 2006.
- _____, and J. Russell, 2008: Ocean circulation in a warming climate. *Nature*, **451**(7176), 286–288.
- Vallis, G. K., 2006: Atmospheric and Oceanic Fluid Dynamics. 1st ed. Cambridge University Press, 745 pp.
- _____, P. Zurita-Gotor, C. Cairns, and J. Kidston 2015: Response of the large-scale structure of the atmosphere to global warming. *Quart. J. Roy. Meteor. Soc.*, **141**(690), 1479–1501.
- Walker, C. C., and T. Schneider, 2006: Eddy influences on Hadley circulations: Simulations with an idealized GCM. *J. Atmos. Sci.*, **63**, 3333–3350, <https://doi.org/10.1175/JAS3821.1>.
- Wang N., D. Jiang, and X. Lang, 2018: Metric-Dependent Tendency of Tropical Belt Width Changes during the Last Glacial Maximum. *J. Climate*, **31**(20), 8527–8540.
- Waugh, D. W., K. M. Grise, W. J. M. Seviour, S. M. Davis, N. Davis, O. Adam, and coauthors, 2018: Revisiting the relationship among metrics of tropical expansion. *J. Climate*, **31**(18), 7565–7581.
- Wilcox, L. J., Charlton-Perez, A. J., and L. J. Gray, 2012: Trends in Austral jet position in ensembles of high-and low-top CMIP5 models. *J. Geophys. Res. Atmos.*, **117**(D13).
- Yuval, J., and Y. Kaspi, 2016: Eddy activity sensitivity to changes in the vertical structure of baroclinicity. *J. Atmos. Sci.*, **73**(4), 1709–1726.

국문 초록

해들리 순환의 경계와 에디에 의한 제트(이하, “제트”)의 위도의 극방향 이동은 지난 몇 십년간 남반구에서 관찰되어 왔다. 이러한 변화는 미래에도 계속해서 나타나는 것으로 미래기후 시나리오에서 보고된 바 있으며, 이는 열대 및 아열대 동서평균 순환이 현재부터 미래 기후까지 같은 방향으로 이동함을 뜻한다. 여기서 우리는 이러한 일관된 동서평균 순환의 변화가 과거 한랭 기후에는 다르게 나타남을 보였다. 이를 위해 먼저 21,000 년 전 고기후를 모의하는 마지막최대빙하기(Last Glacial Maximum; LGM), 산업화이전시기(Pre-industrial; PI), 그리고 미래기후를 모사하는 연장된 RCP4.5 (Extended Concentration Pathway 4.5; ECP4.5)의 세 가지 시나리오를 갖는 PMIP3 (Paleoclimate Modeling Intercomparison Project Phase 3)와 CMIP5 (Coupled Model Intercomparison Project Phase 5)에 해당하는 전지구 기후모형 자료들을 이용하여 고기후부터 미래기후까지 남반구 대규모 대기대순환의 변화를 확인하였다. 그 결과, 남반구 해들리 순환 경계는 LGM 부터 PI 까지, 그리고 PI 부터 ECP4.5 까지 체계적으로 극방향으로 이동하였다. 반면, 제트의 경우 이러한

전지구 온도 변화에 따른 체계적 이동을 보이지 않았다. 모든 모형들이 PI 실험에서 ECP4.5 실험으로 극방향 제트 이동을 보인 반면, 반 이상의 모형들이 LGM 부터 PI 실험까지 적도방향 제트 이동을 보였다. 즉, 이는 LGM 실험에서 해들리 순환 경계는 현재보다 적도 방향으로 이동하는 반면, 제트의 위치는 보다 극방향으로 이동했을 수 있다는 점을 보여준다. 이러한 반대방향 움직임은 연평균 결과에서도 잘 나타났으며, 특히 LGM 실험에서 남극 지표 냉각이 열대 상층 냉각보다 큰 남반구 겨울철에 보다 두드러지게 나타났다. 이는 남극의 강한 냉각이 해들리순환-제트의 이동 방향을 다르게 하는 데에 기여한다는 것을 의미한다.

해들리 순환과 제트의 반대 방향 이동, 즉 해들리 순환 경계의 적도 방향 이동과 제트 위치의 극방향 이동은 기후모형의 LGM 실험뿐 아니라 LGM 유사 열강제력이 부과된 이상화된 건조역학모형 실험에서도 잘 나타났다. 열대 대류권 상부와 극지표의 냉각 강제력의 세기를 체계적으로 그리고 독립적으로 변화시켜가며 32 개의 평형 실험을 진행한 결과, 반대방향 이동은 극냉각이 열대냉각보다 충분히 클 때 발생한다는 것을 확인하였다. 이는 주로 제트위치가, 해들리 순환에 비해, 극냉각에 대해 민감하게 반응하기 때문이다. 해들리 순환 경계의 변화는 크게

느린 파동과 축대칭(axisymmetric) 순환 변화에 의해 설명되었다. 이들은 해들리 순환이 중위도 경압성의 변화에 대해 보다 약하게 반응하도록 유도했으며, 이는 해들리 순환 경계의 적도방향 이동을 초래하였다. 이와는 달리, 제트위치는 극냉강에 의한 중위도 하층 경압성의 극방향 이동 및 강화에 크게 연관된다. 고위도에서 하층 경압성의 강화는 파수가 짧은 긴 파동이 보다 불안정해지도록 만들었으며, 반시계방향 파동궤적을 보다 많이 일으켜 제트의 극방향 이동을 유도한다.

이러한 역학적 해석은 대기-해양 결합 모형(Atmospheric-coupled global climate models; AGCM)을 통해 재확인되었다. 여기서 극지표 냉각의 강화 효과를 확인하기 위해, LGM 조건 실험에서 남극 해빙농도(sea ice concentration; SIC)를 증가시켜가며 실험하였다. LGM 겨울 조건에서 분석한 결과, 남극 해빙농도가 높은 모형은 해들리 순환-제트의 반대방향 이동을 잘 모의하였다. 이는 남반구 제트의 위치 변화에 남극 해빙이 주요한 역할을 한다는 것을 의미한다. 또한 증가된 남극 해빙은 고위도의 하층 경압성을 증가시켰으며, 이는 긴 파동의 활동성을 증대시켰다. 이는 앞서 단순역학 모형에서 제시된 역학적

메커니즘이 보다 복잡한 기후모형에서도 적용될 수 있음을 시사한다.

우리는 또한 지구온난화-모사 역학코어 실험을 추가로 진행하였으며, 해들리 순환 경계 및 제트위치의 반대 방향 이동, 단, 극방향 해들리 순환 경계 이동과 적도방향 제트위치의 이동을 발견하였다. 이는 추후 미래 기후에서도 해들리 순환-제트의 반대방향 이동이 나타날 수 있음을 시사한다.